

**ENHANCED REACTIVITY OF ULTRATHIN OXIDE
FILMS IN OXIDATION REACTIONS:
BACK TO “ELECTRONIC THEORY OF CATALYSIS”**



Dissertation

zur Erlangung des akademischen Grades des

Doktors der Naturwissenschaften

(Dr. rer. nat.)
im Fach Chemie

eingereicht im Fachbereich Biologie, Chemie, Pharmazie
der Freien Universität Berlin

vorgelegt von

Ying-Na Sun

geboren am 5. November 1981
in Ningbo-China

Berlin 2010

Diese Arbeit wurde von November 2006 bis August 2010 am Fritz-Haber-Institut der Max-Planck-Gesellschaft in der Abteilung Chemische Physik unter Anleitung von Herrn Prof. Dr. H.-J. Freund angefertigt.

Gutachter:

1. Prof. Dr. H.-J. Freund
2. Prof. Dr. K. Christmann

Disputation am: November 8, 2010

ACKNOWLEDGEMENTS

I gratefully acknowledge my supervisor, **Prof. Dr. Hans-Joachim Freund**, for the opportunity to work in his fascinating research group, for his constant encouragement and guidance. I have enjoyed being part of this dynamic, international team of scientists, who collaborate on a wide range of research projects and openly engage in scientific discussions.

I would like to thank **Prof. Dr. Klaus Christmann** for kindly being the co-supervisor and reviewing my thesis.

I am particularly grateful to **Dr. Shamil Shaikhutdinov**, who is my daily scientific advisor. Without his consistent and illuminating instruction, this thesis could not have reached its present form. I greatly appreciate his patience, support and the trust he showed in me throughout my thesis.

I am also greatly indebted to **Dr. Sarp Kaya**, who has instructed and helped me a lot in the beginning of my PhD studies.

I am also whole hearty thankful to my colleagues, **Dr. Zhi-hui Qin, Mikolaj Lewandowski, Dr. Yu Lei, Yuichi Fujimori and Yulia Martynova**, for their invaluable help and fruitful discussions. I deeply appreciate their contribution to this work.

My thanks would also go to **Uwe Härtel, Burkhard Kell, Walter Wachsmann, Klaus-Peter Vogelgesang and Matthias Naschitzki**, for their technical assistance, and to **Manuela Misch** and **Gabriele Mehnert** for their tireless help in administrative works.

I also owe my sincere gratitude to my chinese friends in chemical physics department, **Dr. Bing Yang, Xin Yu, Hui-feng Wang, Dr. Xiang Shao, Dr. Xiao Lin and Yi Pan**. Being with them made me feel much closer to my hometown, and their help made my life in Berlin easier and more joyful.

I would also like to thank all other colleagues at the department, past and present, for providing help with all kinds of things I would not have managed on my own.

Finally my deepest gratitude goes to my beloved parents for their endless love, warm support, encouragement and great confidence in me, and to my husband for his love, enlightening advice and making each day the happiest day of my life. They gave me the inspiration and energy that made this dissertation possible. It is dedicated to them, with all my heart!

ABSTRACT

Thin oxide films grown on metal single crystals are used in many “surface science” research groups aimed to understand surface chemistry of metal oxides. Although these films may show structural and electronic properties different from their bulk counterparts, such films are employed as suitable supports for modeling highly dispersed metal catalysts. However, in the case of ultra-thin films, i.e. few monolayers in thickness, a metal substrate underneath the film may strongly affect the properties of metal deposits via charge transfer through the oxide film.

In this work, we show that the thickness matters not only for metal deposits but also for the gas phase molecules reacting at the surface. More specifically, we show that monolayer FeO(111) films grown on Pt(111) single crystals, which are essentially inert under vacuum conditions, exhibit greatly enhanced reactivity in low temperature CO oxidation as compared to Pt(111) when performed at realistic conditions in the mbar pressure range. The reactivity studies, complemented with structural characterization using various surface science techniques, show that the reaction involves transformation of bi-layer Fe-O film into the tri-layer O-Fe-O (FeO₂) film that catalyses CO oxidation via Mars – van Krevelen type mechanism.

The results may have strong impact on reactivity of oxide supported metal catalysts, undergoing encapsulation by thin oxide layers steaming from the support as a result of a so-called strong metal-support interaction (SMSI). Indeed, we observe rate enhancement in CO oxidation reaction on Fe₃O₄(111)-supported Pt particles encapsulated by thin FeO(111) film as compared to clean Pt particles.

The results suggest that metal supported ultrathin oxide films may serve as promising catalytic systems with tunable reactivity, which can be achieved by a proper combination of a metal substrate and an oxide film. These results revive an “electronic theory of catalysis” developed in the last century, in particular predicting that by varying the thickness of oxide films one could control reactivity of heterogeneous catalysts.

ZUSAMMENFASSUNG

Dünne, auf Metalleinkristallen aufgewachsene Oxidfilme werden von vielen "Surface Science"-Forschungsgruppen genutzt, um die Oberflächenchemie von Metalloxiden zu verstehen. Obwohl diese Filme andere strukturelle und elektronische Eigenschaften als die entsprechenden Volumenkristalle aufweisen können, werden solche Filme als geeignete Träger für hochdisperse metallische Modellkatalysatoren verwendet. Bei ultra-dünnen Filmen mit einer Dicke von wenigen Monolagen kann das Metallsubstrat durch Ladungstransfer durch den Oxid-Film jedoch einen starken Einfluss auf die Eigenschaften der dispergierten Metallpartikel haben.

In dieser Arbeit zeigen wir, dass die Dicke nicht nur für die Metallpartikel, sondern auch für Moleküle aus der Gasphase, die auf der Oberfläche reagieren, von Bedeutung ist. Insbesondere zeigen wir, dass auf Pt(111)-Einkristallen aufgewachsene FeO(111)-Monolagenfilme, die unter Vakuumbedingungen quasi inert sind, eine deutlich erhöhte Reaktivität für CO Oxidation bei niedrigen Temperaturen im Vergleich zu Pt(111) zeigen, wenn die Reaktion unter realistischen Bedingungen im mbar-Druckbereich durchgeführt wird. Die Reaktivitätsstudien in Kombination mit Strukturcharakterisierung durch unterschiedliche Surface Science Methoden zeigen, dass die Reaktion eine Umwandlung von einem doppellagigen Fe-O Film zu einem dreilagigen O-Fe-O (FeO_2) Film, welcher die CO Oxidation katalysiert, gemäß eines Mars-van Krevelen-Mechanismus beinhaltet.

Die Ergebnisse können einen starken Einfluss auf die Reaktivität von Oxid-geträgerten Metallkatalysatoren haben, die durch starke Metall-Träger-Wechselwirkungen (strong metal support interactions, SMSI) von dünnen, aus dem Träger stammenden Oxidschichten eingeschlossen werden. In der Tat, beobachten wir erhöhte Reaktionsraten für CO-Oxidation auf $\text{Fe}_3\text{O}_4(111)$ -geträgerten Pt Partikeln, die von einem dünnen FeO(111) Film umschlossen sind, im Gegensatz zu sauberen Pt Partikeln.

Diese Ergebnisse legen nahe, dass Metall-geträgerte ultra-dünne Oxidfilme durch geeignete Kombination von Metallsubstrat und Oxidfilm als vielversprechende katalytische Systeme mit durchstimmbarer Reaktivität genutzt werden können. Die Ergebnisse beleben des Weiteren die im letzten Jahrhundert entwickelte "Elektronische-Theorie der Katalyse"

erneut. Insbesondere wurde vorhergesagt, dass man durch eine Variierung der Oxidfilmstärke die Reaktivität in heterogener Katalyse kontrollieren kann.

CONTENTS

ACKNOWLEDGEMENTS	i
ABSTRACT	iii
ZUSAMMENFASSUNG.....	v
LIST OF FIGURES.....	xi
LIST OF TABLES	xxi
Chapter 1 Introduction	1
Chapter 2 Methods and Materials	11
2.1. Experimental Setup.....	11
2.2. Surface Analytical Techniques.....	14
2.2.1. Low Energy Electron Diffraction (LEED).....	14
2.2.2. Auger Electron Spectroscopy (AES)	18
2.2.3. Scanning Tunneling Microscopy (STM).....	20
2.2.4. Temperature Programmed Desorption (TPD).....	23
2.3. Gas Chromatography (GC)	33
2.4. The Iron Oxide Films on Pt(111)	37
Chapter 3 CO Oxidation on Ultrathin FeO(111)/Pt(111).....	45
3.1. CO Oxidation under UHV Conditions	45
3.2. CO Oxidation at Elevated Pressures	50
3.2.1. Stoichiometric CO:O ₂ Ratio (2:1).....	50
3.2.2. The Effect of CO and O ₂ Partial Pressures	60
3.2.3. Proposed Mechanism.....	67
Chapter 4 Oxidation of the FeO Films.....	71
4.1. The Structure of Oxygen Rich Iron Oxide Films	71
4.2. The Effect of Oxidants (NO vs. O ₂)	79
Chapter 5 Pt Particles on Fe ₃ O ₄ (111).....	87
5.1. Preparation and Structure	87
5.2. CO Adsorption on Fe ₃ O ₄ (111) Supported Pt Particles	88
5.3. CO Dissociation on Pt/Fe ₃ O ₄ (111).....	92
5.4. SMSI Effect	100
5.5. CO Oxidation on Pt/Fe ₃ O ₄ (111).....	104

Chapter 6 Reactivity of FeO/Pt(111) in PROX.....	107
6.1. Reactivity and Selectivity	108
6.2. Structural Characterization	115
Chapter 7 Summary and Outlook	123
Abbreviations	127
Curriculum Vitae	129
Publications	131
Bibliography	133

LIST OF FIGURES

Fig. 1.1 Schematic illustration of a supported model catalyst.....	2
Fig. 1.2 Energy band diagram of a metal-n-type semiconductor contact with an interfacial layer [75]. ϕ_M : work function of metal, ϕ_B : barrier height of metal-semiconductor surface barrier, ϕ_0 : energy level measured from the edge of the valence band to the energy below which surface states must be filled for charge neutrality at the semiconductor, χ_s : electron affinity of semiconductor, δ : thickness of the interfacial layer, V : potential across interfacial layer.....	4
Fig. 1.3 Electronic levels in the metal, oxide and adsorbed oxygen [74]. (a) before electrons have passed through the oxide. (b) when equilibrium is reached.....	5
Fig. 1.4 (a)-(b) Schematic representation of the interface charge transfer and oxide film rumpling. (black circles cations, white circles anions, grey circles metal substrate). (c)-(d) Schematic representation of “direct” (c) and “flipped” (d) adsorption modes of an adatom (large circle) on a supported oxide film. (from [96]).....	7
Fig. 2.1 Schematic illustration of the experimental setup.....	12
Fig. 2.2 Schematic representation of the sample holder and the reactor.....	12
Fig. 2.3 Setup of the GC system.....	13
Fig. 2.4 Experimental setup of a LEED optics.....	14
Fig. 2.5 Schematic representation of the diffraction process.....	15
Fig. 2.6 LEED pattern ($E= 60$ eV) and schematic structure for the clean Pt(111) sample.....	15
Fig. 2.7 The Ewald construction for the surface case.....	16
Fig. 2.8 The wood(left) and matrix (right) terminology for surface lattices. a_1 and a_2 correspond to the substrate unit cell vectors. b_1 and b_2 indicate the superstructure unit cell vectors. α is the enclosed angle between the substrate, and γ is the enclosed angle between the superstructure unit cell vectors. The angle β and δ accounts for a rotation of the superstructure with respect to the substrate.....	17
Fig. 2.9 Auger electron emission mechanism.....	18
Fig. 2.10 AES spectrum of clean Pt(111) surface as an example. Primary energy: 3 keV. NOO transition is shown.....	19
Fig. 2.11 Universal curve for electron mean free path (adapted from [111]).	19

Fig. 2.12 The principle of tunneling between the surface and the metal tip for positive tip bias V . Tunneling of electrons from occupied surface states into the metal tip (adapted from [113]).....	21
Fig. 2.13 Schematic illustration of the tunneling geometry in the theory of Tersoff-Hamann model. The tunneling tip has been approximated by a spherical potential well with the radius R . The distance of nearest approach is d . The centre of curvature of tip is r_0 . (adapted from [115])	22
Fig. 2.14 Schematic representation of a scanning tunneling microscope.....	23
Fig. 2.15 Sketch of the quadrupole mass spectrometer.....	24
Fig. 2.16 Schematic potential diagram for the (a) molecular chemisorption, (b) non-activated, dissociative chemisorption, (c) activated, dissociative chemisorption of a diatomic molecule. Solid line curve: the total potential energy curve.....	26
Fig. 2.17 Schematic TPD spectrum (adapted from [107]).	27
Fig. 2.18 A series of TPD curves for a zero order (a), first order (b), and second order (c) desorption process.....	29
Fig. 2.19 The so-called “complete analysis” of TPD data. (a) The spectra are integrated to determine points on the spectra corresponding to a fixed coverage. (b) A pair of (r , T) values for every desorption trace are given, from which an Arrhenius plot is made. (c) The slope yields the activation energy [113].....	30
Fig. 2.20 Illustration of retention factor K	34
Fig. 2.21 A normal distribution. The quantity w_h is the width at 0.5 of the peak height and corresponds to 2.354σ . The quantity w_b is the base width and corresponds to 4σ as indicated.....	34
Fig. 2.22 $P(O_2)$ - T phase diagram of Fe- O_2 system [132].....	38
Fig. 2.23 Schematic representation of the side view (left) and top view (right) of FeO(111) and Fe ₃ O ₄ (111) crystals.....	39
Fig. 2.24 (a) LEED pattern of FeO(111)/Pt(111) at 60 eV; (b) cross and top views of an FeO(111) film on Pt(111); (c-d) STM images of FeO(111)/Pt(111) in different sizes, $V=0.8$ V, $I=0.5$ nA (provided by M. Lewandowski); the unit cells of FeO and Moiré superstructure are indicated.....	40
Fig. 2.25 (a) LEED pattern of an Fe ₃ O ₄ (111) film grown on Pt(111), a $p(2 \times 2)$ unit cell is indicated; (b) STM images of Fe ₃ O ₄ (111)/Pt(111) (provided by M. Lewandowski).....	41
Fig. 2.26 Typical TPD spectrum of CO adsorbed at 90 K on an Fe ₃ O ₄ (111) film. Three desorption states are denoted as α , β , and γ . The heating rate is 3 Ks^{-1}	42

Fig. 3.1 TPD spectra of CO adsorbed at 150 K on Pt(111) surface as a function of CO exposure. The heating rate is 3 Ks^{-1} .	46
Fig. 3.2 LEED pattern of Pt(111) by exposure to CO with saturation coverage in UHV at RT (left) and 20 mbar of O_2 at RT (right). The unit cell of Pt(111) substrates and overlayers are shown in black and blue, respectively.	47
Fig. 3.3 TPD spectra of O_2 adsorbed at 100 K on Pt(111) surface as a function of O_2 exposure. The heating rate is 3 Ks^{-1} .	47
Fig. 3.4 Thermal desorption spectra of Pt(111) surface by exposure to 20 mbar O_2 at RT for 10 min. 32 amu (O_2) signal is shown. The heating rate is 3 Ks^{-1} .	48
Fig. 3.5 Temperature desorption spectra of CO and O_2 coadsorbed on Pt(111). The 28 (CO), 32 (O_2) and 44 (CO_2) amu signals are shown. (a) CO adsorption on O_2 precovered Pt (111); (b) O_2 adsorption on CO precovered Pt(111); (c) CO and O_2 simultaneous adsorption. The heating rate is 3 Ks^{-1} .	49
Fig. 3.6 Kinetics of CO_2 production over FeO/Pt(111) at stoichiometric CO: O_2 (2:1) ratios at indicated total pressures at 450 K. The results for Pt(111) and nm-thick $\text{Fe}_3\text{O}_4(111)/\text{Pt}(111)$ film in 40 mbar CO + 20 mbar O_2 at 450 K are shown for comparison. Time zero corresponds to the start of the sample heating (1 Ks^{-1}) from 300 K.	51
Fig. 3.7 Temperature-programmed reaction profile of CO_2 production over FeO(111)/Pt(111) on slow heating (1 Kmin^{-1}) in 40 mbar CO + 20 mbar O_2 balanced by He.	52
Fig. 3.8 kinetics of CO_2 production over FeO(111)/Pt(111) in 40 mbar CO + 20 mbar O_2 balanced by He at indicated temperatures.	52
Fig. 3.9 LEED patterns ($E = 60 \text{ eV}$) of the FeO(111) film after reaction at 400 K (left) and 450 K (right) in 40 mbar CO + 20 mbar O_2 in He.	53
Fig. 3.10 AES spectra of the clean FeO(111) film (top), after the reaction in 40 mbar CO + 20 mbar O_2 at 450 K (middle) and subsequent annealing to 800 K for 2 min (bottom). The corresponding peak ratios for O(510 eV) and Fe(658 eV) are indicated.	54
Fig. 3.11 Room temperature STM images (provided by Z.-H. Qin) (size $200 \text{ nm} \times 200 \text{ nm}$) of Pt(111) (a), FeO(111) film after 10 min (b), and FeO(111) film after 120 min (c) in 40 mbar + 20 mbar O_2 in He at 450 K.	55
Fig. 3.12 LEED patterns ($E = 60 \text{ eV}$) of the FeO(111) film after reaction at 450 K(left) in 40 mbar CO + 20 mbar O_2 in He and subsequently annealed in vacuum at 800 K (right).	56
Fig. 3.13 STM images (provided by Z.-H. Qin) (size $500 \text{ nm} \times 500 \text{ nm}$) of the dewetted FeO(111) film and step-wise UHV annealing at 500, 700 and 800 K.	56

Fig. 3.14 TPD spectra of CO adsorbed at 300 K on the clean Pt(111) (dotted line) and FeO(111)/Pt(111) after reaction (red line) and after step-wise UHV annealing at 600 K (green line) and 800 K (blue line).	57
Fig. 3.15 (a) Time-resolved PM-IRAS spectra of the CO stretching region obtained from the FeO(111)/Pt(111) surface at 450 K in a mixture of 40 mbar CO + 20 mbar O ₂ in He to 1 bar. The spectrum for the Pt(111) surface after 120 min at the same conditions is shown for comparison. (b) Kinetics of CO ₂ formation in the gas phase and of CO adsorbed on FeO(111)/Pt(111) obtained by integration of the respective PM-IRAS signals. (provided by E. Carrasco)	58
Fig. 3.16 CO (28 amu) and CO ₂ (44 amu) signals in TPD spectra of a FeO(111)/Pt(111) film reacted in 40 mbar CO + 20 mbar O ₂ for 120 min at indicated temperatures. The samples were cooled to 300 K and evacuated to 10 ⁻⁵ mbar before exposing to UHV. The inset shows the Arrhenius plot for the integral CO desorption signal as a function of reaction temperature. The spectrum for clean Pt(111) after reaction at 450 K is shown as dotted line for comparison. TPD spectrum of Pt _x (CO) _y formed on Pt(111) by Pt deposition in 10 ⁻⁶ mbar of CO at 100 K (dashed line) is shown to highlight a desorption feature at ~380 K.....	59
Fig. 3.17 Kinetics of CO ₂ production at 450 K at different CO and O ₂ partial pressures as indicated. Full conversion can be reached at low CO:O ₂ ratios. Note the reaction rate slows down in CO-rich conditions. (CO:O ₂ >1).	62
Fig. 3.18 Reaction rate (a), average stoichiometry (b) and degree of dewetting (c) of the spent FeO/Pt catalysts as a function of O ₂ pressure in the mixture with 10 mbar of CO, balance by He to 1 bar. The reaction temperature is 450 K.	63
Fig. 3.19 (a) kinetics of CO ₂ production over FeO(111)/Pt(111) in 10 mbar CO + 20 mbar O ₂ balanced by He at indicated temperatures. (b) Arrhenius plot for the integral CO desorption signal as a function of reaction temperature.....	64
Fig. 3.20 Reaction rate (a), average stoichiometry (b) and degree of dewetting (c) of the spent FeO/Pt catalysts as a function of O ₂ pressure in the mixture with 10 mbar of CO, balance by He to 1 bar. The reaction rates measured after 120 min on stream as well as data for clean Pt(111) are also shown. The reaction temperature is 450 K.....	66
Fig. 3.21 Schematic illustration of the proposed structure transformations of the FeO/Pt(111) at different conditions.	69
Fig. 4.1 (a) Thermal desorption spectra of a pristine FeO(111) film (black line), an O-rich film produced by exposure to 20 mbar of O ₂ at RT (red) and 450 K (green) (32 amu (O ₂) signal is shown). (b) The corresponding AES spectra are shown in the same color code. The peak ratios for O(510 eV) and Fe(658 eV) are indicated.	72
Fig. 4.2 Thermal desorption spectra of a pristine Fe ¹⁸ O(111) film (a), an O-rich film produced by exposure to 20 mbar of O ₂ at RT (b) and 450 K (c). 32 amu (¹⁶ O ₂), 34 amu (¹⁶ O ¹⁸ O) and 36 amu (¹⁸ O ₂) signals are shown. The heating rate is 3 Ks ⁻¹	74

Fig. 4.3 STM images and profile lines of the FeO films exposed to 20 mbar O ₂ at 450 K for 10 min (a, c) and 2 mbar O ₂ at 300 K for 5 h (b, d). The insets show close-ups of the corresponding surfaces. The Moiré superstructure of the pristine FeO film is shown in the inset of (b). Image sizes are 100 nm × 100 nm (a) and 50 nm × 50 nm (b), tunneling bias and current were 1V, 0.7 nA (a) and 0.25 V, 0.3 nA (b). (provided by S. Shaikhutdinov and M. Lewandowski)	75
Fig. 4.4 LEED patterns (E=60 eV) of a pristine FeO film (a) and an O-rich film by exposure to 20 mbar of O ₂ at 450 K (b).....	76
Fig. 4.5 (a) 100 nm × 100 nm STM image of the FeO film exposed to 14 mbar of O ₂ at 450 K for 10 min. The inset zooms in the 3 × 3 R300 structure with respect to pristine FeO, which is more clearly observed in the image (b), presented in the differentiated contrast. (b) 100 nm × 100 nm image of the FeO film exposed to 0.5 mbar of O ₂ for 10 min at 350 K. The unit cells are indicated. Tunneling bias and current are 0.25 V, 0.7 A (a); 1.0 V, 0.7 nA (b); 0.1 V, 0.7 nA (inset), respectively. (provided by M. Lewandowski [166])	77
Fig. 4.6 (top) Energy profile for oxidation of the FeO/Pt(111) film on exposure to O ₂ at high oxygen coverage. (bottom) energy profile for CO oxidation on FeO ₂ /Pt(111) film at low CO coverage. Fe blue, O red, C yellow, Pt gray. (from [167]).....	79
Fig. 4.7 TPD spectra of NO on Pt(111) (top) and FeO(111) (bottom) as a function of NO exposure at 100 K. The heating rate is 3 Ks ⁻¹	81
Fig. 4.8 TPD spectra of the decomposition of the FeO(111) films after exposing to 20 mbar of pure NO and pure O ₂ at 300 K and 450 K for 20 min. O ₂ (32 amu) signal is monitored. The heating rate is 3 Ks ⁻¹	82
Fig. 4.9 TPD spectra of the fresh FeO films and the O-rich iron oxide films prepared by NO and O ₂ oxidation upon adsorbing saturated amount of NO (7.5 L) at 100 K. The heating rate is 3 Ks ⁻¹	83
Fig. 4.10 Kinetics of CO ₂ production over FeO(111)/Pt(111). (a) 10 mbar CO + 50 mbar NO and 10 mbar CO + 50 mbar O ₂ at 450 K (b) 10 mbar CO + 50 mbar NO at indicated temperatures. Time zero corresponds to the start of the sample heating (1 Ks ⁻¹) from 300 K.....	84
Fig. 4.11 CO (28 amu) and NO (30 amu) signals in TPD spectra of a FeO(111)/Pt(111) film reacted in 10 mbar CO + 50 mbar NO for 120 min at indicated temperatures. The spectrum of a FeO(111)/Pt(111) reacted in 10 mbar + 50 mbar O ₂ for 120 min is shown in dotted line for comparison. The heating rate is 3 Ks ⁻¹	85
Fig. 5.1 STM images of the Pt/Fe ₃ O ₄ (111) surface annealed to 600 K in UHV for 5 min at 0.8 ML Pt (a) and 2.6 ML (b) Pt coverages. Image size is 100 nm x 100 nm; tunneling bias and current are V = 1.4 V, I = 1 nA (a); 1.4 V, 0.7 nA (b). (provided by Z.-H. Qin and M. Lewandowski)	88

- Fig. 5.2 (a) TPD spectra of CO on Pt/Fe₃O₄(111) annealed at 600 K for 5 min as a function of Pt coverage as indicated. (b) TPD spectra of CO on the stepped Pt(111) surface prepared by 1 keV Ar⁺ sputtering at 300 K and annealing at 600 K for 5 min, denoted as Pt(111)_s. Subsequently, 0.1 ML of Fe were deposited onto Pt(111)_s surface and annealed for 5 min at 600 K prior to CO adsorption. TPD spectrum of CO on clean Pt(111) surface is shown in dashed line for comparison. 7.5 L of CO were dosed at 100 K in each case. The heating rate is 3 K/sec. STM Image in (b) (provided by M. Lewandowski), presented in differentiated contrast, shows a Pt(111)_s surface. Image size is 100 nm x 100 nm; tunneling bias and current are V = 0.7 V, I = 0.4 nA..... 90
- Fig. 5.3 Repeated TPD spectra of 7.5 L CO adsorbed at 100 K on 1.7 ML Pt/Fe₃O₄(111). The 28 (CO) and 44 (CO₂) amu signals are shown. 93
- Fig. 5.4 TPD spectra of 7.5 L C¹⁸O adsorbed at 100 K on Pt/Fe₃¹⁶O₄(111) surface. The 30 (C¹⁸O), 46 (C¹⁶O¹⁸O) and 48 (C¹⁸O¹⁸O) amu signals are shown. The heating rate is 3 Ks⁻¹..... 94
- Fig. 5.5 TPD spectra of 7.5 L CO on Pt/Fe₃O₄(111) surface. The sample was treated with 1500 L of CO at 450 K and 500 K. The heating rate is 3 Ks⁻¹. The insets show corresponding AES spectra (in the same color code). Formation of carbon upon exposure at 500 K is observed..... 95
- Fig. 5.6 TPD spectra of 7.5 L CO on stepped Pt(111)_s surface. The sample was treated with 1500 L of CO at 500 K. Subsequently, the sample was exposed to 540 L O₂ at 500 K and 1500 L CO at 450 K. The heating rate is 3 Ks⁻¹. The insets show corresponding AES spectra (in the same color code). Formation of carbon upon exposure at 500 K is observed. 95
- Fig. 5.7 TPD spectra of 7.5 L CO on 0.1 ML Fe/Pt(111)_s surface. The sample was treated with 1500 L of CO at 500 K. Subsequently, the sample was exposed to 540 L O₂ at 500 K and 1500 L CO at 450 K. The heating rate is 3 Ks⁻¹. The insets show corresponding AES spectra (in the same color code). Formation of carbon upon exposure at 500 K is observed. 97
- Fig. 5.8 TPD spectra of 7.5 L CO on clean Pt(111) surface. The sample was treated with 1500 L of CO at 500 K. The heating rate is 3 Ks⁻¹. The insets show corresponding AES spectra (in the same color code). Formation of carbon upon exposure at 500 K is observed. 97
- Fig. 5.9 TPD spectra of CO on Pt/Fe₃O₄(111) annealed at 600 K for 5 min as a function of Pt coverage as indicated. Then each sample was treated with 1500 L of CO at 500 K. Subsequently, the sample was exposed to 540 L O₂ at 500 K and 1500 L CO at 450 K. 7.5 L of CO were dosed at 100 K in each case. Heating rate is 3 Ksec⁻¹. The corresponding AES spectra are shown in the insets in the same color code. 99
- Fig. 5.10 STM images (provided by Z.-H Qin and M. Lewandowski) (100 nm × 100 nm) of a 2.6 ML Pt/Fe₃O₄(111) sample as deposited at 300 K and after annealing at 600 K for 5 min (a) and at 850 K for 1 min (b). The inset in (b) (provided by M. Lewandowski) shows a high resolution image presented in the

current mode to increase the contrast and to show moiré superstructure with 2.6 nm periodicity observed on the top facets due to the formation of an FeO encapsulating layer; $V= 1.4$ V, $I= 0.7$ nA. The CO TPD spectra from these samples are shown in (c) as indicated (provided by Z.-H. Qin and M. Lewandowski). The heating rate is 3Ks^{-1} . (d) Schematic presentation of Pt particles encapsulated by a FeO(111) layer.....	101
Fig. 5.11 TPD spectra of 7.5 L of CO adsorbed at 100 K on Pt/Fe ₃ O ₄ (111) annealed at 600 K for 5 min (in black) and 850 K for 1min (in red) as a function of Pt coverage as indicated. TPD spectrum of 7.5 L of CO adsorbed at 100 K on clean Pt(111) is shown in dashed line for comparison. Heating rate is 3Ks^{-1}	103
Fig. 5.12 CO ₂ production as a function of time measured on Pt/Fe ₃ O ₄ (111) at Pt coverages and CO+O ₂ partial pressures as indicated. The catalysts were annealed at 600 K (solid symbols) and 850 K (open symbols) prior to reaction. The results for pristine Fe ₃ O ₄ (111) films under the same conditions are shown for comparison. Time zero corresponds to the start of heating with a rate 1Ksec^{-1} to the reaction temperature, 450 K.....	105
Fig. 6.1 Temperature-programmed reaction profile of CO ₂ production, CO and O ₂ consumption over Pt(111) (a) and FeO(111)/Pt(111) (b) on slow heating (1Kmin^{-1}) in 40 mbar CO + 20 mbar O ₂ + 500 mbar H ₂ balanced by He to 1 bar. The reaction profile under the same conditions in the absence of H ₂ is shown in black for comparison.	109
Fig. 6.2 Kinetics of CO ₂ production, CO and O ₂ consumption over FeO(111)/Pt(111) as a function of O ₂ pressure in the mixture with 500 mbar H ₂ and 1 mbar CO, balance by He. The reaction temperature is 450 K.....	111
Fig. 6.3 Kinetics of CO ₂ production, CO and O ₂ consumption over FeO(111)/Pt(111) as a function of O ₂ pressure in the mixture with 500 mbar H ₂ and 10 mbar CO, balance by He. The reaction temperature is 450 K.	112
Fig. 6.4 Kinetics of CO ₂ production, CO and O ₂ consumption over FeO(111)/Pt(111) as a function of temperatures in the mixture with 10 mbar CO, 20 mbar O ₂ and 500 mbar H ₂ balance by He. Kinetics over Fe/Pt(111) surface at 430 K under the same conditions are also shown.	114
Fig. 6.5 LEED patterns ($E = 60$ eV) of the FeO(111) film after reaction at 450 K(left) in 40 mbar CO + 20 mbar O ₂ +500 mbar H ₂ in He and subsequently annealed in vacuum at 800 K (right).....	116
Fig. 6.6 AES spectra of the clean FeO(111) film (top), after the reaction in 40 mbar CO + 20 mbar O ₂ +500 mbar H ₂ at 450 K (middle) and subsequent annealing to 800 K for 2 min (bottom). The corresponding peak ratios for O(510 eV) and Fe(658 eV) are indicated.....	116
Fig. 6.7 TPD spectra of CO adsorbed at 100 K on the FeO(111)/Pt(111) after reaction (black line) and after step-wise UHV annealing at 600 K (red line) and 800 K (green line).	117

Fig. 6.8 TPD spectra of CO adsorbed at 300 K on FeO(111)/Pt(111) by exposure to 500 mbar H ₂ at 450 K (black line) and after step-wise UHV annealing at 600 K (red line) and 800 K (green line).	118
Fig. 6.9 AES spectra of the clean FeO(111) film (top), after the reaction in 500 mbar H ₂ at 450 K (bottom). The corresponding peak ratios for O(510 eV) and Fe(658 eV) are indicated.....	118
Fig. 6.10 TPD spectra of 7.5 L of CO adsorbed at 100 K on Pt (111) surface and 1 ML Fe precovered Pt(111) sample. Fe/Pt(111) surface was annealed at 450 K for 1 min. The heating rate is 3 Ks ⁻¹	119
Fig. 6.11 Kinetics of CO ₂ production at 450 K over FeO(111)/Pt(111) as a function of H ₂ pressure in the mixture with 10 mbar of CO and 50 mbar of O ₂ , balanced by He. The reaction data in the absence of H ₂ and in the presence of 1 mbar of H ₂ O are shown for comparison.....	120
Fig. 7.1 (a) LEED pattern (E= 60 eV) of the FeO(111) film grown on Pd(111). (b) CO ₂ production over Pd(111), FeO film on Pd(111) and FeO film on Pt(111) in 10 mbar CO + 50 mbar O ₂ balanced by He at 450 K.....	126

LIST OF TABLES

Tab. 2.1 Instrumental parameters for different reactions studied.....	37
Tab. 4.1 O-content of different iron oxide films treated by NO and O ₂ at 300 K and 450 K determined by TPD and AES measurements.	83
Tab. 6.1 CO and O ₂ conversion and O ₂ selectivity towards CO ₂ formation over FeO(111)/Pt(111) as a function of O ₂ pressure in the mixture with 500 mbar H ₂ and 1 mbar CO after 30 min of the reaction (upper) or 10 mbar CO after 60 min of the reaction (bottom), balance by He. The reaction temperature is 450 K.	110
Tab. 6.2 CO and O ₂ conversion and O ₂ selectivity towards CO ₂ formation over FeO(111)/Pt(111) as a function of temperatures in the mixture with 10 mbar CO, 20 mbar O ₂ and 500 mbar H ₂ balance by He after 30 min of reaction. Kinetics over Fe/Pt(111) surface at 430 K under the same conditions are also shown.	115
Tab. 7.1 Electron affinity of different adsorbates (eV).....	125
Tab. 7.2 Work function of different substrates (eV).....	125

1

Introduction

Heterogeneous catalysis plays a prominent role in our society, for instance, in chemical synthesis, energy storage and conversion, and environmental chemistry [1-4]. For rational design of heterogeneous catalysts, the microscopic understanding of structures and reaction kinetics of catalysts is highly demanded. This is evidenced by the 2007 Nobel Prize in chemistry awarded to Prof. Ertl, one of pioneers in introducing modern surface science techniques to the field of heterogeneous catalysis leading to a deeper understanding of the reaction mechanisms and kinetics at surfaces [5-7].

The severe difficulties in investigating heterogeneous catalysts are related to the high degree of complexity of porous, high surface area supports. In addition, surface contamination and electric charging make the use of surface science techniques difficult. The basic idea to resolve this problem is to study systems with reduced complexity. In the early 60s structurally well-defined metal single crystals such as Pt (111) have been employed. Later on, studies on stepped or defect-rich single crystals provided some insight in the role of low-coordinated surface atoms (see e.g. [8-17]). However, a variety of specific effects, such as particle size effects, environmental effects, support effects, which play a critical role on catalytic properties, cannot be investigated on these surfaces.

One approach to bridge this so-called “material gap” is to use model planar systems, which are structurally well-controlled and better mimic the complexity of the real surfaces [18-25]. The supported model catalysts consist of metal particles dispersed across the oxide films grown on metal single crystals as illustrated in Fig. 1.1. To date, many well-ordered thin oxide films can be grown on metal supports, such as iron oxides on Pt(111) [26, 27], MgO on Mo(100) [28-32], NiO on Ni(100) [33-37], SiO₂ on Mo(112) [38-40], Al₂O₃/NiAl(110) [41-44], to name a few. The preparation is typically based on the direct

oxidation of a metal single crystal or an alloy single crystal, or on the deposition and oxidation of a metal on an inert substrate single crystal. The use of thin oxide films circumvents the charging problems that often hinder studies of insulators; therefore, they are suitable for exploration with a variety of electron and ion spectroscopies, scanning tunneling microscopy (STM), etc. Once the oxide films have been prepared, metal particles could be grown on to the oxide films by physical vapor deposition (PVD) (see e.g. [18, 20, 45-57]). An oxide support often plays a critical role that goes far beyond that of the providing support for metallic nanoparticles. The support may take part in catalytic reactions, and cause several effects, such as adsorption and diffusion processes, spillover phenomena, and the so-called “strong metal-support interaction” (SMSI) (see ref. [50] and therein). The SMSI effect was originally developed as an explanation for the decreased chemisorption capacity of CO and H₂ on metal particles with high surface energy (e.g., group VIII metals) supported on reducible metal oxides (e.g., TiO₂, CeO₂, V₂O₅) [58]. Different models were proposed, such as alloy formation, electronic interactions, and, in most cases, encapsulation or decoration of the metal particles by a thin oxide layer (see refs. [59-65] and therein). However, the exact nature and stoichiometry of the oxide layer is not known.

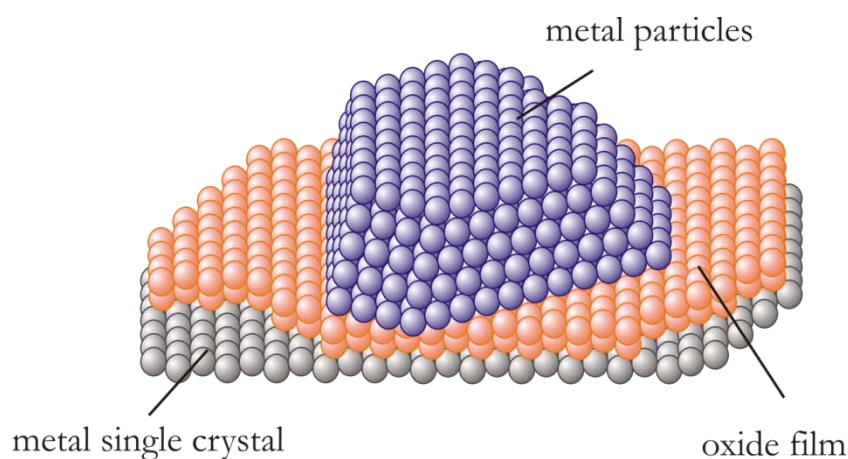


Fig. 1.1 Schematic illustration of a supported model catalyst.

In order to understand the physical nature of the metal-support interaction, a more detailed consideration of the metal-oxide interface is required. Metal-oxide interfacial contact can lead to charge redistribution at the junction: localized redistribution (among atoms at the interface) and delocalized charge transfer (between the metal and the space

region of the oxide). Minimization and the continuity of the electric potential are considered as the driving force for the charge redistribution [66].

The localized charge redistribution involves a few atomic layers at the interface. The mutual polarization of metal and oxides give rise to the van der Waals interaction, which is quite weak compared to other interactions, e.g. electrostatic interaction. This interaction is important only in the systems consisting of a wide band gap oxide, and qualitatively account for the energetics of adhesion at metal-oxide interfaces [67]. The electrostatic interaction between a metal and an oxide (mostly ionic oxide) is described by an “image charge theory” [68, 69]. At a metal-ionic oxide interface, anions and cations in the oxide induce image charges in the metal. The image theory assumes that the attractive Coulomb force between ions in the oxide and their images in the metal give rise to the interaction energy. The electrostatic field of the oxide can cause the distortion of metal valence band. This so-called polarization effect results in electron redistribution of the metal band. In the case of ultrathin oxide films on metal, the binding is dominated by the polarization effect.

The delocalized charge redistribution happens primarily between metals and the space charge regions at oxide surfaces, which is also called charge transfer. Oxides with relatively small band gap energies (usually <3.5 eV) upon intrinsic (e.g. lattice defects) or extrinsic (e.g. adsorbates) doping may produce free electronic carriers causing them to become equivalent to semiconductors. The work function of the metal support and the electron affinity of the oxide with dopants determine the direction and magnitude of the charge transfer. This process can be described using the Schottky-Mott theory [70, 71]. It stated that when a metal and a semiconductor in contact, there is no charge transfer across the interface after they are in thermal equilibrium and the Schottky barrier height, ϕ_B , is simply the difference between the metal work function ϕ_M and the electron affinity of the semiconductor χ_s :

$$\phi_B = \phi_M - \chi_s \quad (1.1)$$

However, the interface states located in the semiconductor band gap may also contribute to the Schottky barrier height, which is named Fermi level pinning after Bardeen [72]. Cowley and Sze [73] combined two situations (see Fig. 1.2) and derived the following relation:

$$\phi_B = \gamma(\phi_M - \chi_s) + (1 - \gamma)(E_g - \phi_0) \quad (1.2)$$

where E_g is the band gap energy of the semiconductor; ϕ_0 is defined as the energy measured from the edge of the valence band to the energy below which surface states must be filled for charge neutrality at the semiconductor; γ is the interface parameter:

$$\gamma = (1 + e^2 D_{is} \delta / \epsilon_{it})^{-1} \quad (1.3)$$

with δ defined as the thickness of the interfacial layer; ϵ_{it} is the permittivity of the interface layer; D_{is} is the density of interface states. For a high density of interface states (covalent solids), ϕ_B becomes independent of the metal work function ($D_{is} \rightarrow \infty, \gamma \rightarrow 0$), and is determined entirely by the doping and surface properties of the semiconductor [73]. A low density of interface states (ionic oxides), on the other hand, results in the Schottky limit ($D_{is} \rightarrow 0, \gamma \rightarrow 1$), where interface effects are neglected.

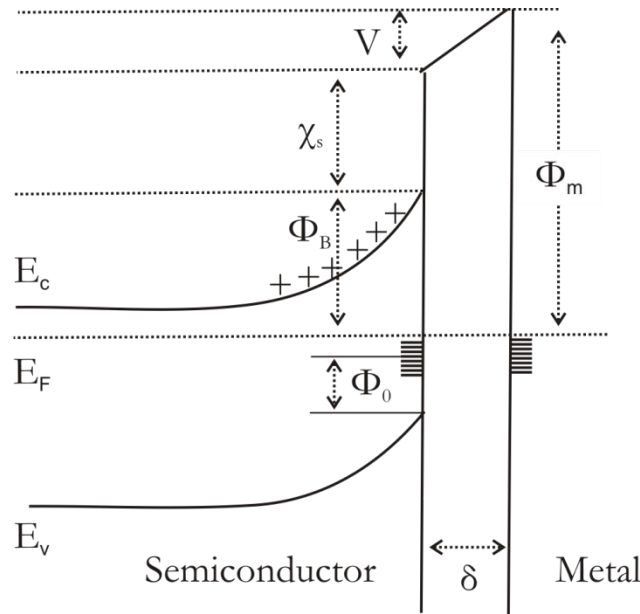


Fig. 1.2 Energy band diagram of a metal-n-type semiconductor contact with an interfacial layer [73]. ϕ_M : work function of metal, ϕ_B : barrier height of metal-semiconductor surface barrier, ϕ_0 : energy level measured from the edge of the valence band to the energy below which surface states must be filled for charge neutrality at the semiconductor, χ_s : electron affinity of semiconductor, δ : thickness of the interfacial layer, V : potential across interfacial layer.

At the close of the 1940s, these concepts used in the semiconductor theory of interfacial phenomena in solids were extended to the solid-gas contact phenomena. The charge transfer could take place as the gas species attached itself to the solid surfaces. Cabrera and Mott used these ideas to explain the formation of thin oxide films by metal oxidation at low temperatures (see Fig. 1.3) [74]. The main assumption of this theory is that electrons can pass through the oxide layer from the metal to the adsorbed oxygen by

thermionic emission or tunnel effect. This electronic motion is rapid compared with the ionic motion such that a quasi-equilibrium state is set up between the metal and the adsorbed oxygen. As a consequence the electrostatic potential V forms. A rough estimate of V is given as:

$$V = \frac{\chi_O + W - \phi_M}{e} \quad (1.4)$$

where χ_O is the electron affinity of O; W is the adsorption energy of an oxygen ion O^- on the oxide surface; ϕ_M is the work function of the metal. V is independent of the film thickness (L). This produces an electric field $F = V/L$, which may lower the energy barriers for the initiation of ionic motion and act as a driving force for interstitial metal ions or oxygen anions diffusion through the oxide layer without much help from the temperature. The Cabrera–Mott theory predicts a very rapid initial oxide growth rate followed by a breakdown at thickness $\sim 100 \text{ \AA}$.

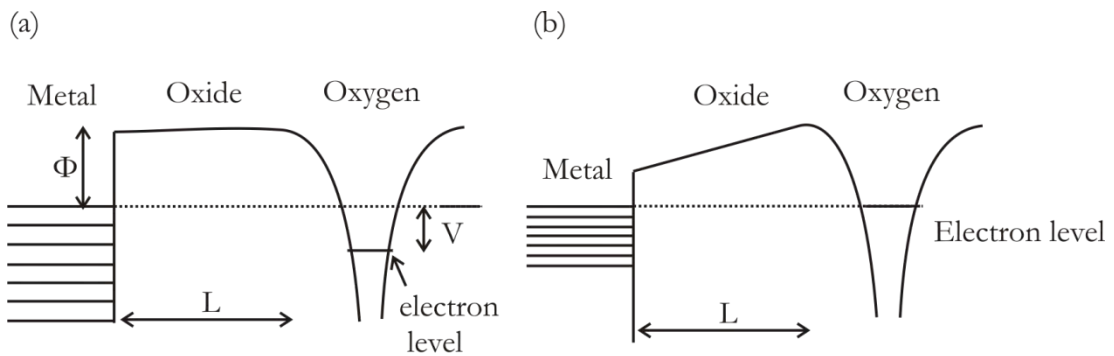


Fig. 1.3 Electronic levels in the metal, oxide and adsorbed oxygen [74]. (a) before electrons have passed through the oxide. (b) when equilibrium is reached.

Meanwhile, in the 1950s and 60s, Aigrain and Dugas [75], Weisz [76], Hauffe [77, 78], Vol'Kenshtein [79], Schwab [80] and others made great advances in developing charge transfer concepts, or electronic theory of catalysis (ETC), as it sometimes called, to explain chemisorption and catalysis on surfaces of semiconducting oxides. Essentially, ETC states that, a relationship exists between the catalytic activity of the solid and the concentration of current carriers and relative position of the Fermi level in the solid. A change in the electronic properties of a metal in contact with the semiconductor should enhance or inhibit its catalytic activity, since the catalytic act, especially the precursor stages (the chemisorption of reactants), involves the redistribution of the electron density between reactants and catalysts. Vol'Kenshtein in his review paper [79] underlined that: the semiconductor film arises as a result of oxidation of a metal, and its thickness can often be

controlled to some extent. By varying the thickness, it is possible to control the adsorption capacity, the catalytic activity, and the selectivity. It would be interesting to study the adsorption and catalytic properties of a semiconducting film on a metal, and their changes, during growth of the film. Schwab in his papers [81, 82] also proposed that inverted supported catalysts (that is, oxides on metals) would be promising to serve as potential catalysts since large number of electrons in the metallic support can easily modify the spatial distribution of electrons in thin oxide layers. Two possibilities were suggested to test this hypothesis experimentally: either by varying the thickness of the oxide layer or the work function of the metal support through alloying or entirely changing the metal [81]. For example oxidation reaction of SO_2 to SO_3 on Ag powder which was covered with a thin layer of the iron oxide ($\sim 64 \text{ \AA}$ thick) was studied. The activation energy is drastically decreased with decreasing work function of the support. ($\text{Ag+Hg} < \text{Ag} < \text{Ag+Pd} < \text{no support}$) [81]. The authors proposed the reaction goes through the step such that oxygen acts as an electron acceptor and becomes chemisorbed with a negative charge.

However the great initial interest faded considerably when this work did not evolve prompt and broadly applicable explanations of catalysis. At that time the experimental tools were not available to study ETC properly, as characterization of ultrathin film systems was not possible at the atomic level. Recent theoretical and experimental studies again revive ETC and show evidence on electronic communication between ultrathin oxides and metal substrates in the presence of adsorbed species (e.g., metal particles or molecular adsorbates) [83-88]. For example, Au atoms deposited on ultrathin MgO films supported on Mo(100) or Ag(100) substrates have been investigated by STM and density functional theory (DFT) [84, 85, 88]. It was found that electrons tunnel from the metal substrate to the deposited gold through the oxide thin film, giving rise to the negatively charged Au atoms repelling each other and forming an ordered array on the MgO surface. On the contrary, Pd atoms do not possess the charge transfer effect due to the lower electron affinity, thus residing neutrally and randomly on the same substrates. Besides metal particles, molecular adsorbates such as NO_2 was also found to be negatively charged NO_2^- upon adsorption on MgO/Ag(100) [89, 90]. Similarly, DFT predicts that O_2 is activated by MgO/Ag(100), forming negatively charged O_2^- species [91]. On the other hand, oxides on metal substrates with a large work function may favor the electron tunneling in the direction from the adsorbates to the substrate. Recently, it has been shown that Au atoms distributed orderly

on FeO/Pt(111) are in a positively charged state [92, 93]. The positive charging has also been predicted for alkali metals on oxide thin films [84, 94, 95].

Therefore, it can be concluded that the necessary condition to have the charge transfer is obtaining an energy gain in the system, which in principle is determined by the work function of metals and the electron affinity of adsorbates. The thickness of the oxide layer should also be taken into account to fully satisfy the requirement for tunneling. Obviously in case of nanometer thick films the electron transfer probability would simply be zero. However, an 8 ML oxide film differs from a 3ML film in charge transfer though the energy balance depends weakly on thickness for very thin films. This could be explained in terms of polaronic distortion: the lattice flexibility of the thin film decreases rapidly as the film grows thicker, and therefore the thin film offers opportunity to stabilize charged species by a lattice distortion, whereas a thicker film cannot [92, 96]. The structural relaxation in general is found for the supported monolayer films due to the substrate electronegativity, resulting in the film rumpling. The oxide films donate electrons to the metal substrates of high electronegativity, and anions are repelled outward (see Fig. 1.4a); whereas electrons flow from the substrates of low electronegativity to the oxide films, and cations are repelled outward (see Fig. 1.4b). Dipole moment due to the rumpling (D_R) partially compensates that due to the charge transfer at the interface (D_{CT}) [96]. Indeed, the model system FeO(111)/Pt(111) used in our work presents a pronounced substrate induced rumpling with an outward relaxation of the oxygen ions [96].

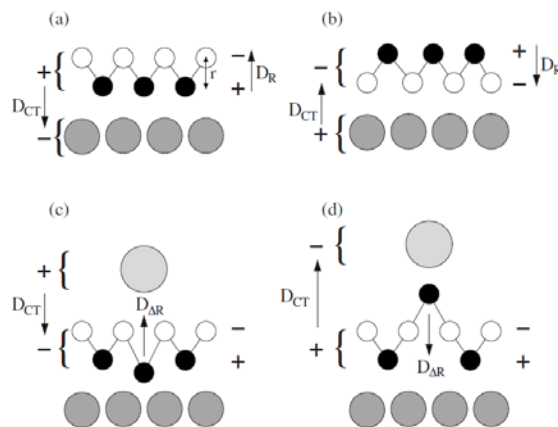


Fig. 1.4 (a)-(b) Schematic representation of the interface charge transfer and oxide film rumpling. (black circles cations, white circles anions, grey circles metal substrate). (c)-(d) Schematic representation of “direct” (c) and “flipped” (d) adsorption modes of an adatom (large circle) on a supported oxide film. (from [96])

Upon introduction of adsorbed species onto the supported oxide films, the electron flow between the adsorbates and the oxide support may cause the local distortion of the thin oxide film, which results in either reinforcing the rumpling of the oxide films or reducing, or even inverting the cation-anion stacking (see Fig. 1.4c-d) [96]. A significant local distortion of the FeO layer on Pt(111) upon Au deposition is predicted by DFT [96]. It has been found that different registries within the Moiré pattern shows different adsorption strength due to the variation of the surface potential, which may influence the interaction of adsorbates on the surface. When Au is bound on top of O anions of the FeO monolayer, the rumpling of the oxide film increases locally by about 20%. When Au is adsorbed on top of Fe cations, the effect is opposite, as the Fe ion directly below the Au atom moves from the interface outward and stands above the oxygen plane in the final flipped configuration. These two different adsorption modes are related to an opposite charge of the gold adatom, positive on top of O anions and negative on top of Fe cations, respectively.

The aim of the present thesis is to study the reactivity of well-ordered ultra thin oxide films grown on metal supports under realistic conditions (e.g. possible effects of elevated pressures and temperatures), and to provide deeper understanding of structure-reactivity relationships for ultrathin oxide films. As a strategy to study the reactivity of thin oxide films in a well-controlled manner, a suitable model system is needed. In this work, we have employed a monolayer thick FeO(111) film grown on Pt(111) single crystal. Pt catalysts (in particular, promoted by iron oxides) are widely used in many industrially important catalytic processes, and the preparation of well-ordered thin iron oxide films on Pt(111) has been established well [26, 27, 97]. As a probe reaction, CO oxidation reaction was chosen for the reactivity studies, since it has been extensively studied on transition metal surfaces and oxides, and a large amount of reference data on the reaction mechanisms exist for comparison. Particularly CO oxidation on Pt is one of the most studied reactions in catalysis on metals (see reviews [98, 99]), that proceeds via Langmuir-Hinshelwood mechanism whereby CO_2 is formed through the associative reaction of chemisorbed CO with the oxygen surface atoms produced by dissociation of molecular oxygen. The reaction has two distinct branches in the reactivity plot which is determined by a $\text{CO}:\text{O}_2$ ratio reflecting the competition for adsorption sites between CO and oxygen. At the oxygen rich conditions, the metal surface is covered by oxygen, which does not affect adsorption of

CO that readily reacts with oxygen. In contrast, the reaction exhibits low activity in excess of CO suppressing oxygen dissociation.

Very often, reactivity studies under ultra-high vacuum (UHV) conditions cannot straightforwardly be taken to explain the complex chemistry of catalysts which proceeds under high pressures and high temperatures conditions. For example, new adsorbate structures may originate under high pressure, and the catalyst surface may restructure [100-104]. In order to bridge the so-called “pressure-gap”, a high-pressure cell was added to our UHV setup. The sample was prepared and characterized at UHV conditions. For reactivity studies, the experiments were carried out on the same sample in the high-pressure cell used as a circulating batch reactor at elevated pressures up to 1 bar with a gas chromatography (GC) analysis of products.

The thesis is organized as follows:

- i. In chapter 2, experimental tools and their theoretical backgrounds are described. In addition, the preparation of iron oxide films as well as their structural information are summarized.
- ii. Chapter 3 presents results of systematic kinetics studies of CO oxidation reaction on a clean Pt(111) single crystal and iron oxide films grown on Pt(111) at different CO:O₂ ratios (between 1:5 and 5:1) and partial pressures up to 60 mbar at 400-450 K. Structural characterization of the model catalysts was performed by STM, low energy electron diffraction (LEED), Auger electron spectroscopy (AES), and temperature programmed desorption (TPD).
- iii. Chapter 4 mainly deals with the structural information of the oxygen rich iron oxide, which is considered as the key structure in the CO oxidation reaction on FeO(111)/Pt(111). In addition the oxidant effects have also been studied by replacing O₂ with NO.
- iv. Chapter 5 addresses CO oxidation on Pt particles supported on Fe₃O₄(111) films. The identification of different adsorption sites on Pt/Fe₃O₄ model catalysts is presented by using CO as a probe molecule in TPD measurements. Additionally, CO dissociation on supported Pt

particles has also been investigated. Particularly, we provided evidence on the SMSI effects via encapsulation of Pt particles with thin iron oxide layers via high temperature annealing. The effect of encapsulated thin oxide layer on reactivity has been investigated.

- v. Chapter 6 addresses the preferential oxidation reaction of CO in the presence of H₂ (PROX) on FeO(111)/Pt(111) as a case study.
- vi. Finally, the summary and outlook are provided in Chapter 7.

Methods and Materials

This chapter briefly describes the various analytical techniques and systems used in this study, including, LEED, AES, STM, TPD and GC. In addition, the preparation and structure of iron oxide films used in this work are discussed in details.

2.1. Experimental Setup

The development of modern surface and interface physics is intimately related to the advent of UHV techniques. The preparation of well-defined surfaces with negligible contamination requires ambient pressures lower than 10^{-9} mbar. The UHV system used in this work consists of a typical stainless-steel chamber as shown in Fig. 2.1, in which the base pressure is maintained below 2×10^{-10} mbar by using the pumping stations, including a rotary pump, a turbomolecular pump, a Ti sublimation pump and an ion pump, covering different pressure ranges. The rotatable x-y-z manipulator with liquid nitrogen cooling is used to put the sample in front of various analytical tools. The UHV chamber is equipped with electron beam assisted metal evaporators (Focus EFM3), Auger electron spectrometer (Omicron), LEED optics (Omicron), quadrupole mass spectrometer (QMS, Hidden) and standard facilities for sample cleaning (sputter gun and gas handling system). The gas handling system is connected to high purity gases. Before each dosing, the doser line is “washed” with this gas to avoid gas contaminating. In TPD measurements, the sample surface is exposed to specific gas molecules through a directional gas doser of a King-Wells type [105]. This doser with a $10 \mu\text{m}$ pin-hole in the Mo foil significantly reduces the base pressure in the chamber during the gas exposure as compared to dosing by back-, therefore minimizing the contamination.

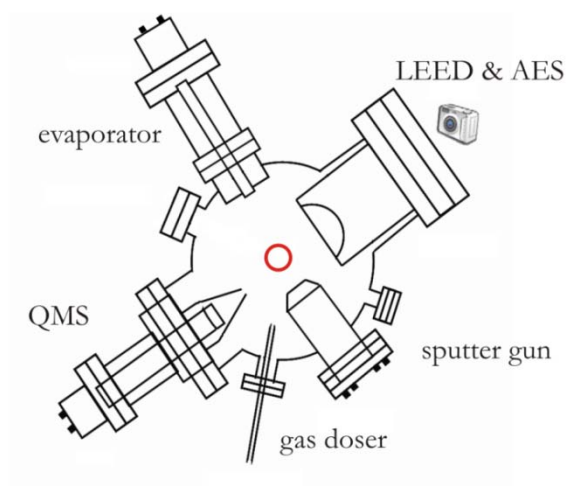


Fig. 2.1 Schematic illustration of the experimental setup.

A sketch of the sample holder used is shown in Fig. 2.2. The substrate used in the work is double-side polished Pt (111) (99.99%, Mateck) single crystal (~ 10 mm in diameter, 1.5 mm in thickness). The sample was mounted to two parallel Ta (1mm) sticks by a pair of Ta wires (0.25 mm), which were used for resistive heating and also for cooling by filling a manipulator rod with liquid nitrogen. The temperature was measured by type K thermocouples (NiCr-NiAl) spot-welded to the edge of the crystal, and controlled using a feedback system (Schlichting Phys. Instrum.). The temperature could be varied between ca. 90 K and 1500 K.

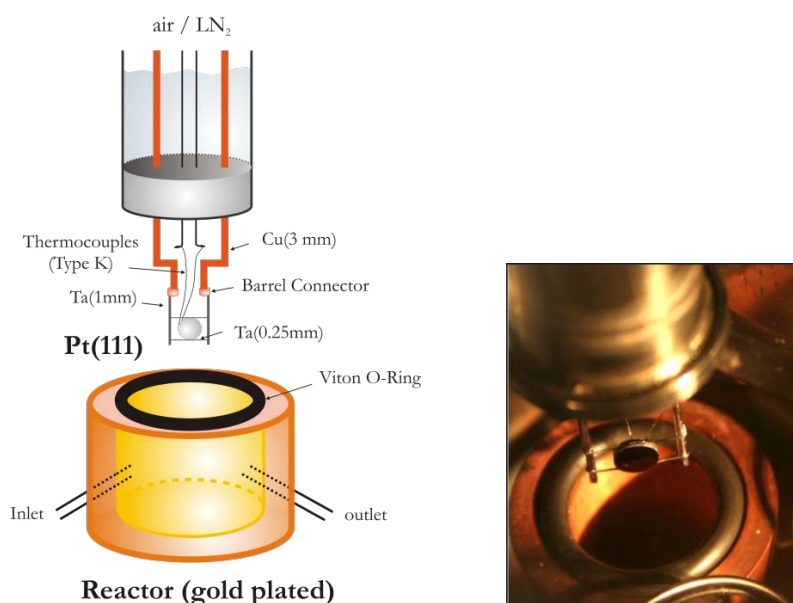


Fig. 2.2 Schematic representation of the sample holder and the reactor.

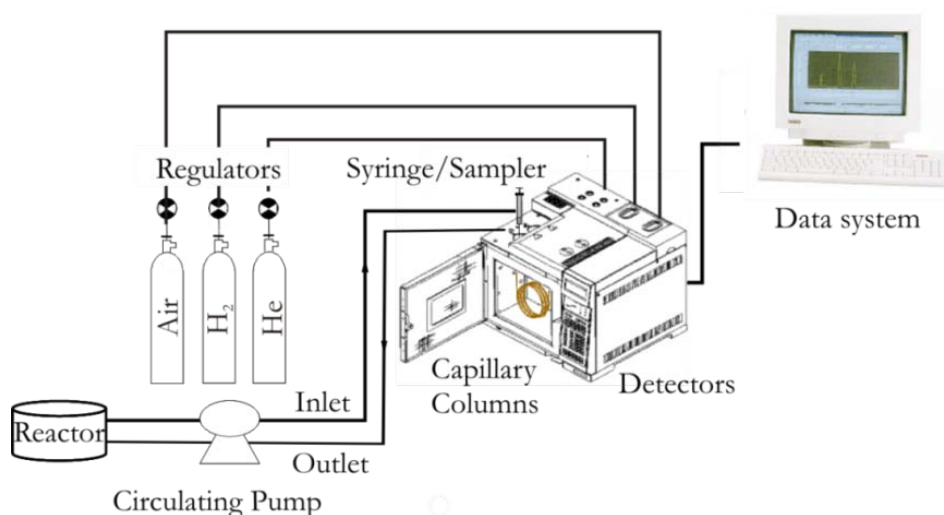


Fig. 2.3 Setup of the GC system.

To carry out the reactivity studies at realistic pressure conditions, we have built a “high-pressure” cell (~ 30 ml, made of Au-plated Cu massive block) inside the UHV chamber (see Fig. 2.2) that allowed us to monitor reaction kinetics by GC (Agilent 6890N) and to perform structural characterizations of model catalysts *ex situ*. The manipulator rod inside the chamber ends with a KF-type flange with a 4-pins electrical feedthrough holding Ta and thermocouple sticks. For high-pressure reactivity studies, the following procedures were used. The well-characterized sample was moved vertically down to the high-pressure cell, which was then sealed from the UHV chamber by using a Viton O-ring placed on top of the reactor matching the flange at the end of the manipulator. The reactor was then filled with reactants up to the desired pressure and balanced by He up to 1 bar. Meanwhile the main chamber remained in the pressure of $\sim 10^{-9}$ mbar range. For high-pressure experiments, gases (e.g. CO (99.997%) and O₂ (99.9996%), NO(99.5%) and He(99.9999%)) were additionally cleaned using a cold trap kept at 200 K. Reactants were circulating with a flow of 3 ml/min for 20 min at room temperature to get equilibrium by using a membrane pump. The sample was then heated up to the reaction temperature with a constant heating rate. The gas composition in the circulating flow was analyzed by GC using a HP-Plot Q column at 35 °C and a thermal conductivity detector (TCD) (see Fig. 2.3). After the reaction, the spent catalyst was rapidly (within 2-3 min) cooled down to room temperature, and the reactor was quickly pumped out down to $\sim 10^{-5}$ mbar (which typically took ~ 20 min) before exposing to UHV. Then the manipulator was retracted, and the post-reaction characterization was performed.

2.2. Surface Analytical Techniques

2.2.1. Low Energy Electron Diffraction (LEED)

LEED is the principal technique for the determination of the ordered structures on the surface. A typical experimental set up is illustrated schematically in Fig. 2.4. The standard LEED apparatus comprises a hemispherical fluorescent screen and an electron gun aligned along the central axis of the screen. Electrons of low energy below 300 eV are emitted from the filament with low work functions (LaB₆, W or Ir), which then follow paths along the central axis with the aid of Wehnelt and electrostatic lenses, and finally hit the sample at earth potential in order to prevent charging. The back-scattered electrons are then accelerated sharply onto the screen which is biased to 3-6 kV. The grids in front of the screen provide accurate energy selection to screen out the inelastically scattered electrons. The grid nearest the sample is grounded to allow the linear beam trajectories. The next two grids away from the sample are at a potential of several volts below the incident electron beam, therefore inelastic electrons which have lost more than a few volts cannot reach the screen. The fourth grid is again grounded to prevent the influence from the screen potential on the energy-selection grids [106].

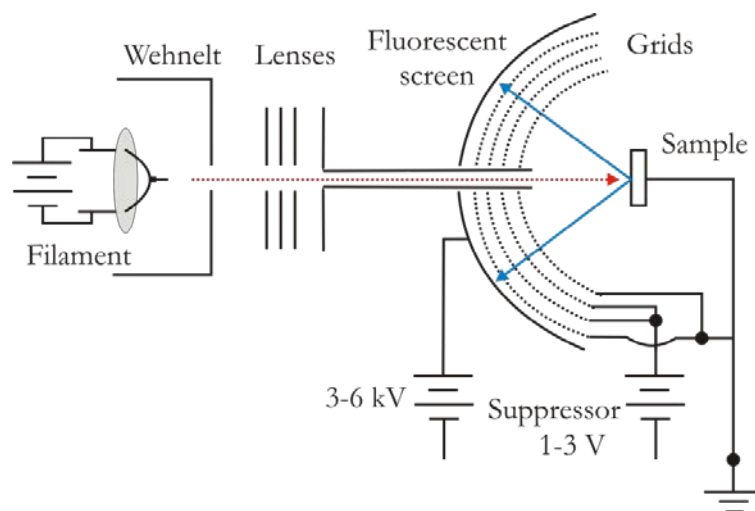


Fig. 2.4 Experimental setup of a LEED optics.

The elastically back-scattered electrons give a diffraction pattern. The energy of the diffracted electrons is typically in the range of 20-200 eV, which means the corresponding wavelength (λ) is in the range of 2.7 Å - 0.87 Å, according to the De Broglie formula:

$$\lambda = \frac{h}{p} = \frac{h}{mv} = \frac{h}{\sqrt{2meV}} \quad (2.1)$$

where $h = 6.626 \times 10^{-34} \text{ Js}$ is the Planck constant, $m = 9.11 \times 10^{-31} \text{ kg}$ is the electron mass and $e = 1.6022 \times 10^{-19} \text{ C}$ is the elementary charge. This wavelength is comparable with the atomic spacing, which is the necessary condition for diffraction effects to be observed. The waves associated with the scattered electrons undergo a constructive interference if the path difference between waves is equal to an integral multiple of the wavelength:

$$2d\sin\theta = n\lambda \quad (2.2)$$

where d is the distance between lattice planes, and θ is the angle of reflected electrons to the surface normal (see Fig. 2.5), and n is an integer number. The electron beam used at above 50 eV has typically a beam diameter of around 1 mm^2 . The instruments transfer width (which is essentially the coherence length of the electrons) is of approximately 5-10 nm in modern instruments. Naturally only structures which extent over at least $(100 \times 100) \text{ \AA}$ can produce Bragg reflexes. Structure domains with a smaller diameter than the coherence width will not constructively add to the diffraction pattern but add diffuse background intensity. The observed diffraction pattern reveals the translational symmetry and the point group of the surface in the reciprocal space [107, 108]. Fig. 2.6 shows a LEED pattern of a clean Pt(111) surface as an example.

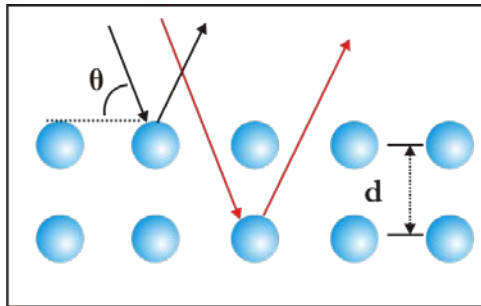


Fig. 2.5 Schematic representation of the diffraction process.

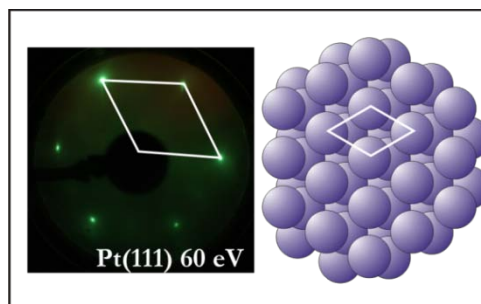


Fig. 2.6 LEED pattern ($E = 60 \text{ eV}$) and schematic structure for the clean Pt(111) sample.

The concepts for lattice and reciprocal lattice on surfaces are very similar to what we know from the bulk. In two dimensional space, the lattice vectors are spanned by two base vectors \vec{a}_1 and \vec{a}_2 , the reciprocal lattice follows from the definition of the reciprocal lattice vectors \vec{a}_1^* and \vec{a}_2^* :

$$\vec{a}_1^* = 2\pi \frac{\vec{a}_2 \times \vec{n}}{\vec{a}_1(\vec{a}_2 \times \vec{n})}, \quad \vec{a}_2^* = 2\pi \frac{\vec{a}_1 \times \vec{n}}{\vec{a}_2(\vec{a}_1 \times \vec{n})} \quad (2.3)$$

\vec{n} is the vector normal to the surface. This also means:

$$\vec{a}_i \cdot \vec{a}_j^* = 2\pi \delta_{ij} \quad (2.4)$$

$$|\vec{a}_1^*| = \frac{2\pi}{|\vec{a}_1| \sin \alpha}, \quad |\vec{a}_2^*| = \frac{2\pi}{|\vec{a}_2| \sin \alpha} \quad (2.5)$$

where \vec{a}_i are the base vectors of the real lattice ($i = 1, 2$); \vec{a}_j^* are the base vectors of the reciprocal lattice ($j = 1, 2$); δ_{ij} is the Kronecker delta, $\delta_{11} = \delta_{22} = 1, \delta_{12} = \delta_{21} = 0$; α is the enclosed angle between \vec{a}_1 and \vec{a}_2 . The diffraction conditions for a two dimensional lattice are given by the two dimensional Laue conditions:

$$(\vec{k}_i - \vec{k}_j) \vec{a}_1 = 2\pi h, \quad (\vec{k}_i - \vec{k}_j) \vec{a}_2 = 2\pi k \quad (2.6)$$

where h and k are arbitrary integers. They principally represent the conservation of energy and momentum between the incident wave vector \vec{k}_i and the emerging wave vector \vec{k}_j . This condition is fulfilled whenever $\Delta \vec{k}$ equals a reciprocal lattice vector $\vec{G} = h\vec{a}_1^* + k\vec{a}_2^*$. The energy conservation requires that $|\vec{k}_i| = |\vec{k}_j|$. These two conditions can be made visible by changing the Ewald construction known from x-ray scattering to the surface case as shown in Fig. 2.7.

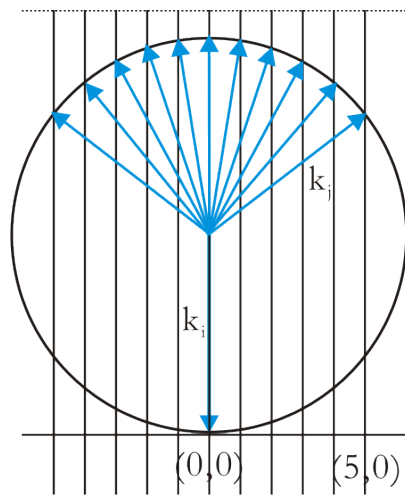


Fig. 2.7 The Ewald construction for the surface case.

An overlayer structure with a rather large unit mesh and various domains may generate a complicated pattern. The lattice vectors of the surface including possible adsorbate overlayers are characterized as \vec{b}_1 and \vec{b}_2 . A simple nomenclature of surface structures is that of Wood's. The surface structure is described by

$$N \left(\frac{b_1}{a_1} \times \frac{b_2}{a_2} \right) R\beta \quad (2.7)$$

where N= "P" or "c" for primitive or centered cells, respectively, and β is the angle by which the surface vectors have to be rotated with respect to those of the bulk (see Fig. 2.8). The nomenclature of Wood has the advantage of simplicity. It is, however, not possible to describe all surface structures because the rotation angle might not be the same for both vectors.

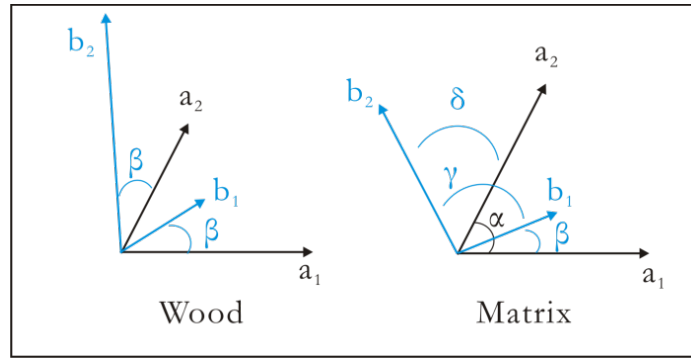


Fig. 2.8 The wood(left) and matrix (right) terminology for surface lattices. a_1 and a_2 correspond to the substrate unit cell vectors. b_1 and b_2 indicate the superstructure unit cell vectors. α is the enclosed angle between the substrate, and γ is the enclosed angle between the superstructure unit cell vectors. The angle β and δ accounts for a rotation of the superstructure with respect to the substrate.

The matrix representation of superstructures shows that \vec{b}_1 and \vec{b}_2 can be built up by the substrate unit cell vectors:

$$\vec{b}_1 = m_{11}\vec{a}_1 + m_{12}\vec{a}_2, \quad \vec{b}_2 = m_{21}\vec{a}_1 + m_{22}\vec{a}_2 \quad (2.8)$$

$$M = \begin{bmatrix} m_{11} & m_{12} \\ m_{21} & m_{22} \end{bmatrix} \quad (2.9)$$

The indices m_{ij} can be derived by simple trigonometric considerations:

$$M = \begin{bmatrix} \frac{|b_1|}{|a_1|} [\cos\beta - \sin\beta \cot\alpha] & \frac{|b_1|}{|a_2|} \frac{\sin\beta}{\sin\alpha} \\ \frac{|b_2|}{|a_1|} [\cos(\beta + \gamma) - \sin(\beta + \delta) \cot\alpha] & \frac{|b_2|}{|a_2|} \frac{\sin(\beta + \gamma)}{\sin\alpha} \end{bmatrix} \quad (2.10)$$

The meaning of the variables is illustrated in Fig. 2.8. Large overlayer unit cells together with multiple domain structures may give rather busy LEED pictures. Disentangling the various effects can become very difficult. Together with STM, from which the real space image of the surface is obtained, the analysis can become simple. Usually not all diffraction spots that should be visible are visible. This is due to the fact that at certain electron energies these spots can be almost completely extinguished. The use of a large range of reciprocal space (e.g. various beam energies) avoids false conclusions based on insufficient information.

2.2.2. Auger Electron Spectroscopy (AES)

AES is a surface-sensitive spectroscopic technique providing a fingerprint technique to identify all chemical elements except H and He [109, 110]. It is possible to use 4-grid LEED optics for AES. The physical mechanism of the Auger process is shown in Fig. 2.9. An electron beam of high energy typically of 2-5 KeV is used to ionize core levels of atoms, labeled as A. The ionized atom that remains after the removal of the core electron is in a highly excited state and will rapidly relax back to a lower energy state by one of two routes: X-ray fluorescence (process b) and Auger emission (process c). A higher level electron fills the vacant core level. The energy liberated in this process is transferred to a second electron which is called the Auger electron. The Auger electron is then emitted and the retained kinetic energy ($E_k = E_A - E_B - E_C$) is measured. Therefore, the kinetic energy of the Auger electron is independent of the primary energy. An Auger transition (ABC) is therefore described by the initial hole location (A) and followed by the locations of the final two holes (B, C). Each element in a sample gives a characteristic spectrum of peaks at various kinetic energies. The spectra are typically recorded in differentiated form using lock-in techniques as shown in Fig. 2.10.

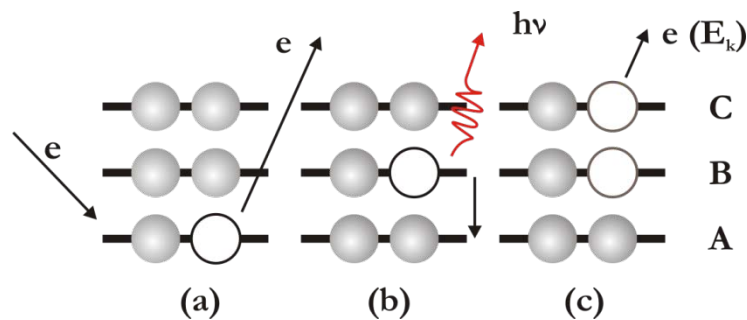


Fig. 2.9 Auger electron emission mechanism.

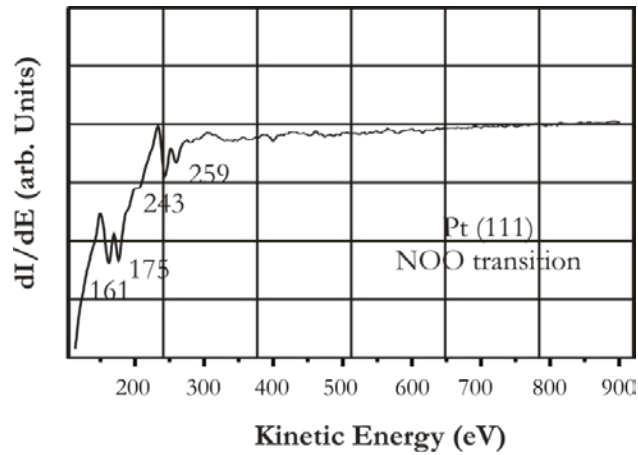


Fig. 2.10 AES spectrum of clean Pt(111) surface as an example. Primary energy: 3 keV. NOO transition is shown.

Although E_k is independent of the primary beam energy (E_p), E_p is important for obtaining optimum Auger yield. The ionization probability Q_i to form a core hole in a level of energy E_i depends on the energy of the core level as $1/E_i^2$, as well as on the ratio E_p/E_i . In order to remove an electron with a binding energy E_i one needs a primary electron of higher energy. If the primary energy is too high, the electron simply goes too fast to have efficient interaction with a bound electron in a core level. As a result, it is shown theoretically by calculating cross section that a maximum cross section is obtained when E_p is three to five times of the core electron energy [109]. Therefore, the Auger electron of the kinetic energy ranging from 50 eV to 1000 eV need the primary energy in the range 2-5 KeV. According to the so-called universal mean free path (λ) curve shown in Fig. 2.11, the Auger electron can escape from subsurface region of 1-2 nm in depth which corresponds to 3-5 atomic layers of the sample.

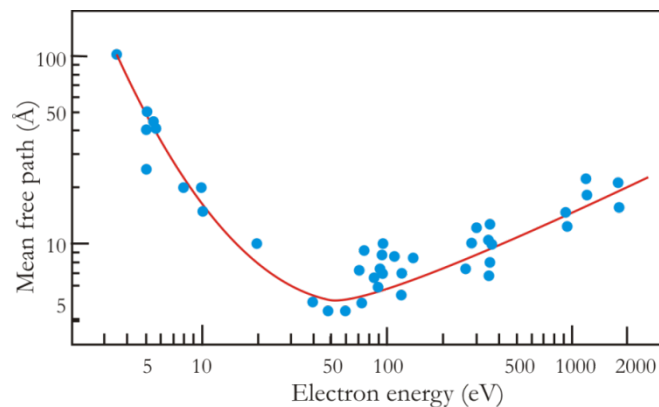


Fig. 2.11 Universal curve for electron mean free path (adapted from [111]).

A quantitative analysis of Auger spectra is easily possible, but less straightforward than in X-ray photoemission spectroscopy (XPS) due to backscattering effects [112]. For example, the Auger yield measured from a few atomic layers thick molybdenum film on a tungsten substrate is about 20% higher than that of bulk molybdenum, because the heavier tungsten is an efficient backscatterer [112]. This effect should be taken into account by multiplying the primary electron intensity I_p by a factor of $(1+R)$, where R is the backscattering factor. In general, R is higher for heavier than for lighter elements, but it may also be matrix dependent. The general expression for the Auger electron current I_A becomes:

$$I_A = I_p(1 + R)QY \int_0^{\infty} n(z)d^{-z/\lambda\cos\theta} dz \quad (2.11)$$

where Y is the probability of Auger decay; $n(z)$ is the concentration of the element at depth z ; λ is the inelastic mean free path of the Auger electron; θ is the take-off angle of the Auger electron measured from the surface normal. For a homogenous sample with the detector perpendicular to the sample surface, Eq. 2.11 reduces to

$$I_A = I_p(1 + R)QYn\lambda \quad (2.12)$$

2.2.3. Scanning Tunneling Microscopy (STM)

The scanning tunneling microscopy was first introduced in 1981 by Binnig and Rohrer [113]. Within a few years, it was quickly established as one of the most surface relevant techniques. STM is based on quantum mechanical tunneling, a phenomenon in which a particle with a given energy E is able to pass through a classically forbidden potential barrier. In the one-dimensional case, the elastic tunneling of an electron of energy E through a constant potential barrier U_0 can be described by a stationary Schrödinger equation:

$$-\frac{\hbar^2}{2m} \frac{d^2\psi(z)}{dz^2} + U(z)\psi(z) = E\psi(z) \quad (2.13)$$

The solution has the form:

$$\psi(z) = \psi(0)e^{-kz} \quad (2.14)$$

where $\psi(0)$ is the wave function of the surface state of the sample at $Z=0$; $K = \sqrt{2m(U_0 - E)/\hbar^2}$. The wavefunction ψ decays exponentially. In STM the barrier U_0 is

given by the vacuum gap between sample and tip. Then the tunneling current I can be calculated by taking into account the density of states (DOS) of the sample,

$$\rho_s(z, E) = \frac{1}{\varepsilon} \sum_{E_n=E-\varepsilon}^n |\psi_n(z)|^2 \quad (2.15)$$

At the Fermi edge:

$$I \propto V \rho_s(0, E_F) e^{-2kz} \propto V \rho_s(0, E_F) e^{-1.0252\sqrt{\phi}z} \quad (2.16)$$

where the barrier height ϕ is in eV and z in Angstrom units; V is the bias voltage. With a typical barrier height of 5 eV, the tunneling current decays by an order of magnitude when the vacuum gap is changed by 1 Å. This exponential dependence is the fundament for the high spatial resolution of the scanning tunneling microscope. Electron tunneling can occur from the metal tip to the sample surface, or vice versa, depending on the direction of the bias. When the metal tip is positive with respect to the surface, tunneling of electrons occurs from occupied surface states into empty metal states as shown in Fig. 2.12. If the potential is reversed the current flows in the other direction, the unoccupied density of states is imaged.

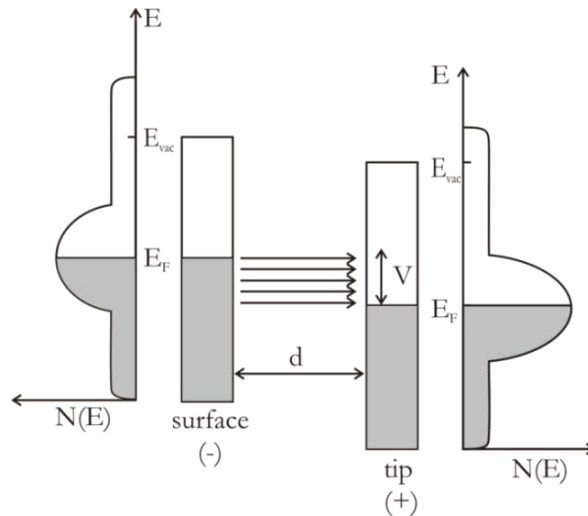


Fig. 2.12 The principle of tunneling between the surface and the metal tip for positive tip bias V . Tunneling of electrons from occupied surface states into the metal tip (adapted from [112]).

While the one dimensional example of tunneling exhibits characteristics common to tunneling in three dimensions, it does not adequately describe the physical reality of the STM tunnel junction. The Bardeen approach to tunneling considers the physical nature of the tunnel junction [114], offering grater insight into the nature of tunneling. This model assumes the wave functions of the surface states of the tip ψ_t and sample ψ_s to overlap in

order to carry out perturbation theory. The tunneling matrix element M , the transition probability from the tip state to the sample state, is then determined by the overlap of the two wave functions at some separation surface:

$$M = -\frac{\hbar}{2m} \int dS (\psi_t^* \nabla \psi_s - \psi_s \nabla \psi_t^*) \quad (2.17)$$

The integration is done over a surface S between tip and sample, through which the entire tunneling current flows. Fermi's golden rule gives the transfer rate of the electron going from one state to the other. The transition state is $|M|^2$. The probability to change states is:

$$w = \frac{2\pi}{\hbar} |M|^2 \delta(E_t - E_s) \quad (2.18)$$

where E_t and E_s is the energy of the state ψ_t and ψ_s , respectively. The δ function implies electrons can only tunnel to and from states with the same energy. As electrons can tunnel in both directions, the tunneling current can be calculated by summing over all states. At a bias voltage V , the tunneling current is:

$$I = \frac{2\pi e}{\hbar} \sum_{t,s} [f(E_t)(1 - f(E_s + eV)) - f(E_s + eV)(1 - f(E_t))] \cdot |M|^2 \delta(E_t - (E_s - eV)) \quad (2.19)$$

where $f(E) = (1 + e^{(E-E_F)/k_B T})^{-1}$ are the Fermi functions and E_t and E_s are the energies of the unperturbed wave functions of tip and sample, respectively. The Fermi functions enter here because only tunneling from an occupied to an unoccupied state is allowed.

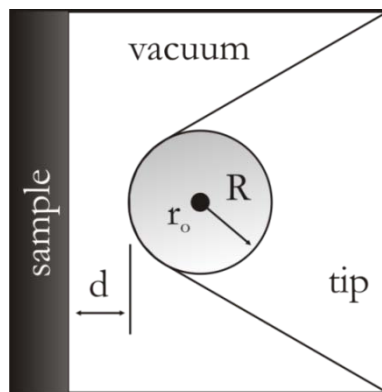


Fig. 2.13 Schematic illustration of the tunneling geometry in the theory of Tersoff-Hamann model. The tunneling tip has been approximated by a spherical potential well with the radius R . The distance of nearest approach is d . The centre of curvature of tip is r_0 . (adapted from [115])

Based on this, Tersoff and Hamann developed a simple theory of the STM [115]. One can approximate the tunneling tip to a spherical geometry with the radius R and could treat them like a metallic s-Orbital (angular momentum quantum number $l=0$). The tip geometry is illustrated in Fig. 2.13. The position vector \vec{r}_0 defines the center of the tip. The smallest distance between tip and sample is named d . For low voltage V and low temperature, Eq. 2.19 simplifies to:

$$I \propto V \rho_t(E_F) e^{2kR} \sum_{t,s} |\psi_s(\vec{r}_0)|^2 \delta(E_s - E_F) \quad (2.20)$$

where $K = \sqrt{2m\phi/\hbar^2}$, ϕ is the barrier height between sample and tip; $\rho_t(E_F)$ is the local density of states (LDOS) at E_F of the tip. The STM images the DOS at the surface of the sample close to the Fermi energy. The DOS of the tunneling tip, as well as the one of the sample surface influence the STM measurement.

Fig. 2.14 shows a schematic setup of a STM apparatus. The position of the tip (typically W or Pt/Ir) is controlled by a piezoelectric tube. Two scanning modes exist: so-called “constant height” and “constant current” modes. For all STM experiments presented in this work, the constant current mode is employed. In this mode, the feedback controller regulates the distance between surface and the tip in order to keep the tunneling current constant, while the tip scans across the surface. The corrugation as well as the local electronic structure of the surface give rise to the variation of the signal, which then gives the STM images containing topographical maps and electronic effects.

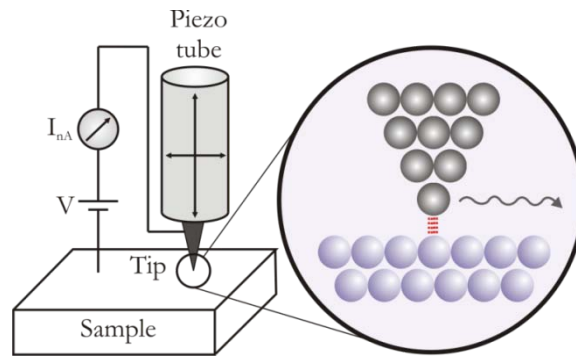


Fig. 2.14 Schematic representation of a scanning tunneling microscope.

2.2.4. Temperature Programmed Desorption (TPD)

Since TPD was one of the main techniques used in this work, more details are given in this section. In TPD studies, the sample is linearly heated, and the adsorbed species are

detected by QMS. In our setup, the mass spectrometer has a shield with a nozzle pointing towards the sample which therefore eliminates signals coming from the sample holder [116]. The sample is positioned <1 mm far from the nozzle. The lower limit of the partial pressures which can be detected with such a spectrometer is typically about 10^{-14} mbar [117].

A QMS consists of three sections as shown in Fig. 2.15. In the first ionization region, gas atoms and molecules are ionized by electrons (typically of ~ 70 eV) produced by W cathode [118]. Ions are then accelerated and focused into the second section, the mass filter, which consists of four parallel bars forming an electrical quadrupole field. The applied voltages affect the trajectory of ions traveling down the flight path centered between the four rods. For given voltages, only ions of a certain mass-to-charge ratio pass through the quadrupole filter and all other ions are thrown out of their original path. A mass spectrum is obtained by monitoring the ions passing through the quadrupole filter as the voltages on the rods are varied. The last section of the spectrometer is the ion detector which contains a secondary electron multiplier.

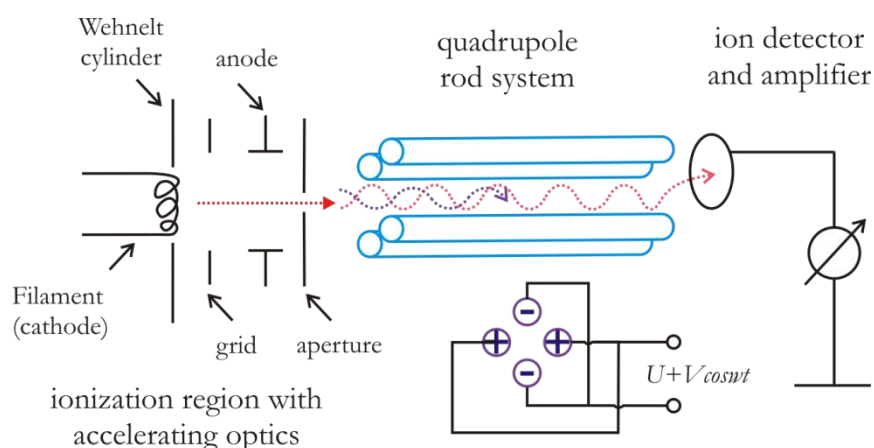


Fig. 2.15 Sketch of the quadrupole mass spectrometer.

Adsorption of atoms or molecules from the gas phase onto a solid surface occurs when attractive forces exist at short distance between them. There are two principle modes of adsorption on surfaces: physisorption and chemisorption. The basis of distinction is the nature of the bonding between atoms or molecules and surfaces. The weakest interaction which can lead to bonding between a surface and an adsorbate is the attractive van der Waals interaction, which originates from the interaction of a fluctuating dipole in the adsorbate with a polarizable surface. A van der Waals bonding between two molecules can

be described as the interaction between two point dipoles, P_1 and P_2 . In the case of bonding to a surface, the attractive potential has a r^{-3} dependence [119]. However, as the atom is brought very close to the surface, the overlapping of the electron cloud of the adsorbate and the substrate leads to a steep increase of kinetic energy of the electrons and hence a high repulsive potential [120]. A physisorption potential is the sum of the repulsive and attractive Van der Waals contributions (see Fig. 2.16, blue curves).

Chemisorption occurs when there is an overlap between the electronic orbitals of the adsorbate and the surface, leading to the formation of chemical bonds of energies typically exceeding 50 kJ/mol [39]. The bond can be predominantly ionic or covalent. There are three types of chemisorption: molecular chemisorption (a), non-activated dissociative chemisorption (b) and activated dissociative chemisorption (c) [109, 121] (see Fig. 2.16). The potential energy curve is described by a combination of the physisorption and chemisorption. The left region from the crossing point in the figure is dominated by the chemisorption. The depth of the adsorption well is a measure of the strength of the binding to the surface and is represented as adsorption energy (E_{ads}). The desorption of an adsorbed species from a surface is considered to be the reverse process of adsorption. For cases A and B, the desorption energy (E_{des}) is equal to E_{ads} . The dissociative chemisorption is often an activated process, which means that an activation barrier (E_{act}) needs to be overcome. E_{des} then can be equated:

$$E_{des} = |E_{ads}| + |E_{act}| \quad (2.21)$$

Fig. 2.16(c) shows the potential energy diagrams with an activated dissociative chemisorption process. A diatomic molecule approaching the surface from a large distance first physisorbs on the surface. If a molecule possesses kinetic energy enough to overcome the activation barrier, the molecule may dissociate. The dissociated species can be bonded to the surface in a chemisorption state. The corresponding potential curve of two atoms differs from that of the molecule at the large distance by the dissociation energy of E_{diss} .

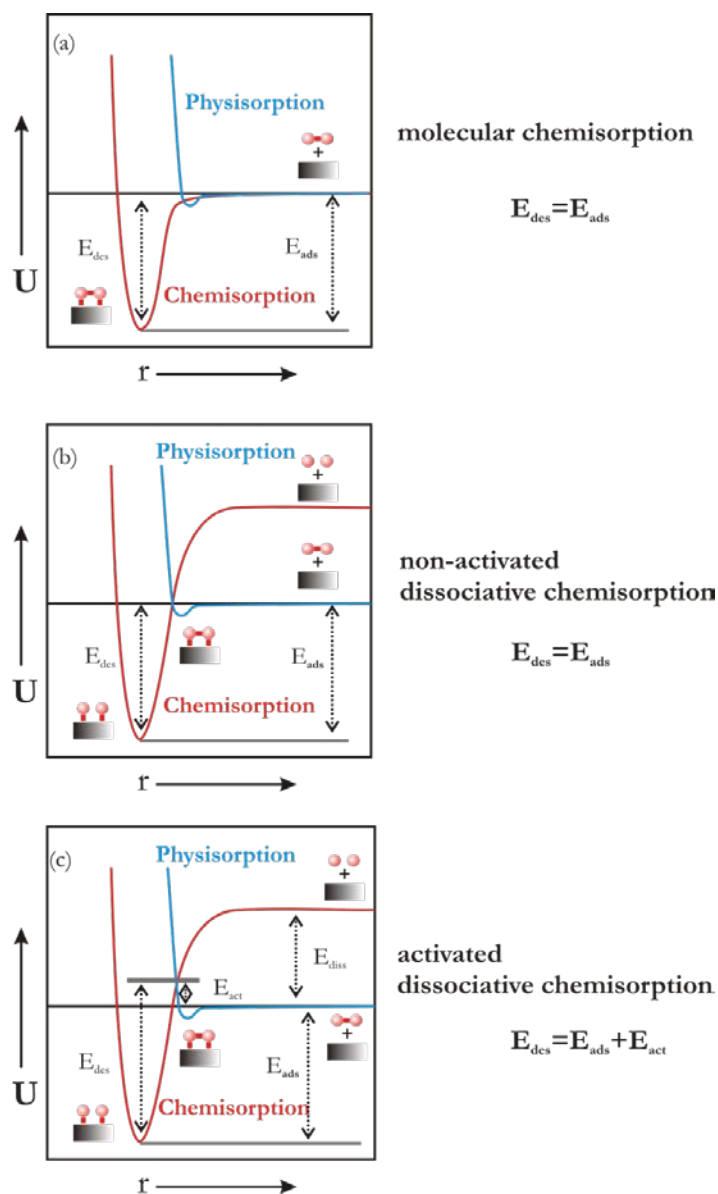


Fig. 2.16 Schematic potential diagram for the (a) molecular chemisorption, (b) non-activated, dissociative chemisorption, (c) activated, dissociative chemisorption of a diatomic molecule. Solid line curve: the total potential energy curve.

The energetics and kinetics of adsorption is obtained by analyzing the TPD data [109, 122-126]. Fig. 2.17 schematically shows a TPD spectrum. Each peak corresponds to various desorbing species. The area under a peak is proportional to the amount of adsorbed species. The position of the peak (the peak temperature) is related to the enthalpy of adsorption. TPD provides information on the strength of the bond between adsorbate and substrate.

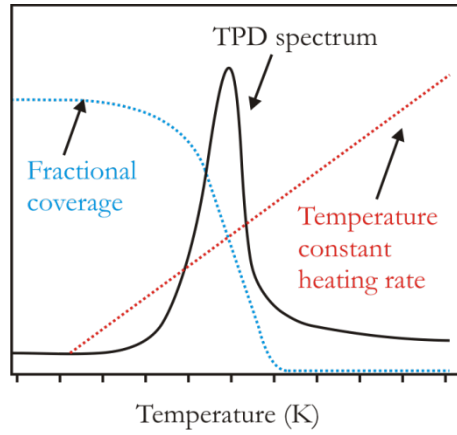


Fig. 2.17 Schematic TPD spectrum (adapted from [107]).

In 1962, Redhead presented the fundamentals of thermal desorption spectroscopy (TDS) method [126]. The surface under consideration is placed in a chamber of volume (V), which is being pumped out at a constant speed (S), and the gas is being leaked at a constant rate (L). At equilibrium, the steady-state pressure is P_{eq} , and

$$L = KSP_{eq} \quad (2.22)$$

where K represents the proportionality constant ($K = 3.27 \times 10^{19} \text{ molecule}^{-1}$, at $P = 1 \text{ torr}$ and $T = 295 \text{ K}$). Assuming no re-adsorption of the desorbing species, the mass balance gives:

$$A \frac{dN}{dt} + L = KSP + KV \frac{dP}{dt} \quad (2.23)$$

where, A is the sample area, dN/dt is the rate of desorption, and P is the instantaneous pressure inside the chamber. Using Eq. 2.22 and substituting $\Delta P = P - P_{eq}$, the Eq. 2.23 can be simplified as:

$$a \frac{dN}{dt} = \frac{d\Delta P}{dt} + \frac{\Delta P}{\tau} \quad (2.24)$$

where, $a = A/KV$ and $\tau = V/S$. τ is the characteristic pumping time. At a small pumping speed ($\tau \rightarrow \infty$), the desorption rate is proportional to the first derivative of pressure with time ($dN/dt \propto d\Delta P/dt$). Alternatively, (which the case in the most TPD studies), at a high pumping speed ($\tau \rightarrow 0$), the pressure is proportional to the desorption rate ($\Delta P = a\tau dN/dt$).

Analysis of desorption signals is based on treating the desorption process as a kinetic phenomenon. In the Polanyi Wigner model, it is assumed that the rate of desorption from a species on a surface may be written in the form:

$$-\frac{d\theta}{dt} = \nu\theta^n \exp\left(\frac{-E_d}{RT}\right) \quad (2.25)$$

where ν is the pre-exponential frequency factor, E_d is the activation energy of desorption and θ is the coverage ($0 \leq \theta \leq 1$). During TPD measurements, the temperature of the sample surface is linearly increased as $T = T_o + \beta t$. Therefore, Eq. 2.25 can be re-written as:

$$r = -\frac{d\theta}{dT} = \frac{\nu}{\beta}\theta^n \exp\left(\frac{-E_d}{RT}\right) \quad (2.26)$$

The Fig. 2.17 shows that, if the kinetics of the desorption process follows the rate law in Eq. 2.26, one would expect to observe a single peak in TPD. Initially the increasing of the temperature results in an exponential rise of the desorption rate. At the same time coverage of the surface decreases. When the coverage and temperature have the same influence on the desorption rate, a maximum desorption rate appears in the spectrum.

The TPD spectra of three different adsorbate systems, corresponding to zero-, first-, and second-order kinetics, are shown in Fig. 2.18. Zero-order desorption is the case that the desorption rate is independent of the coverage ($n = 0$). The TPD curves show the same leading edge, and the peak maximum shifts to higher temperature with increasing coverage. Fig. 2.18b shows typical TPD spectra for the first order desorption. The TPD peaks are asymmetric, but the peak maximum is independent of the initial coverage. Second order desorption process is observed in many dissociative adsorption reactions. Fig. 2.18c shows typical TPD spectra for the second order desorption. The peak positions shift with increasing coverages to lower temperatures, and the peak is symmetric.

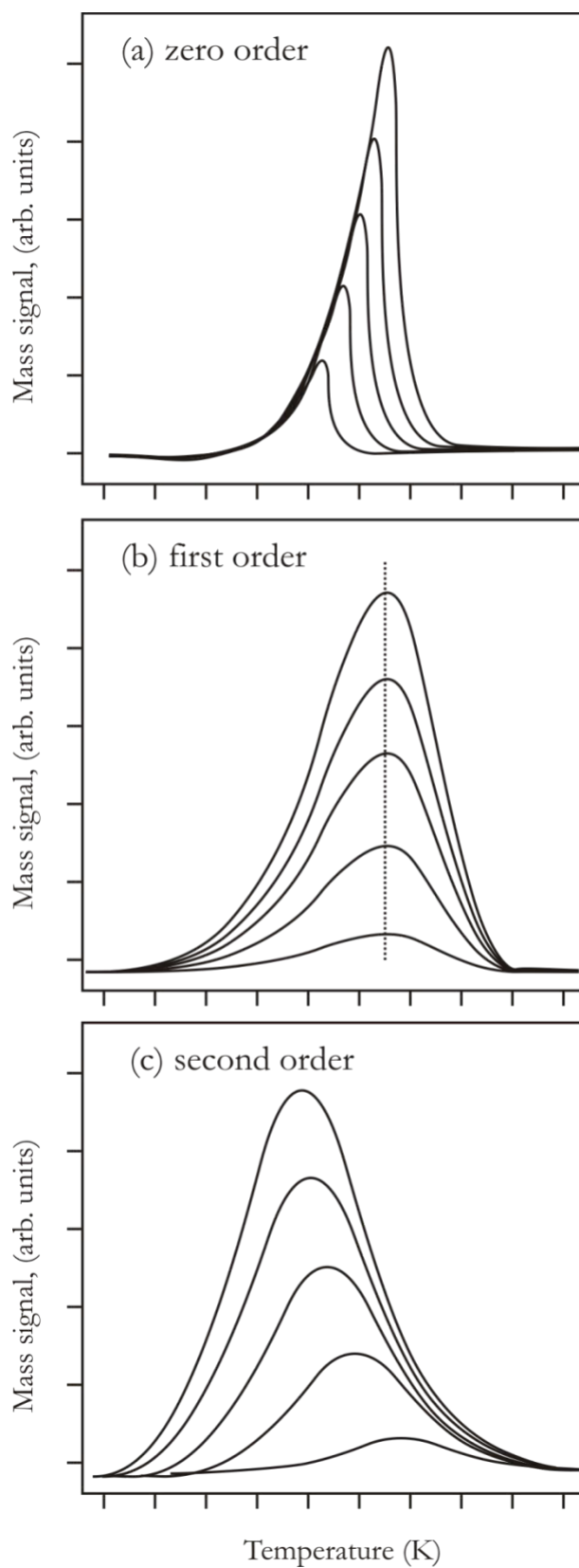


Fig. 2.18 A series of TPD curves for a zero order (a), first order (b), and second order (c) desorption process.

In the literature, several methods for evaluating the desorption activation energies, prefactors and orders of desorption have been described, including complete analysis, Redhead's analysis, and leading edge analysis.

Complete Analysis

The first complete analysis of TPD was given by King [125]. Fig. 2.19 illustrates the procedure: a coverage θ is chosen (e.g. 0.15 ML); the points corresponding to $\theta = 0.15$ ML on all TPD curves are found. This gives a pair of (r, T) values from every curve with initial coverage larger than 0.15 ML. An Arrhenius plot of all $\ln r$ versus $1/T$ values for this particular coverage yields E_d . The prefactor follows from the intercept $n \ln \theta + \ln \nu(\theta)$, when we know the order of desorption. For coverage above 0.1 ML the term $n \ln \theta$ is much smaller than $\ln \nu(\theta)$, and we could ignore it. The pre-exponential factor can be regarded as representing the frequency of attempts of the adsorbed particle to escape the chemisorptive potential. The values determined vary by at least four orders of magnitude, from 10^{12} to 10^{16} s⁻¹ [109]. This property is discussed later. If we adopt the simplest picture and set $\nu(\theta)$ equal to the frequency of vibration of the adsorbed particle, then values near 10^{13} s⁻¹ are expected.

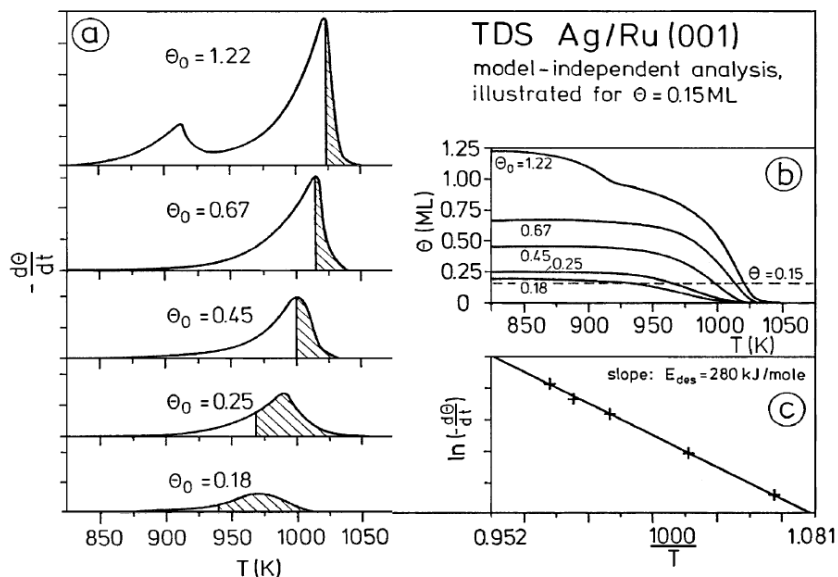


Fig. 2.19 The so-called “complete analysis” of TPD data. (a) The spectra are integrated to determine points on the spectra corresponding to a fixed coverage. (b) A pair of (r, T) values for every desorption trace are given, from which an Arrhenius plot is made. (c) The slope yields the activation energy [112].

Redhead's Analysis

Simplified analyses were published much earlier, with the so-call Redhead's analysis [126], which is based on the peak maximum temperature observed in a thermal desorption spectrum. The maximum in the desorption rate occurs when $dr/dT = 0$. Redhead has shown that the equation for $n = 1$ can be solved to obtain:

$$\frac{E_d}{RT_{max}^2} = \frac{\nu}{\beta} \exp\left(\frac{-E_d}{RT_{max}}\right) \quad (2.27)$$

The relation between E_d and T_{max} can be shown:

$$E_d = RT_{max}(In\nu T_{max} - In\beta - 3.64) \quad (2.28)$$

The calculation of activation energy using this method is generally valid for first-order desorption. A reliable pre-exponential frequency factor ν is typically set to 10^{13} s^{-1} .

Leading Edge Analysis

The leading edge analysis of TPD spectra is given by Habenschaden and Küppers [123]. It is expected that in this small temperature range ($\sim 4\%$ of spectra), the variation of ν can be neglected, and θ is close to the initial coverage. The leading edge of the TPD curve fits Eq. 2.25. The desorption rate is proportional to the intensity of the TPD trace. Here the equation becomes:

$$-\frac{dP}{dt} = A\nu\theta^n \exp\left(\frac{-E_d}{RT}\right) \quad (2.29)$$

where A is proportionality constant. Taking logarithms of both sides of this equation leads to:

$$In\left(-\frac{dP}{dt}\right) = nIn\theta + InA + In\nu - \frac{E_d}{RT} \quad (2.30)$$

The slope of this line can then be used to determine the desorption energy. Bolina et al. [127] suggested a method to obtain a desorption order. In TPD experiments it is not possible to measure an absolute coverage, however integrating the area under the TPD peaks does allow a relative coverage θ_{rel} , to be obtained. Hence Eq. 2.30 can now be rewritten:

$$In\left(-\frac{dP}{dt}\right) = nIn\theta_{rel} + InA + In\nu - \frac{E_d}{RT} \quad (2.31)$$

plotting a graph of $ln(-dP/dt)$ against $In\theta_{rel}$ at a fixed temperature. The gradient of such a plot is n .

Transition State Theory

The transition state theory of reaction rates gives the link between macroscopic reaction rates and molecular properties of the reactants, such as translational, vibrational, and rotational degrees of freedom. The desorption of a molecule M proceeds:



where M_{ads} is the adsorbed molecule; M_{ads}^\ddagger is the molecule in the transition state for desorption; K^\ddagger is the equilibrium constant for the excitation of M_{ads} into the transition state; k is the Boltzmann's constant; h is the Planck's constant; T is the temperature; M_{gas} is the molecule desorbed in the gas phase. For desorption, the reaction coordinate is the vibration of the molecule with respect to the substrate. The chance that the adsorption bond breaks is given by the factor kT/h . Therefore the rate constant of desorption in the transition state theory is:

$$K_{des} = K_1 \cdot K_2 = K^\ddagger \cdot \frac{kT}{h} = \frac{Q^\ddagger}{Q} e^{-\Delta E/RT} \frac{kT}{h} \quad (2.33)$$

where Q^\ddagger is the partition function of M_{ads}^\ddagger , Q is the partition function of M_{ads} , ΔE is the adsorption energy. The partition function Q contains translational, vibrational and rotational terms:

$$Q = Q_{trans} \cdot Q_{vib} \cdot Q_{rot} \quad (2.34)$$

$$Q_{trans} = l \frac{\sqrt{2\pi mkT}}{h}; \quad Q_{vib} = \frac{1}{1 - \exp(-h\nu/kT)}; \quad Q_{rot} = \frac{8\pi^2 I kT}{h^2} \quad (2.35)$$

where l is the characteristic linear dimension of an adsorption site; m is the mass of the molecule M . ν is the vibrational frequency; I is the moment of inertia of the molecule M . The total partition functions are the products of each terms for each individual translation, vibration and rotation. The simplest case arises if the partition functions Q and Q^\ddagger are almost equal. This corresponds to a transition state that resembles the ground state of the adsorbed molecule. The activation energy E_{act} equals to $\Delta E + kT$. According to the definition of the activation energy:

$$E_{act} = -RT^2 \frac{\partial}{\partial T} \ln K_{des} \quad (2.36)$$

Comparison with Eq. 2.33 results in the prefactors equals to $\frac{ekT}{h}$, $1.6 \times 10^{13} s^{-1}$. Higher pre-exponential factors are obtained when the molecule rotates or moves in the transition

state, indicating rather loose transition state, for example the prefactors for desorption of CO from Ru(001) is in the range of 10^{15} to 10^{16} s⁻¹ [128].

2.3. Gas Chromatography (GC)

GC is one of the most versatile and ubiquitous analytical techniques in the catalytic laboratories. It is a common type of chromatography used in analytic chemistry for separating and analyzing compounds that are gas or can be vaporized without decomposition.

After sample injection, the carrier gas, usually a chemically inert gas such as argon, helium or nitrogen, sweeps the vapor constituents through the column. Separation occurs as the gas components possess different retention time and reach the detector in sequence. The total retention time t_R is equal to the mobile phase residence time t_M , plus the stationary phase residence time t'_R (*adjusted* retention time):

$$t_R = t'_R + t_M \quad (2.37)$$

This t_M can be written as follows:

$$t_M = \frac{L}{\bar{\mu}} \quad (2.38)$$

where L is the column length and $\bar{\mu}$ is the average carrier gas velocity. During the periods when a substance is in the mobile phase, it is moving toward the detector at the same velocity as the carrier gas. Therefore, all substances spend the same length of time t_M in the mobile phase. The time spent in the stationary phase will therefore be important for separation. The retention factor K defined as the time the substance spends in stationary phase relative to the time it spends in mobile phase:

$$K = \frac{t'_R}{t_M} \quad (2.39)$$

K is partly related to the thermodynamic parameters governing the distribution process of the compound into the mobile and stationary phase. The higher value of K is, the better a separation can be (see Fig. 2.20).

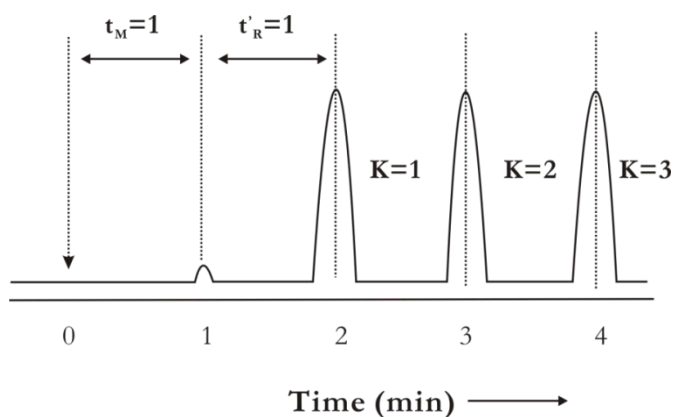


Fig. 2.20 Illustration of retention factor K .

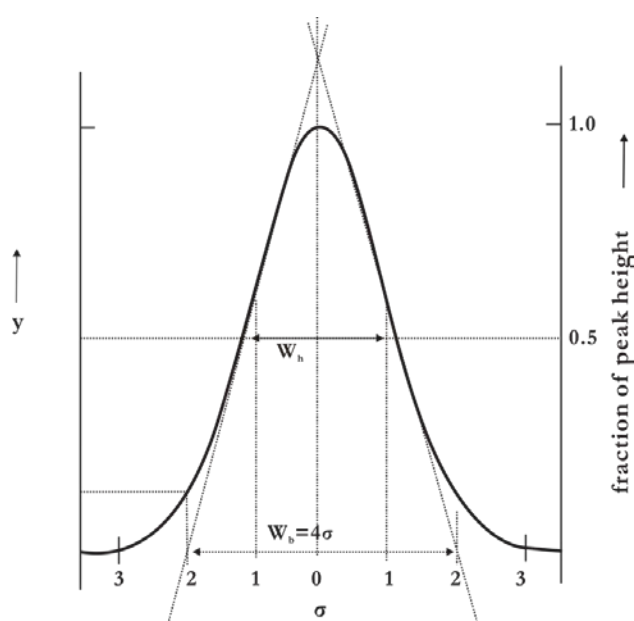


Fig. 2.21 A normal distribution. The quantity w_h is the width at 0.5 of the peak height and corresponds to 2.354σ . The quantity w_b is the base width and corresponds to 4σ as indicated.

The separation efficiency of a gas chromatographic column N is related to the degree of band broadening σ relative to the time the band requires to traverse the column t_R [129]. N is also called the number of *theoretical* plates, and is defined as:

$$N = \left(\frac{t_R}{\sigma}\right)^2 \quad (2.40)$$

To simplify the system and determine σ , the peak is assumed to be Gaussian. For a Gaussian peak, peak width at base $w_b = 4\sigma$, and peak width at half height $w_h = 2.354\sigma$, (see Fig. 2.21) which gives the following relationship:

$$N = \left(\frac{t_R}{\sigma}\right)^2 = 16\left(\frac{t_R}{w_b}\right)^2 = 5.545\left(\frac{t_R}{w_h}\right)^2 \quad (2.41)$$

If we further consider the non-negligible time for substances in the mobile phase, this gives the *effective* theoretical plates:

$$N_{eff} = \left(\frac{t_R - t_M}{\sigma}\right)^2 = \left(\frac{t'_R}{\sigma}\right)^2 = 5.545 \left(\frac{t'_R}{w_h}\right)^2 = N \left(\frac{K}{K+1}\right)^2 \quad (2.42)$$

This equation indicates that the increase of the velocity of the mobile phase raises the number of *effective* plates, and eventually improve the separation efficiency.

By definition the degree of separation *resolution* (R_s) between a critical pair of components can be expressed as:

$$R_s = \frac{2(t_{R2} - t_{R1})}{w_{b1} + w_{b2}} = \frac{t_{R2} - t_{R1}}{4\sigma} \quad (2.43)$$

where t_{R2} and t_{R1} are the retention times of the second and first peak of the critical pair in the chromatogram. w_{b1} and w_{b2} are the baseline width of the peaks. The ratio of the *adjusted* retention time of two components is termed the separation factor,

$$\alpha = \frac{t'_{R2}}{t'_{R1}} = \frac{K_2}{K_1} \quad (2.44)$$

The resolution can be rearranged to yield:

$$R_s = \frac{\sqrt{N}}{4} \frac{\alpha - 1}{\alpha} \frac{K'}{K' + 1} \quad (2.45)$$

where K' is the average of the retention factors of the peaks. In practical terms, resolution is effectively complete for $R \geq 1.5$ [129]. To obtain high resolution, the three terms must be maximized. An increase in N , the number of theoretical plates, by lengthening the column leads to an increase in retention time and increased band broadening(not desirable). Instead, to increase the number of plates, the height equivalent to a theoretical plate can be reduced by reducing the size of the stationary phase particles. It is often found that by controlling the retention factor K , separations can be greatly improved. This can be achieved by changing the oven temperature. The selectivity factor, α , can also be manipulated to improve separations. When α is close to unity, optimising K and increasing N is not sufficient to give good separation in a reasonable time. In these cases, K is optimized first, and then α is increased by one of the following procedures: changing mobile phase composition, column temperature and composition of stationary phase.

The most important factor in gas chromatography is the selection of the proper column (stationary phase) for the particular separation to be performed. The nature of the

stationary phase will determine the exchange equilibrium with the sample components, such as polarity, absorbability and so on. There are two types of columns used in GC, packed column and capillary columns, and the latter provide advantages of high resolution with narrow peaks, short analysis time, and high sensitivity [130]. Specifically the capillary PLOT-Q and PLOT-MOLSIEV columns are used in our reactivity studies. PLOT-Q column contains polystyrene-divinylbenzene and has been developed for the separation via the variation in the polarity of different compounds, for instance permanent gases, as well as volatile hydrocarbons. PLOT-MOLSIEV column is designed for the analysis of permanent gases.

Usually the detector contains a reference side and a sampling side. The response of the sampling side relative to the reference side signal is fed to a recording device where the chromatographic peaks are recorded as a function of time. By measuring the retention time and comparing this time with that of a standard of the pure substance, it may be possible to identify the peak. The area under the peak is proportional to the concentration, and so the amount of substance can be quantitatively determined. The detectors used in our work are TCD and flame ionization detector (FID).

For TCD detector, as a gas is passed over a heated filament wire, the temperature and thus the resistance of the wire will vary according to the thermal conductivity of the gas. The change in the resistance, which is proportional to the concentration of the sample component in the carrier gas, is registered on the recorder. The TCD is particularly useful for the analysis of gaseous mixtures, and of permanent gases such as CO₂ [130]. Hydrogen and helium carrier gases are preferred with TCD because they have a very high thermal conductivity compared with most other gases, and so the largest change in the resistance occurs in the presence of sample component gases (helium is preferred for safety reasons). The advantages of thermal conductivity detectors are their simplicity and approximately equal response for most substances. Also, their response is very reproducible. They are not the most sensitive detectors, however.

Most organic compounds form ions in a flame, generally cations such as CHO⁺. This forms the basis of an extremely sensitive detector, FID [130]. The ions are collected by a pair of oppositely charged electrodes. The response depends on the number of carbon atoms in the sample and on the oxidation state of the carbon. Those atoms that are completely oxidized do not ionize, and the compounds with the greatest number of low

oxidation state carbons produce the largest signals. This detector gives excellent sensitivity, permitting measurement of components in the ppb concentration range. This is about 1000 times more sensitive than the thermal conductivity detector. The carrier gas is relatively unimportant. Helium, nitrogen, and argon are most frequently employed. The FID is insensitive to most inorganic compounds, including water. The instrumental parameters used in this study is shown in Tab. 2.1.

Tab. 2.1 Instrumental parameters for different reactions studied.

CO +O₂ and CO+NO reactions	
Circulating time	20 min (RT)
Column	HP-PIOT Q, 0.53 mm × 30 m × 40 μm
Oven	35 °C, isothermal
Carrier Gas	Helium 3.0 mL/min
Detector	TCD, 250 °C
Sampling	Every 5 min

CO +O₂ +H₂ reaction	
Circulating time	20 min (RT)
Column	HP-PIOT Q, 0.53 mm × 30 m × 40 μm HP-MOLSIEV, 0.53 mm × 30 m × 25 μm
Oven	40°C, 3 min $\xrightarrow{50^{\circ}\text{C}/\text{min}}$ 100 °C, 4.8min $\xrightarrow{20^{\circ}\text{C}/\text{min}}$ 40°C
Carrier Gas	Helium 5.0 mL/min
Detector	TCD, 250 °C
Sampling	Every 15 min

2.4. The Iron Oxide Films on Pt(111)

The epitaxial growth of iron oxide films has been extensively studied, originated by Somorjai and coworkers [26, 27] and continued in detail by Weiss and coworkers [97]. The close-packed surfaces of three iron oxides (FeO, Fe₃O₄ and Fe₂O₃) can all be grown on Pt(111) single crystal. In our study we focus on well ordered FeO (111) and Fe₃O₄ (111) films.

The knowledge of the bulk crystal structures of oxides is a necessary prerequisite for a detailed understanding of the geometric structure of metal-oxide surfaces. A century of X-ray crystallography work provides excellent reference database on almost every known

crystalline materials. In the following section, an individual description of the bulk crystal structure of wüstite (FeO) and magnetite (Fe₃O₄) is given.

In the literature six iron oxides have been reported. These are FeO (wüstite), Fe₃O₄ (magnetite), α -Fe₂O₃ (hematite), γ -Fe₂O₃ (maghemite), β -Fe₂O₃ and ϵ -Fe₂O₃ [131]. They are stable over a certain range of temperatures and pressures as shown in the phase diagram for the Fe-O system depicted in Fig. 2.22.

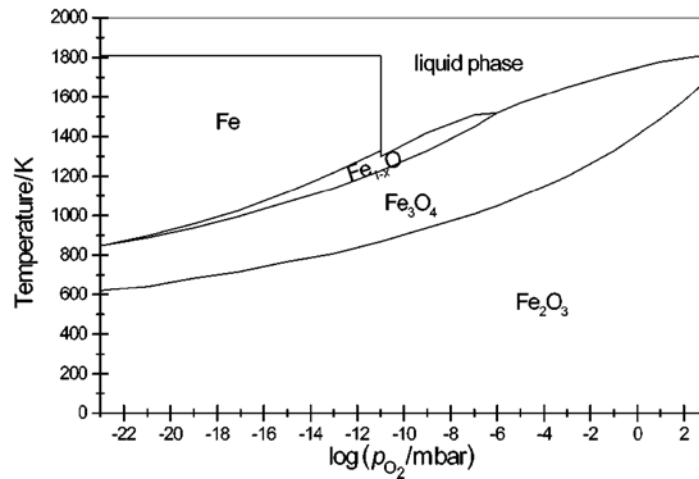


Fig. 2.22 P(O₂)-T phase diagram of Fe-O₂ system [132].

Wüstite (FeO), consisting of divalent Fe, is usually non-stoichiometric (Fe-deficient), forming Fe_xO, with x ranging from 0.83 up to 0.95, which is caused by an oxidation of Fe²⁺ ions to Fe³⁺ in order to maintain electrical neutrality [133]. Wüstite is stable only at the temperature above 843 K, and below this temperature it disproportionates into metallic Fe and Fe₃O₄. Therefore, this oxide can be only obtained by preparations at the temperature above 843 K and sequentially quenching down to room temperature [131].

The structure of wüstite is similar to sodium chloride (NaCl), consisting of four formula units in the cubic unit cell [131]. It contains an fcc close packed lattice of large oxygen anions, providing octahedral interstitial Fe²⁺ sites. In this oxide, the Fe-O bond length is 2.16 Å [131]. The two-dimensional cells formed by O and Fe on the hexagonal (111) planes with an interlayer distance of 1.25 Å exhibit an interatomic distance of 3.04 Å [131], which is considered as the lattice constant of the hexagonal unit cell of the unreconstructed FeO(111) surface as indicated in Fig. 2.23.

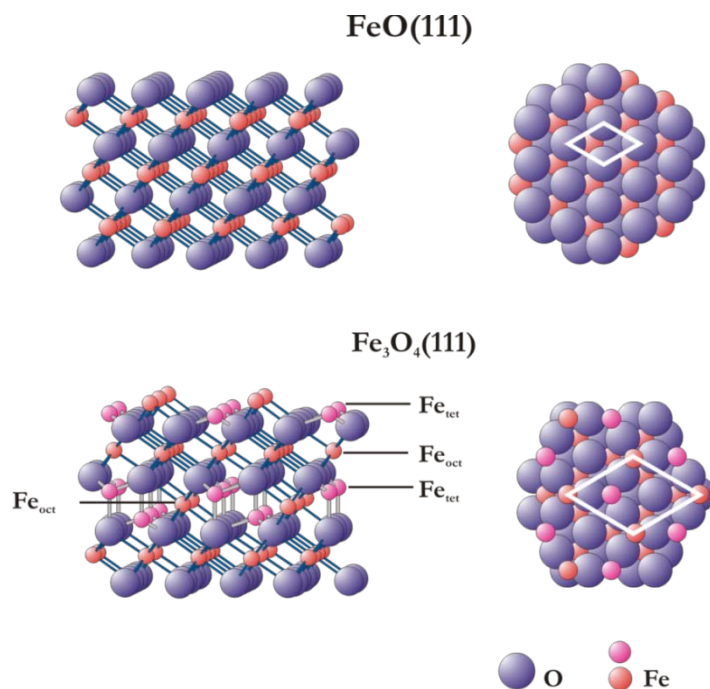


Fig. 2.23 Schematic representation of the side view (left) and top view (right) of FeO(111) and Fe₃O₄(111) crystals.

Magnetite (Fe₃O₄) is an inverse spinel that contains both divalent and trivalent iron [131]. Its formula is written as Y[XY]O₄, where X=Fe²⁺, Y=Fe³⁺. The cubic unit cell contains eight formula units and has a lattice constant of 8.39 Å [131]. The O anions form a close-packed fcc sublattice with Fe²⁺ and Fe³⁺ cations located in the interstitial sites. Fe²⁺ cations reside in octahedral sites, whereas Fe³⁺ cations occupy both tetrahedral and octahedral sites.

The (111) surface plane of bulk Fe₃O₄ is stable and frequently occurs on naturally grown crystals. Fig. 2.23 displays the structure of Fe₃O₄(111). The O and Fe hexagonal layers alternate with each other along this axis. The Fe–O bond length for tetrahedrally coordinated Fe is 1.88 Å, whereas that for octahedrally Fe is 2.07 Å [131]. The lattice constant of the two-dimensional surface unit cell of Fe₃O₄(111) is 5.94 Å [131].

The growth of iron oxide films on Pt(111) substrates follows a Stranski-Krastanov mode, with initial layer-by-layer growth of FeO(111) films and subsequent island growth of Fe₃O₄(111) films. The FeO film is limited to a maximal thickness of 2.5 ML at low oxidation temperatures (< 800 K), mainly because of the surface energy, which increases with the number of iron oxide layers [97]. In our study, well-ordered ultrathin FeO(111) films were grown onto clean Pt(111) surfaces by depositing 1ML Fe at 100 K and

annealing at 1000 K in 1×10^{-6} mbar O_2 for 2 min. CO TPD on FeO(111)/Pt(111) ($\theta \leq 1ML$) is used for calibrating the coverage of FeO films, since CO only adsorbs on the Pt(111) surface at the temperature above 100 K in this system. Using the TPD spectrum for CO/Pt(111) as a reference, the integrated area of CO desorption signal from FeO films gives the percentage of the area of open Pt(111).

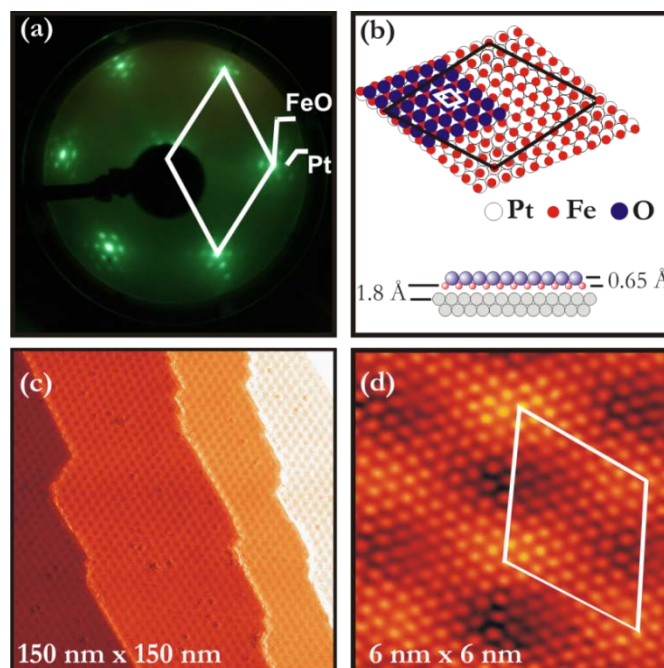


Fig. 2.24 (a) LEED pattern of FeO(111)/Pt(111) at 60 eV; (b) cross and top views of an FeO(111) film on Pt(111); (c-d) STM images of FeO(111)/Pt(111) in different sizes, $V=0.8$ V, $I=0.5$ nA (provided by M. Lewandowski); the unit cells of FeO and Moiré superstructure are indicated.

A typical LEED pattern for FeO (111) film is shown in Fig. 2.24a. The corresponding Pt substrate spots are still visible as indicated, forming Pt(111)-(1 \times 1) surface unit cell with a lattice constant of 2.77 Å [97]. The six main bright spots superimposed on the hexagonal Pt(111) pattern come from the hexagonal FeO bilayer with O termination and has the lattice constant of 3.10 Å [97]. Each main spot is surrounded by the satellite diffraction spots due to the formation of large Moiré superstructure between hexagonal lattices of FeO(111) and Pt(111). It can be described by $(\sqrt{84} \times \sqrt{84}) R10.9$ or by $\begin{pmatrix} 8 & 2 \\ -1 & 10 \end{pmatrix}$ superstructure cells using the Wood or matrix notation, respectively [97].

The LEED observation is in line with the STM results as shown in Fig. 2.24c-d with a large scale $150 \text{ nm} \times 150 \text{ nm}$ and a $6 \text{ nm} \times 6 \text{ nm}$ atomic-resolution image. The film

consists of large, atomically flat terraces exhibiting Moiré superstructure with a periodicity of $\sim 25 \text{ \AA}$. The hexagonal unit cell exhibits a lattice constant of $\sim 3.1 \text{ \AA}$. The rigid model for FeO(111)/Pt(111) structures is displayed in Fig. 2.24b. It consists of a O-terminated FeO(111) bilayer on top of the Pt(111) surface, which has a lattice expansion of 2 % as compared to the FeO bulk structure (with a lattice constant of 3.04 \AA as mentioned above). The bulk FeO(111) surface is unstable due to the dipole moment normal to the surface. However the polar instability can be compensated by the structural transformation driven by the metal substrate underneath the FeO(111) film [134]. Indeed combined photoelectron diffraction, STM and theoretical calculations found that the lattice expansion is additionally accompanied by reductions of the Fe-O interplane distance, changing from 1.26 \AA to 0.68 \AA for 1 ML FeO [135], as well as the Fe-O bond length, from 2.16 \AA to 1.8 \AA [136].

On top of FeO films, by cycles of iron deposition (5 ML, RT) and oxidation (1×10^{-6} mbar 5min, 875 K), the iron oxide then continues to grow, resulting in the formation of three-dimensional Fe_3O_4 islands, which coalesce with increasing coverage, forming a closed Fe_3O_4 oxide film with atomically flat, more than 100 nm wide terraces and steps of 4.8 \AA (or a multiple thereof) in height as shown in the STM image in Fig. 2.25b. The Fe_3O_4 films prepared for this study are at least 10 nm thick. Fig. 2.25a displays the LEED pattern of an $\text{Fe}_3\text{O}_4(111)$ film, showing quasi $p(2 \times 2)$ -FeO(111) diffraction pattern with lattice constant of 5.92 \AA , which is identical to bulk $\text{Fe}_3\text{O}_4(111)$ surface. The unit cells of Fe_3O_4 are aligned with the Pt(111) LEED spots in such a manner that the atomic rows in the O sublattices are parallel to the atomic rows of the Pt(111) substrate [97].

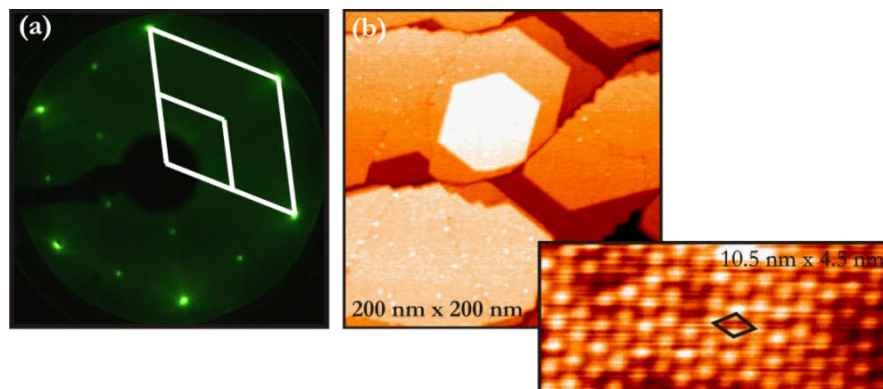


Fig. 2.25 (a) LEED pattern of an $\text{Fe}_3\text{O}_4(111)$ film grown on Pt(111), a $p(2 \times 2)$ unit cell is indicated; (b) STM images of $\text{Fe}_3\text{O}_4(111)/\text{Pt}(111)$ (provided by M. Lewandowski).

The termination of the close-packed surfaces of $\text{Fe}_3\text{O}_4(111)$ has been addressed in the literature [48, 97]. Fig. 2.26 displays a TPD spectrum of 5 Langmuirs (L) ($1 \text{ L} = 10^{-6} \text{ Torr} \cdot \text{s}$) CO adsorbed on $\text{Fe}_3\text{O}_4(111)$ surface at 90 K. The spectrum is acquired by monitoring the 28 amu signal while applying a constant heating rate of 3 K s^{-1} . Three desorption peaks appear at 110 K, 180 K, and 230 K, denoted as α , β , and γ , respectively. Based on the combined TPD, IRAS (Infrared Reflection Absorption Spectroscopy), and HREELS (High Resolution Electron Energy Loss Spectroscopy) studies by Lemire et al.[48], three adsorption states show CO stretching frequencies at $2115\text{-}2140 \text{ cm}^{-1}$ (α state), 2080 cm^{-1} (β state), and 2207 cm^{-1} (γ state). The α state was assigned to a weakly bond (physisorbed) species. The β state was interpreted to be CO adsorbed on regular sites on terraces, which are terminated by Fe^{2+} , and the γ state as CO strongly bond to Fe^{3+} cations present on step edges. One possible surface structure was suggested to be terminated by an outmost $1/4 \text{ ML}$ of octahedral Fe^{2+} cations situated above a $1/4 \text{ ML}$ of tetrahedral Fe^{3+} ions. However, this surface structure is still debated in the literature [48, 97], and it seems to critically depend on the preparation procedures, such as oxidation temperature, cooling rate, etc.

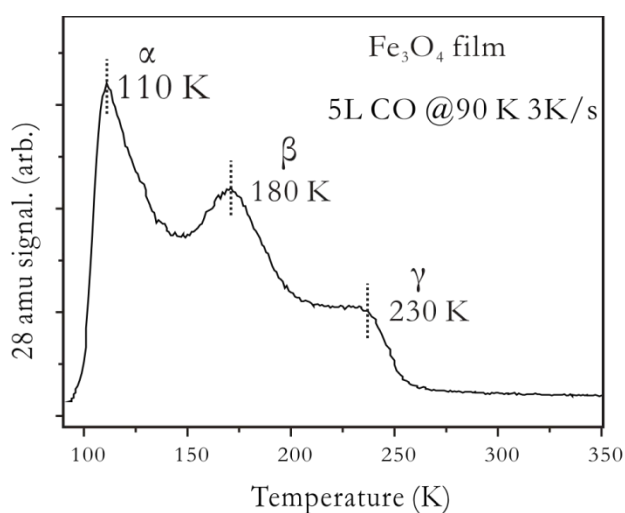


Fig. 2.26 Typical TPD spectrum of CO adsorbed at 90 K on an $\text{Fe}_3\text{O}_4(111)$ film. Three desorption states are denoted as α , β , and γ . The heating rate is 3 K s^{-1} .

Iron oxides are common and widely used compounds for catalyzing many reactions involving selective oxidations, dehydrogenations, CO oxidation, water-gas shift reaction, etc [137]. Well-ordered iron oxide thin films have been employed for studying water adsorption (see e.g. [138-140]) and modeling the dehydrogenation of ethylbenzene to

styrene synthesis (see e.g. [97, 141, 142]). They have been found to be suitable model catalysts for the systematic investigation of catalytic reactions at atomic level.

3

CO Oxidation on Ultrathin FeO(111)/Pt(111)

In this Chapter, we have studied CO oxidation over FeO(111) films grown on Pt(111). The results showed an unexpected promoting effect of an ultrathin FeO film in CO oxidation at realistic reaction conditions.

3.1. CO Oxidation under UHV Conditions

Before discussing reactivity of model catalysts at elevated pressures, it is instructive here to summarize the results obtained by TPD and temperature programmed reaction (TPR) for adsorption and co-adsorption of CO and O₂ on Pt(111) and FeO(111) film at UHV conditions.

Numerous studies performed on clean Pt (111) single crystal surfaces in UHV showed that CO adsorbs molecularly and preferentially occupies atop sites [16]. At increasing coverage ($\theta > 0.17$), CO also resides on bridge sites. Several ordered structures as evidenced in LEED experiments at 170 K have been reported [9, 16, 143, 144]. At a coverage $\theta = 0.33$, a fuzzy $(\sqrt{3} \times \sqrt{3})R30^\circ$ structure is formed. Upon coverage increase to $\theta = 0.5$ a sharp $c(4 \times 2)$ (or $(\sqrt{3} \times 2)_{\text{rect}}$) structure is observed. The transition to the higher coverage results in the compression of the $c(4 \times 2)$ unit and the formation of two hexagonal close packed structures, $c(\sqrt{3} \times 5)_{\text{rect}}$ and $c(\sqrt{3} \times 7)_{\text{rect}}$, for $\theta = 0.6$ and $\theta = 0.71$, respectively. When the experiments were performed at room temperature, only first two LEED patterns were observed. It is noteworthy that there is no pressure gap for CO adsorption on Pt(111) as suggested by Carrasco et al. in their polarization modulated

infrared reflection absorption spectroscopy (PM-IRAS) and sum frequency generation (SFG) measurements [145].

Oxygen adsorption on Pt(111) surface has also been studied. O_2 adsorbs molecularly at ~ 100 K with a saturation coverage of $\theta = 0.44$, providing a $(3/2 \times 3/2)R15^\circ$ diffraction pattern [146]. Upon annealing the sample to 300 K, the molecularly adsorbed oxygen partially desorbs at 150 K and partially dissociates, forming atomic oxygen which resides on threefold hollow sites with the saturation coverage of $\theta = 0.25$. An ordered $p(2 \times 2)$ diffraction pattern is observed.

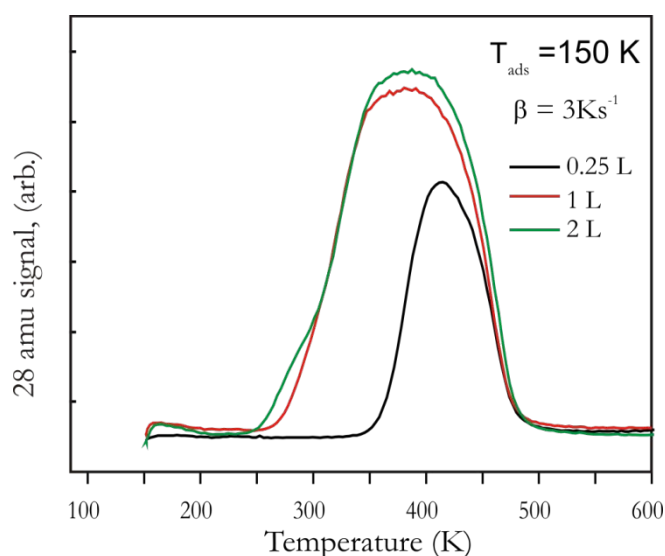


Fig. 3.1 TPD spectra of CO adsorbed at 150 K on Pt(111) surface as a function of CO exposure. The heating rate is $3 Ks^{-1}$.

Fig. 3.1 displays TPD spectra acquired after exposing Pt(111) to increasing amount of CO at 150 K. CO adsorbs molecularly on the surface. A desorption maximum appears at 414 K for the lowest exposure, which shifts to 385 K with increasing coverage. At coverage of ~ 2 L, full saturation of CO adsorption is reached on Pt(111) surface. The $c(4 \times 2)$ diffraction pattern is obtained at RT with saturation coverage as shown in Fig. 3.2a. The shift of the peak maximum to low temperature with increasing coverage can be explained in terms of long-rang repulsive interactions between the adsorbed species, which results in the continuous decrease of the adsorption energy with coverage [9]. The activation energy of CO desorption on Pt(111) at different coverages is estimated by applying Redhead's formula as provided in Chapter 2. If the pre-exponential factor ν is assumed to be $10^{13} sec^{-1}$,

the value of E_d extrapolated to zero coverage is around 120 KJ/mol, which is in line with the results reported in the literature [9, 147, 148].

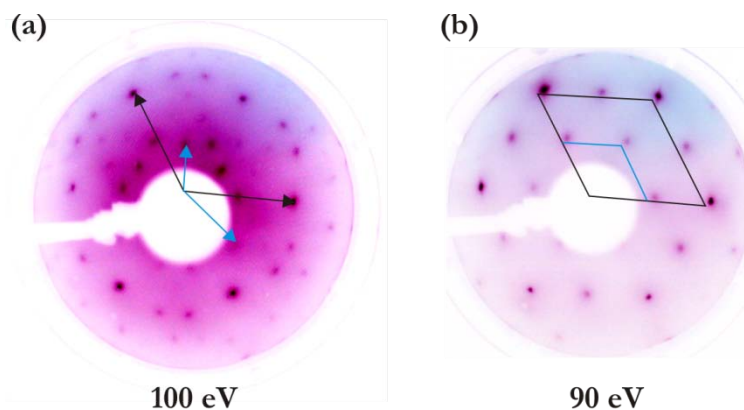


Fig. 3.2 LEED pattern of Pt(111) by exposure to CO with saturation coverage in UHV at RT (left) and 20 mbar of O_2 at RT (right). The unit cell of Pt(111) substrates and overlayers are shown in black and blue, respectively.

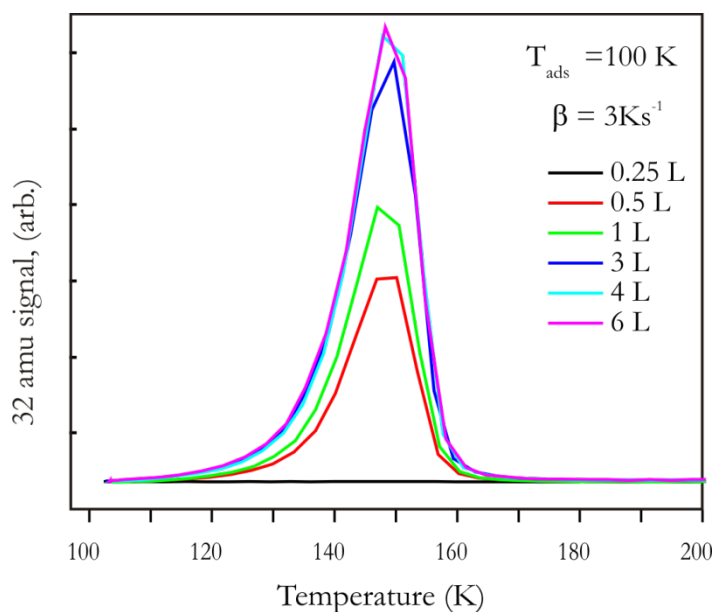


Fig. 3.3 TPD spectra of O_2 adsorbed at 100 K on Pt(111) surface as a function of O_2 exposure. The heating rate is 3 Ks^{-1} .

A series of TPD spectra of O_2 adsorbed on Pt(111) surface at 100 K were measured as a function of O_2 coverage (see Fig. 3.3). O_2 desorbs molecularly with a constant peak position at 148 K with increasing coverage, which saturates at coverage of 3 L. A second broad peak with much less intensity temperature above 600 K is reported in the literature [146, 149], which is ascribed to the recombinative desorption. In our TPD measurements under UHV conditions this feature is not observed, most probably due to the reaction of

the atomic oxygen with the residual CO gas in the chamber upon heating (“clean-off” reaction). However, exposing Pt(111) surface to 20 mbar O₂ at 300 K results in the observation of p(2× 2) diffraction pattern, and the 32 amu desorption feature at ~680 K (see Fig. 3.2b and Fig. 3.4).

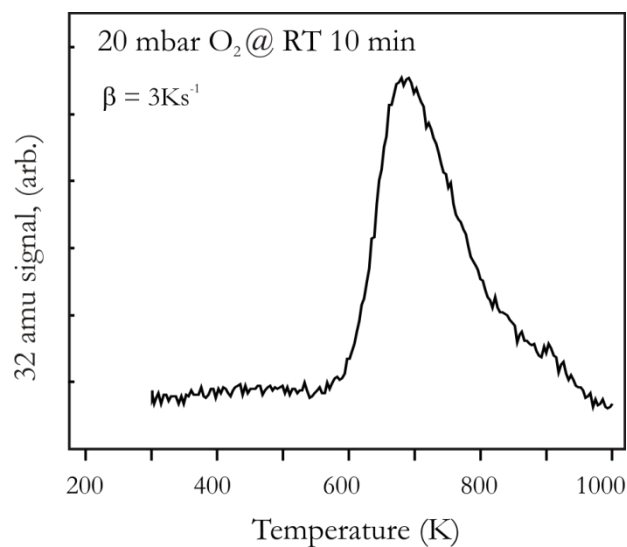


Fig. 3.4 Thermal desorption spectra of Pt(111) surface by exposure to 20 mbar O₂ at RT for 10 min. 32 amu (O₂) signal is shown. The heating rate is 3 Ks⁻¹.

The clean Pt(111) surface exposed to saturating amounts of O₂ (typically, 4 L) and subsequently CO at 100 K showed a broad CO₂ desorption signal centered at 315 K as displayed in Fig. 3.5a. In the opposite sequence or exposing the sample to the mixtures of CO and O₂ at 100 K, no CO₂ was observed in the TPR spectra as shown in Fig. 3.5 b-c. These results are consistent with the well-established CO poisoning effect on oxygen dissociation.

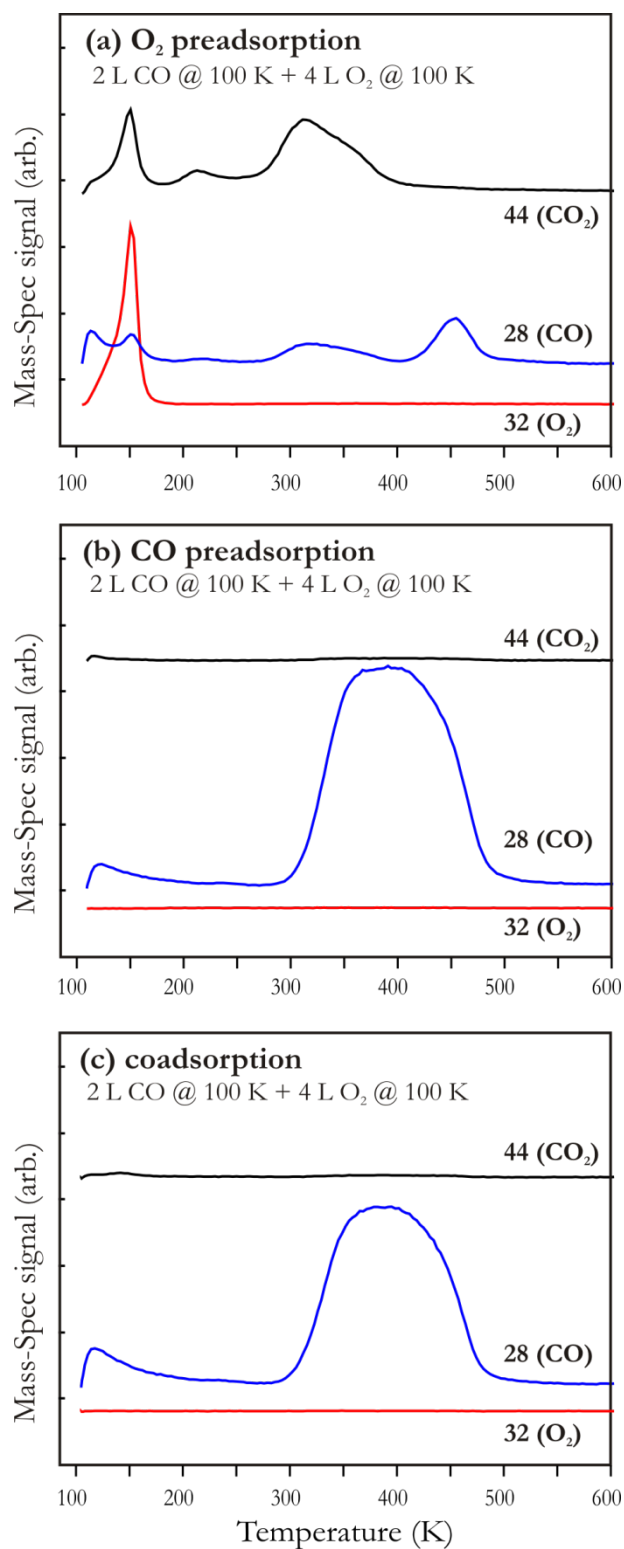


Fig. 3.5 Temperature desorption spectra of CO and O_2 coadsorbed on Pt(111). The 28 (CO), 32 (O_2) and 44 (CO_2) amu signals are shown. (a) CO adsorption on O_2 precovered Pt (111); (b) O_2 adsorption on CO precovered Pt(111); (c) CO and O_2 simultaneous adsorption. The heating rate is 3 K s^{-1} .

On the FeO(111)/Pt(111) surfaces, the individual TPD spectra of CO and O₂ inversely scale with the FeO coverage, with no difference in the temperature profiles as compared to the clean Pt(111), thus indicating no specific adsorption at the rim of FeO(111) islands formed at sub-monolayer coverage. As expected, the FeO(111) films fully covering Pt(111) do not show CO₂ formation in TPR spectra, since neither CO nor O₂ adsorbs on the O-terminated FeO(111) surface at the temperatures used. Note also that long exposures of the FeO films to 10⁻⁶ mbar CO at 500 K did not reveal any signature of oxide reduction. The results basically confirm the previous conclusions [97] about good thermal stability and chemical inertness of the FeO(111) films. However, the situation changes dramatically in the mbar-pressure range.

3.2. CO Oxidation at Elevated Pressures

3.2.1. Stoichiometric CO:O₂ Ratio (2:1)

CO oxidation on FeO(111) films in the stoichiometric mixture of CO and O₂ balanced by He to atmospheric pressure at 450 K was investigated. The same experiment on Pt(111) and the well-ordered, nm-thick Fe₃O₄(111) films grown on Pt(111) is performed for comparison. The clean Pt(111) surface showed almost no activity under the same conditions (see Fig. 3.6), that is consistent with the above TPR results on CO self-poisoning. Surprisingly, FeO covered surface oxidized CO with a much higher activity than clean Pt. Quite the contrary, one would have expected that the FeO film further suppresses the reaction on Pt, since the TPR studies in the previous section revealed no CO₂ formation on the FeO(111) film under UHV conditions. Indeed, the reactivity of the FeO films strongly depends on the pressure while keeping the same CO:O₂ ratio as displayed in Fig. 3.6. The reaction proceeds much slower when the pressure is reduced from 60 to 15 mbar, and then to 6 mbar. On the other hand, the well-ordered, nm-thick Fe₃O₄(111) films grown on Pt(111) also exhibited much lower activity than the FeO film, indicating that the enhanced activity observed in these experiments must be intimately connected to the ultrathin FeO(111) film on Pt(111).

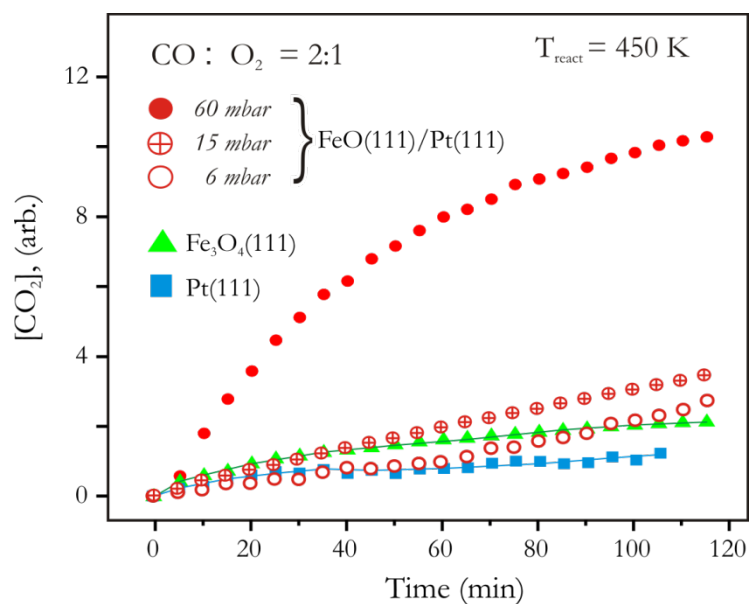


Fig. 3.6 Kinetics of CO₂ production over FeO/Pt(111) at stoichiometric CO:O₂ (2:1) ratios at indicated total pressures at 450 K. The results for Pt(111) and nm-thick Fe₃O₄(111)/Pt(111) film in 40 mbar CO + 20 mbar O₂ at 450 K are shown for comparison. Time zero corresponds to the start of the sample heating (1 Ks⁻¹) from 300 K.

Fig. 3.7 shows CO₂ evolution upon slow heating of FeO(111) films in the mixture of 40 mbar CO and 20 mbar O₂. Carbon dioxide is clearly observed at temperatures above 430 K. The reaction rate apparently increases at increasing temperature as shown in Fig. 3.8 presenting the kinetics of the CO₂ formation at different temperatures. At all temperatures studied, the oxidation rate decreases in time.

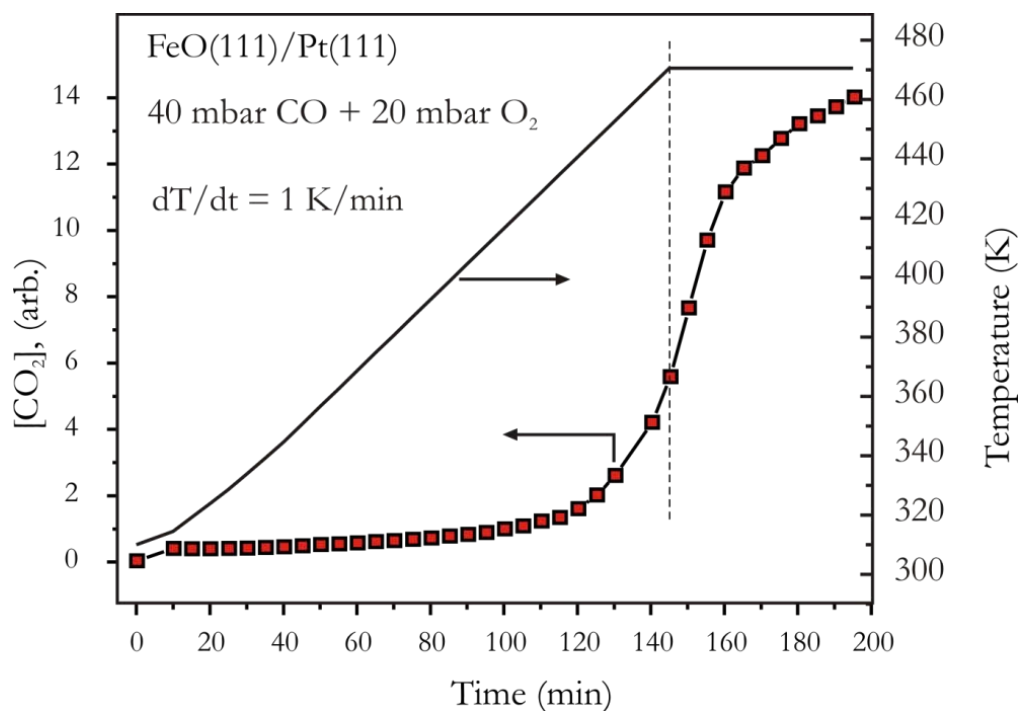


Fig. 3.7 Temperature-programmed reaction profile of CO₂ production over FeO(111)/Pt(111) on slow heating (1 Kmin⁻¹) in 40 mbar CO + 20 mbar O₂ balanced by He.

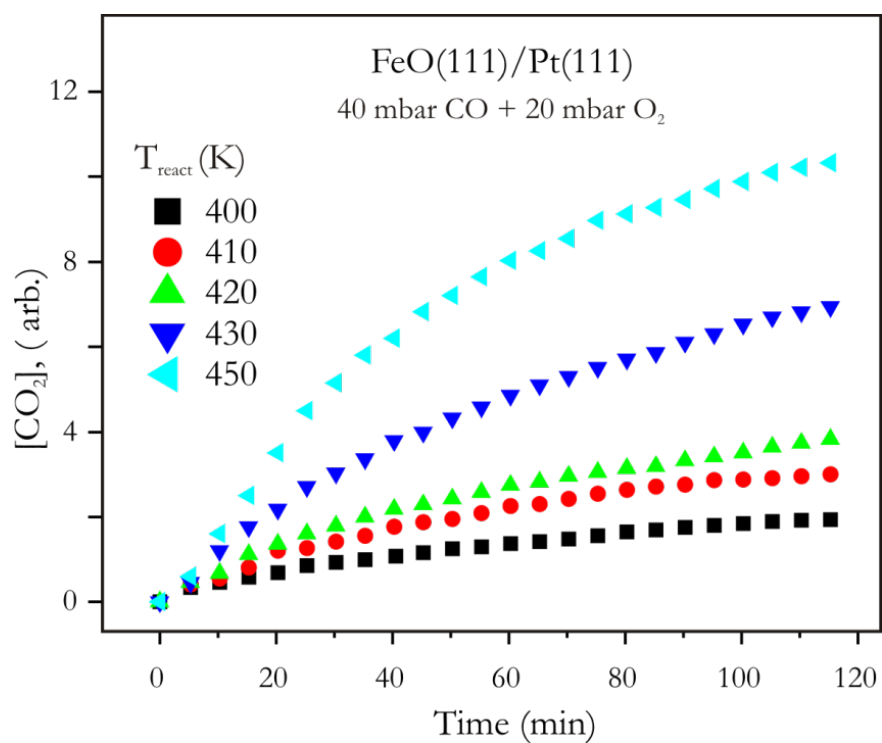


Fig. 3.8 kinetics of CO₂ production over FeO(111)/Pt(111) in 40 mbar CO + 20 mbar O₂ balanced by He at indicated temperatures.

Fig. 3.9 shows LEED patterns of the FeO(111)/Pt(111) surface after reaction at 400 and 450 K in 60 mbar of CO + O₂ as indicated. The surface after reaction at 400 K resembles the diffraction pattern of the origin FeO(111) surface, indicating that the surface preserves long-range ordering. The conclusion holds true also for the samples treated in 6 mbar at 450 K. On the contrary, the sample reacted at 450 K showed the sharp diffraction spots of Pt(111) with additional weak spots, which are practically identical to those observed on clean Pt(111) by exposure to CO and assigned to a Pt(111)-c(4x2)CO structure [9, 16, 143, 144]. At intermediate temperatures (~ 430 K), a superposition of the FeO(111)/Pt(111) and CO/Pt(111) structures was observed.

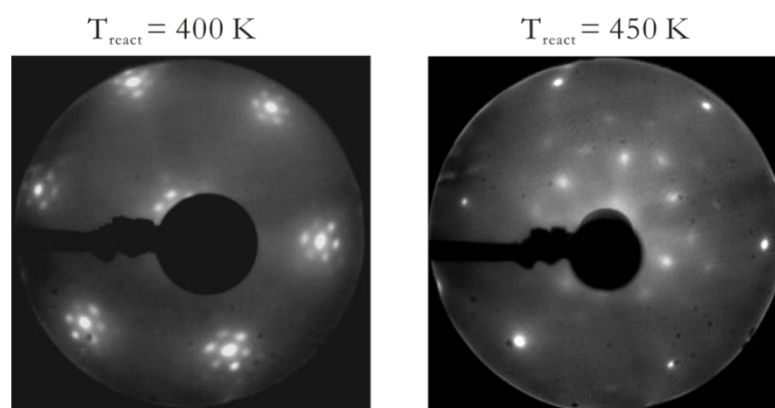


Fig. 3.9 LEED patterns ($E = 60$ eV) of the FeO(111) film after reaction at 400 K (left) and 450 K (right) in 40 mbar CO + 20 mbar O₂ in He.

The AES study of the spent catalysts revealed only small amounts of carbon beyond the elements, which belong to the original surfaces, as shown in Fig. 3.10. (In particular, no nickel via Ni carbonyls which may contaminate CO in high-pressure containers has been detected). Carbon (but no oxygen) has been found on the post-reacted Pt(111) surface most likely due to CO dissociation on the Pt low coordination sites (see Chapter 5). Therefore, it seems plausible that carbon on the FeO/Pt surface appears in course of surface reconstructions whereby CO dissociates on the open Pt(111) areas. In addition, using the Auger O:Fe signal ratio in the pristine FeO films as a reference, the iron oxide phase in the post-reacted catalysts exhibits a FeO_x ($x \sim 1.25$) stoichiometry, on average. In line with LEED data, Auger spectra revealed no significant differences in the surface composition after catalytic tests at lower temperatures and/or lower pressures. The threshold temperature observed for the structural changes (~ 430 K) basically coincides with the “ignition” temperature in the reaction profile shown in Fig. 3.7.

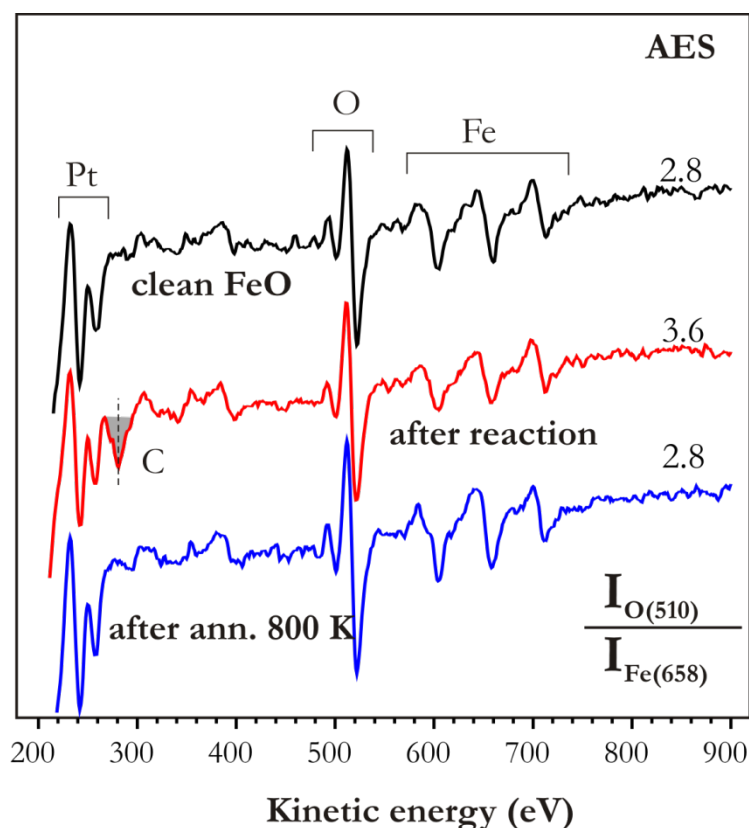


Fig. 3.10 AES spectra of the clean FeO(111) film (top), after the reaction in 40 mbar CO + 20 mbar O₂ at 450 K (middle) and subsequent annealing to 800 K for 2 min (bottom). The corresponding peak ratios for O(510 eV) and Fe(658 eV) are indicated.

The LEED/AES study of the post-reacted samples show that the CO oxidation activity correlates well with the structural transformations of the FeO/Pt surface, which occur only in the pressure range above ~10 mbar and temperatures above 430 K, whereby the surface starts to expose Pt(111). In principle, two different structures could be proposed at this point. First, the FeO film dewets under the reaction conditions and hence opens a Pt(111) substrate. Another scenario stems from the fact that the FeO(111) film is only of monolayer thickness that allows metal atoms to penetrate through the film, as previously shown for Pd deposited onto these films on heating in UHV [55]. In this case, one may envision that the Pt atoms having much high affinity for CO and O₂ than FeO will segregate on top of the FeO film at high temperature and form a single Pt(111) layer on top of FeO/Pt(111). To determine the surface morphology of the model catalysts we employed STM. The experiments were performed in another UHV chamber connected via gate valve to a gold-plated “high-pressure” cell used as a batch reactor.

We have first inspected the post-reacted Pt(111) crystal, which is found to essentially preserve the surface topography as shown in Fig. 3.11a. Only few small, irregularly shaped particles, presumably of carbon (as judged by AES), and primarily located at the terrace steps were observed. Besides, this provides further evidence that the surfaces were essentially not contaminated during reactions at elevated pressures.

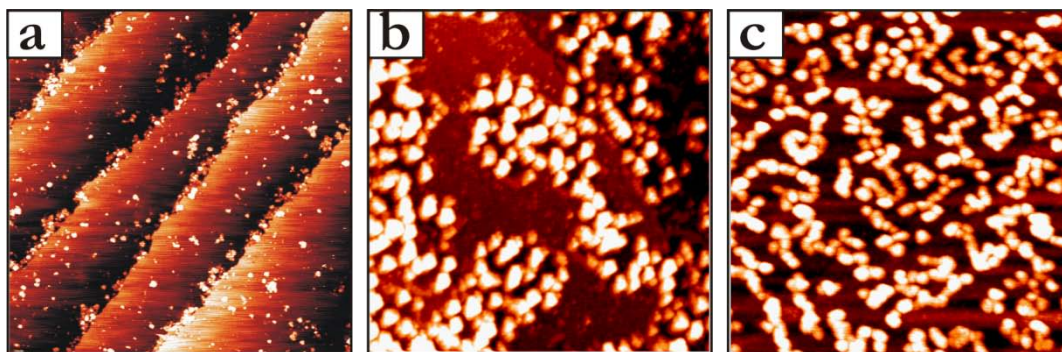


Fig. 3.11 Room temperature STM images (provided by Z.-H. Qin) (size $200\text{ nm} \times 200\text{ nm}$) of Pt(111) (a), FeO(111) film after 10 min (b), and FeO(111) film after 120 min (c) in 40 mbar + 20 mbar O_2 in He at 450 K.

The STM image of a FeO(111)/Pt(111) film with atomically flat, wide terraces exhibiting Moiré superstructure with a periodicity $\sim 2.6\text{ nm}$ is shown in Fig. 2.24. After 10 minutes exposure to the 40 mbar CO + 20 mbar O_2 mixture at 450 K, small particles emerge on the surface (see Fig. 3.11b), whereas the rest of the surface shows FeO-like superstructure. The large-scale STM images show that the reconstruction proceeds homogeneously on the whole film. After 120 min the surface is covered by nanoparticles as shown in Fig. 3.11c. The particles exhibit a narrow size distribution of $8 \pm 1\text{ nm}$ in diameter and $1.8 \pm 0.1\text{ nm}$ in height. These nanoparticles are three-dimensional in nature, exhibit a rough morphology and therefore can hardly be assigned to the sandwich-like structure proposed above. Therefore, the particles are assigned to iron oxide particles formed on Pt(111) upon dewetting of the FeO film at elevated pressure and temperature. These particles are supported on a Pt(111) substrate which is in turn covered by CO forming the $c(4 \times 2)$ superstructure as observed by LEED (see Fig. 3.9).

Interestingly, subsequent UHV annealing at temperatures above 800 K essentially restores the LEED pattern (see Fig. 3.12) and the O:Fe ratio of the original FeO film and also removes carbon from the surface (see bottom spectrum in Fig. 3.10). TPD and STM study also showed that stepwise heating to 600 K, 700 K and 800 K in UHV leads to

gradual wetting of the Pt (111) substrate, ultimately forming the FeO(111) film, which again shows chemical inertness towards CO as shown in Fig. 3.13 and Fig. 3.14. Thus, the combined LEED, AES and STM results clearly show that the thin FeO film wetting/dewetting of Pt(111) is totally *reversible* and only depends on the ambient atmosphere and temperature.

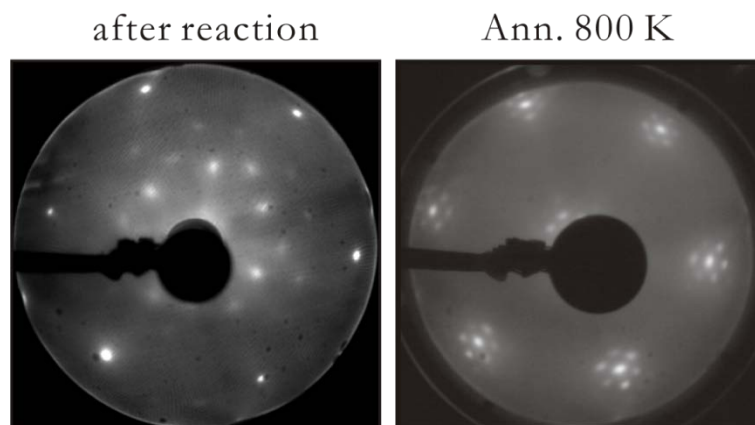


Fig. 3.12 LEED patterns ($E = 60$ eV) of the FeO(111) film after reaction at 450 K(left) in 40 mbar CO + 20 mbar O₂ in He and subsequently annealed in vacuum at 800 K (right).

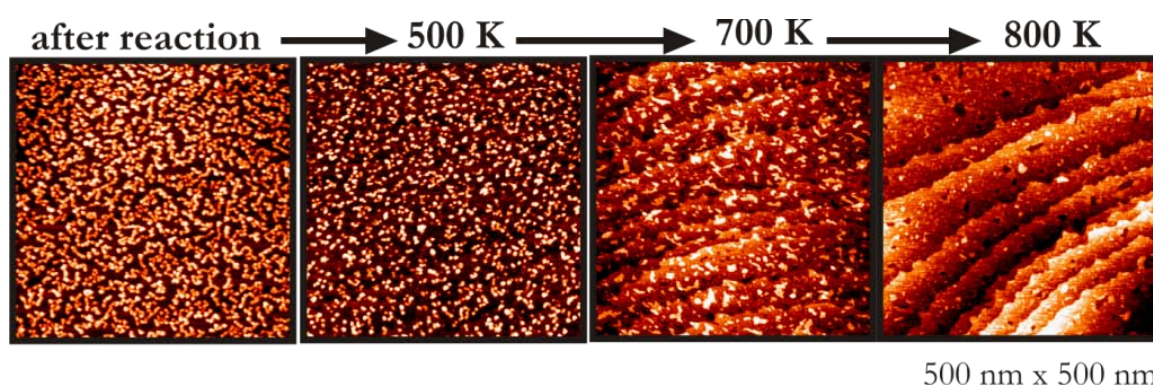


Fig. 3.13 STM images (provided by Z.-H. Qin) (size $500\text{ nm} \times 500\text{ nm}$) of the dewetted FeO(111) film and step-wise UHV annealing at 500, 700 and 800 K.

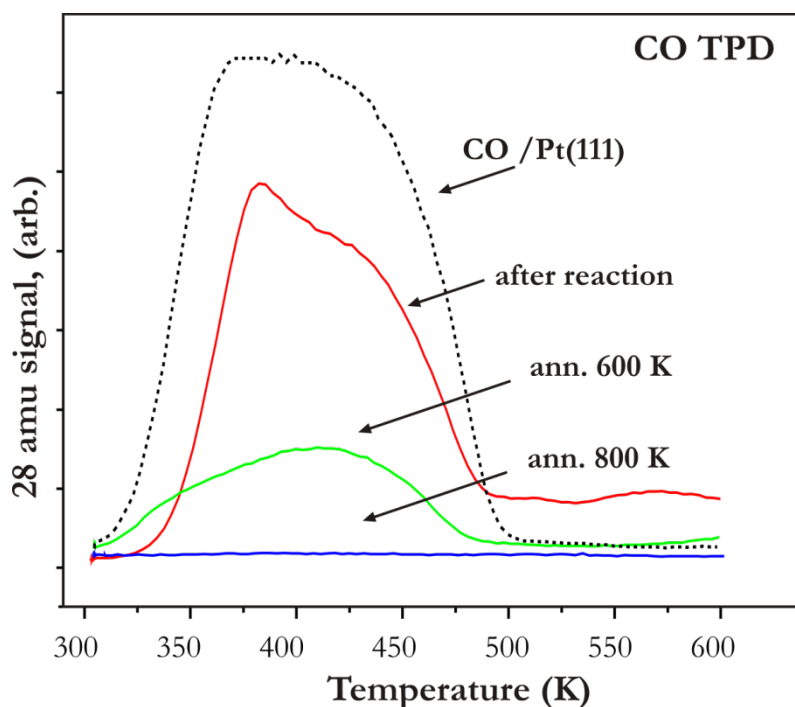


Fig. 3.14 TPD spectra of CO adsorbed at 300 K on the clean Pt(111) (dotted line) and FeO(111)/Pt(111) after reaction (red line) and after step-wise UHV annealing at 600 K (green line) and 800 K (blue line).

In order to obtain in situ information on surface restructuring we employed PM-IRAS that allowed monitoring surface species simultaneously with the gas-phase composition. Fig. 3.15a shows a series of spectra in the CO stretching region obtained from the FeO(111)/Pt(111) surface at 450 K in a reaction mixture of 40 mbar CO and 20 mbar O₂ (balanced by He). The spectrum for a Pt(111) crystal under the same conditions for 120 min is also shown for comparison.

The absorption band at $\sim 2095\text{ cm}^{-1}$ that grows with time is characteristic for atop (or terminal) CO species on Pt(111). In addition, a broad band centred at $\sim 1865\text{ cm}^{-1}$ develops, which is typical for CO occupying bridge position, i.e., consistent with the formation of c(4x2)-CO overlayer on Pt(111) observed by LEED. The integral intensity of this band apparently saturates after ~ 60 min of the reaction as shown in Fig. 3.15, finally exposing approximately 70% of Pt(111). Therefore, the PM-IRAS results unambiguously show that an FeO film dewets a Pt substrate under the reaction conditions, thus exposing a Pt(111) substrate. Interestingly, the major peak at 2095 cm^{-1} revealed a low frequency shoulder, which remained after sample cooling and pumping the reactor out. Therefore, this feature can hardly be assigned to CO adsorbed on Lewis (Fe²⁺) sites on iron oxide

particles as CO desorbs from iron oxide surfaces below room temperature [150]. On the other hand, this feature is missing in the spectra for Pt(111) under the same conditions. Therefore, its presence on the dewetted surface could be linked to the oxide/metal interface formed upon dewetting.

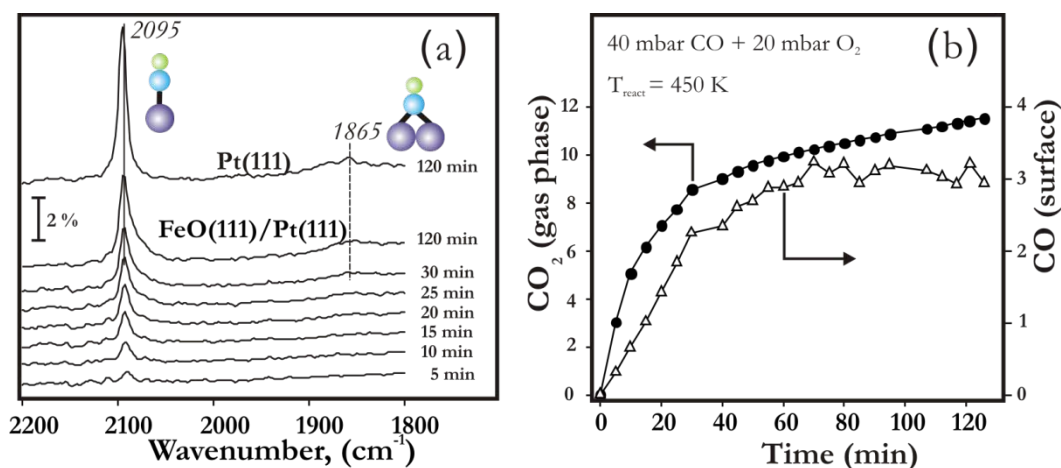


Fig. 3.15 (a) Time-resolved PM-IRAS spectra of the CO stretching region obtained from the FeO(111)/Pt(111) surface at 450 K in a mixture of 40 mbar CO + 20 mbar O₂ in He to 1 bar. The spectrum for the Pt(111) surface after 120 min at the same conditions is shown for comparison. (b) Kinetics of CO₂ formation in the gas phase and of CO adsorbed on FeO(111)/Pt(111) obtained by integration of the respective PM-IRAS signals. (provided by E. Carrasco)

Fig. 3.15b shows the time evolution of integral amounts of CO adsorbed on the surface and of CO₂ produced in the reaction as obtained by the respective surface and gas-phase IR signals. The kinetics of the CO₂ production resembles that of the GC experiments presented in Fig. 3.8, both showing that the CO oxidation rate (the slope of the CO₂ production curve) decreases with time. It is clearly seen that the highest rate is observed at the beginning of the reaction where the surface is essentially non-dewetted (see more in the next section). With increasing degree of dewetting the reaction rate slows down and is practically constant as the maximum dewetting is obtained. At this stage, the CO₂ formation rate is almost equal to that observed for a Pt(111) single crystal.

Further information on the structure of the post-reacted FeO/Pt surfaces was obtained by TPD. Only CO and CO₂ were found as desorbing species upon heating of the spent catalysts in UHV. After reaction at low temperatures, a broad and rather featureless CO desorption signal at 350 - 450 K is observed (see Fig. 3.16). (Note, that the pristine FeO films do not adsorb CO even at 90 K). With increasing the reaction temperature, a

peak at ~ 390 K develops which superimposes with the signal at 320 - 500 K gaining intensity. Except the prominent feature at 380-390 K, the TPD spectra are similar to that observed after CO adsorption on clean Pt(111) shown in the same graph for comparison. The desorption traces of CO and CO₂ at $T > 500$ K, which are missing in the spectra for Pt(111), may be attributed to the reaction of carbonaceous species with surface oxygen (e.g., see [151]). This oxygen is apparently coming from the iron oxide particles since the carbon peak in AES spectra disappears upon heating to 800 K with simultaneous restoration of the Auger O:Fe ratio (see bottom spectrum in Fig. 3.10).

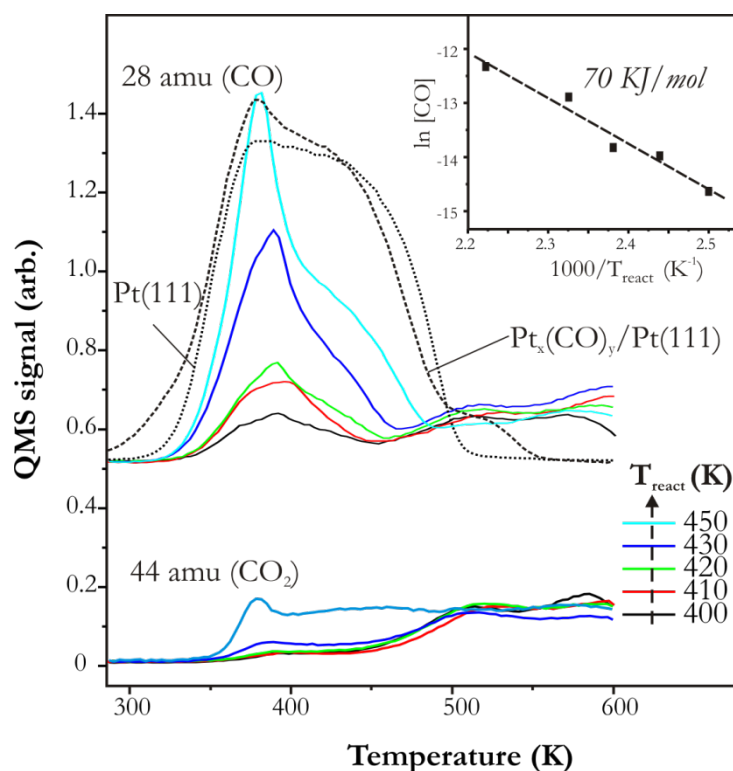


Fig. 3.16 CO (28 amu) and CO₂ (44 amu) signals in TPD spectra of a FeO(111)/Pt(111) film reacted in 40 mbar CO + 20 mbar O₂ for 120 min at indicated temperatures. The samples were cooled to 300 K and evacuated to 10⁻⁵ mbar before exposing to UHV. The inset shows the Arrhenius plot for the integral CO desorption signal as a function of reaction temperature. The spectrum for clean Pt(111) after reaction at 450 K is shown as dotted line for comparison. TPD spectrum of Pt_x(CO)_y formed on Pt(111) by Pt deposition in 10⁻⁶ mbar of CO at 100 K (dashed line) is shown to highlight a desorption feature at ~ 380 K.

Regarding the desorption peak at ~ 380 K, it cannot be assigned to CO adsorbed on iron oxide particles [150]. Note that this peak was only observed on strongly dewetted surfaces (e.g., after reaction in 60 mbar at 450 K) and never under O-rich reaction conditions (see below). Also, the peak does not show up in the next CO TPD runs, i.e.,

after the first heating to 600 K. On the other hand, narrow CO desorption signals are typical for decomposition of metal carbonyls [152, 153]. Indeed, $\text{Pt}_x(\text{CO})_y$ species prepared on Pt(111) by PVD of Pt in 10^{-6} mbar of CO at 100 K revealed a similar TPD peak at ~ 380 K superimposed with the signal from CO/Pt(111) as shown in Fig. 3.16. Therefore, we may assign this desorption feature, observed on the spent catalysts, to Pt carbonyl-like species formed upon dewetting of the oxide film. Its absence on the post-reacted Pt(111) sample indicates that these species are most likely stabilized by the iron oxide particles. This conclusion is also consistent with the observation of a low frequency shoulder on the 2095 cm^{-1} band on FeO/Pt and not on Pt(111) surface in the PM-IRAS experiments (see Fig. 3.15a).

In addition to PM-IRAS, we used the TPD results for estimating the degree of dewetting (determined here as a percentage of the Pt(111) substrate that opens during a reaction) by integrating the CO TPD signal between 300 and 500 K. Using the TPD spectrum for CO/Pt(111) as a reference, we found that approximately 70 % of the surface expose the Pt(111) after reaction at 450 K for 2 h. This value nicely agrees with that obtained by PM-IRAS. It has turned out that the integral CO intensity vs reaction temperature relationship fits well the Arrhenius plot as shown in the inset in Fig. 3.16, from which the activation energy ~ 70 kJ/mol is calculated. The analysis with a proper subtraction of the feature at ~ 380 K in the TPD spectra results in a bit smaller value, ~ 65 kJ/mol. Therefore, 65 - 70 kJ/mol may be considered in the first approximation as the activation energy for the FeO film dewetting; however, this value will depend on pressure and CO:O₂ ratio.

It should be mentioned that according to the TPD studies, no dewetting is observed after individual exposures of FeO films to 40 mbar CO or 20 mbar O₂ at 450 K. In both cases, the LEED patterns revealed a Moiré superstructure (see more in chapter 4). Therefore, the results show that the FeO/Pt surface undergoes *reaction-induced* reconstruction at increasing partial pressure to 60 mbar such that it exposes a significant fraction of Pt(111) in the most active catalysts.

3.2.2. The Effect of CO and O₂ Partial Pressures

It is well documented in the literature that the CO oxidation rate on Pt catalysts strongly depends on CO:O₂ partial pressures ([154, 155] and references therein). Therefore,

one may raise the question about whether the promoting effect of the ultrathin FeO films exists in a wide range of CO and O₂ partial pressures. To study possible effects of the gas composition on reactivity of the FeO films, we carried out two sets of experiments in various CO + O₂ mixtures. In the first set, we varied the O₂ pressure while keeping the CO partial pressure at 10 mbar. In the second set, we kept the O₂ partial pressure constant at 20 mbar and varied the CO pressure. In two sets the CO:O₂ ratio was varied between 1:5 and 5:1 which basically covers both O₂-rich and CO-rich regimes. The mixtures were always balanced by He to 1 bar, and the reaction was monitored at 450 K. After reactivity measurements, the surfaces were characterized by LEED, TPD and AES.

Fig. 3.17 shows the kinetics of CO₂ production at different CO and O₂ partial pressures. Under CO-lean conditions the reaction rate is almost constant in time and increases while approaching 100 % conversion of CO. In contrast, the reaction slows down in the CO-rich conditions. Note, that the reaction rate was not much affected by CO₂ accumulation in the circulating gas mixture. Pumping out the reactor and refilling the line with a fresh CO + O₂ mixture had basically no effect on the subsequent activity, thus indicating that CO₂ is not involved in the deactivation process. For further analysis we present the rates measured in the first minutes of reaction (i.e., extrapolated to zero conversion on yet non-deactivated catalysts), if not specified.

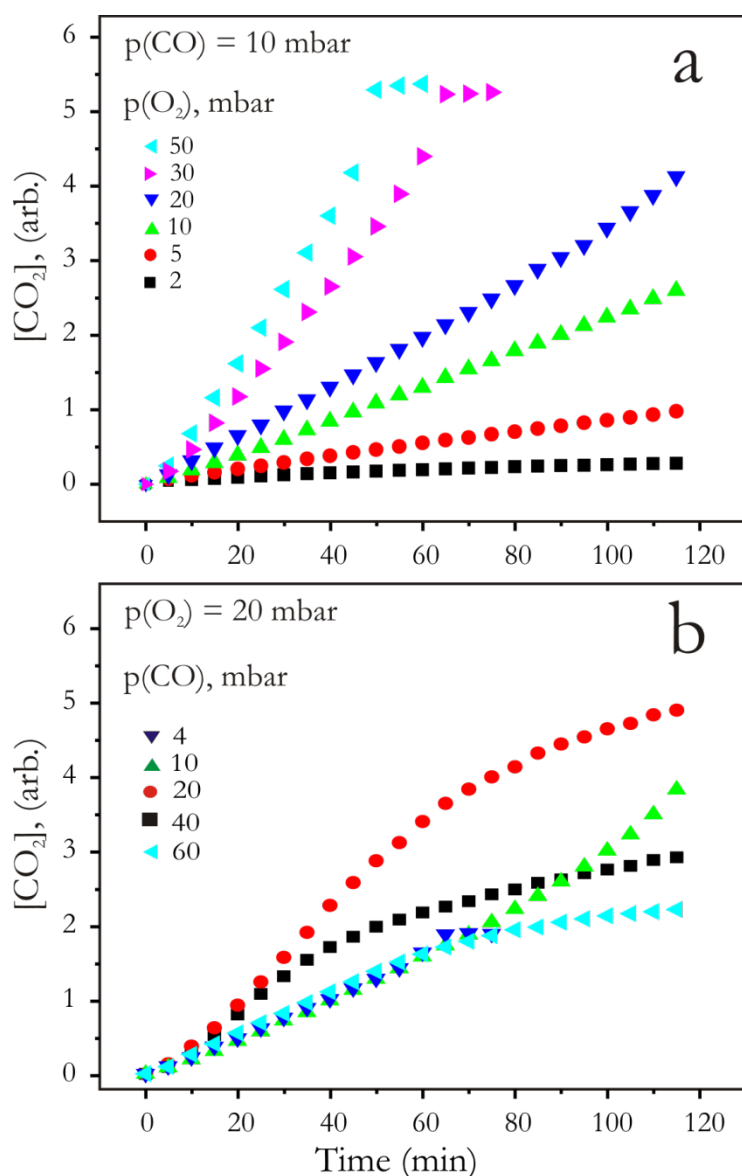


Fig. 3.17 Kinetics of CO₂ production at 450 K at different CO and O₂ partial pressures as indicated. Full conversion can be reached at low CO:O₂ ratios. Note the reaction rate slows down in CO-rich conditions. (CO:O₂ > 1).

Fig. 3.18a depicts the reaction rate as a function of oxygen pressure. The reaction kinetics exhibits first order ($n = 1.1 \pm 0.1$) for O₂. This may straightforwardly explain the results of Fig. 3.6 showing much lower CO₂ production upon decreasing the total CO + O₂ (2:1) pressure from 60 down to 6 mbar. The reaction order measured on Pt(111) under the same conditions is close to unity ($n = 0.85 \pm 0.1$) and is consistent with previous studies [156]. The figure shows that the FeO/Pt catalysts exhibit much higher activity than Pt(111) in the whole pressure range studied.

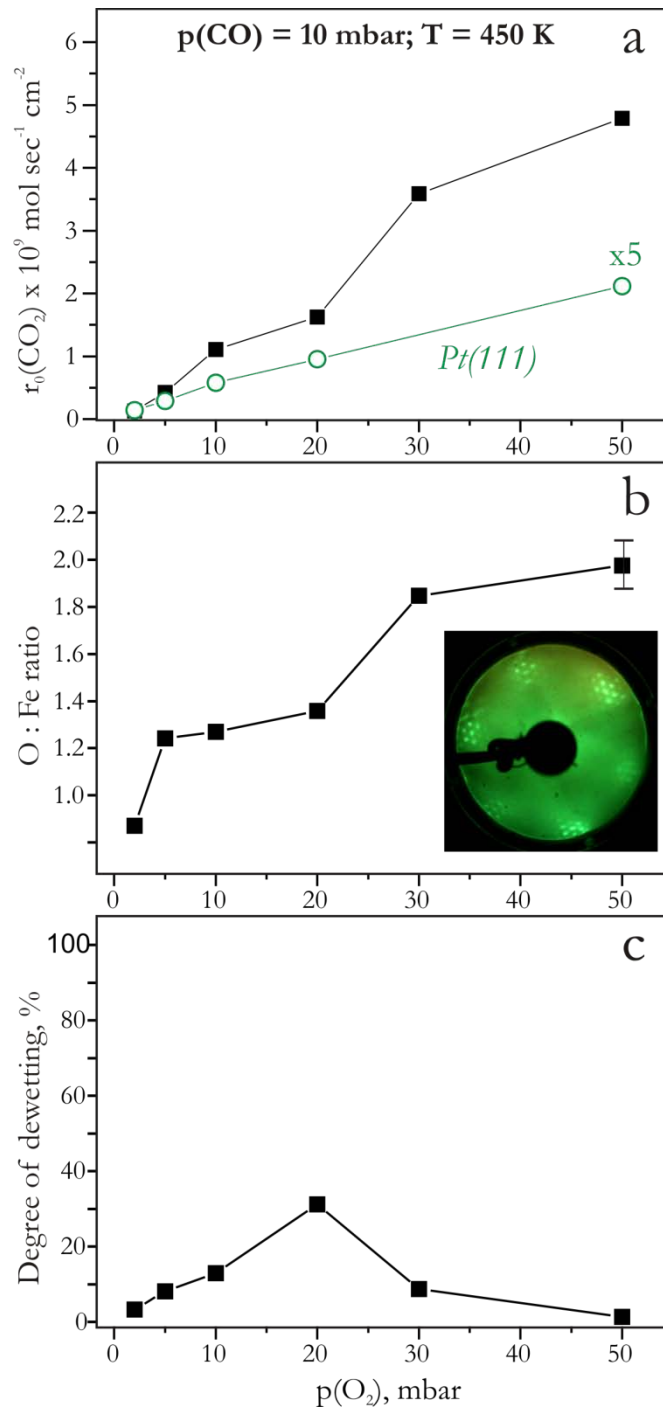


Fig. 3.18 Reaction rate (a), average stoichiometry (b) and degree of dewetting (c) of the spent FeO/Pt catalysts as a function of O_2 pressure in the mixture with 10 mbar of CO, balance by He to 1 bar. The reaction temperature is 450 K.

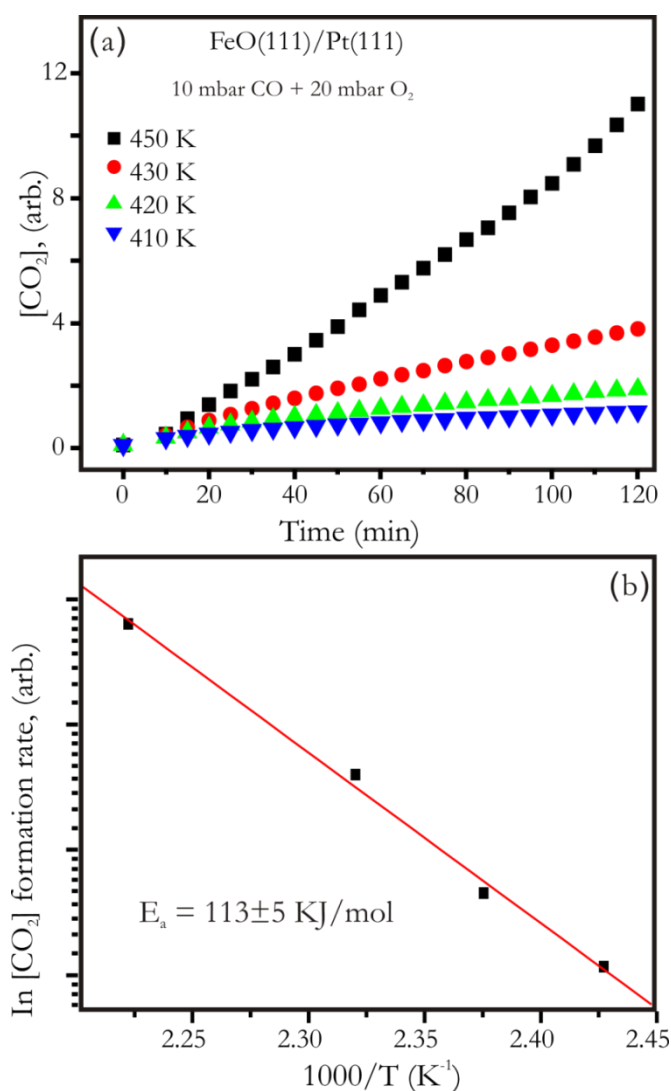


Fig. 3.19 (a) kinetics of CO₂ production over FeO(111)/Pt(111) in 10 mbar CO + 20 mbar O₂ balanced by He at indicated temperatures. (b) Arrhenius plot for the integral CO desorption signal as a function of reaction temperature.

The temperature dependence of the reaction rate measured at 410 – 450 K in the mixture of 10 mbar CO and 20 mbar O₂ leads to an Arrhenius plot with an apparent activation energy of 113 ± 5 kJ/mol as shown in Fig. 3.19. Due to the very low conversion, it was impossible to precisely measure the activation energy on Pt(111) for comparison. Nevertheless, this value is significantly lower than ~ 135 kJ/mol, reported for supported Pt catalysts and Pt single crystal surfaces for conditions where CO is the primary surface species [155, 156], which is in turn very close to the desorption energy of CO from Pt (see section 3.1).

The reaction is accompanied by remarkable structural changes detected by AES. The film becomes enriched with oxygen upon increasing O₂ pressure, and approaches the Fe:O ratio close to 2 (without losing Fe), on average (see Fig. 3.18b). Interestingly, the corresponding LEED patterns (shown in the inset in Fig. 3.18b) are in fact similar to those of the pristine FeO(111)/Pt(111) surface. Therefore, we have tentatively proposed that a FeO film, originally composed of Fe and O close-packed layers stacked as O-Fe/Pt, reconstructs at high O₂ pressures into a O-Fe-O/Pt –like (“sandwich”) structure. Another intriguing finding is that the degree of dewetting (see Fig. 3.18c) basically shows no direct relationship to activity. In fact, in the O₂-rich atmosphere the inverse relation is observed such that the activity is the highest for the least dewetted surface.

In the next step, we review experimental results of the second set of experiments. Fig. 3.20 shows the reaction rate (a), average stoichiometry of the iron oxide film (b), and degree of dewetting (c) as a function of CO partial pressure. Note, that under the same conditions the Pt(111) surface showed zero-order kinetics for CO at 450 K, i.e., in full agreement with previous studies [156]. Fig. 3.20a reveals again, that the FeO films are much more active than Pt(111) in the whole CO pressure range studied. The initial reaction rate vs. CO pressure relationship is not monotonous and has a maximum at CO:O₂ ~ 1. Apparently, at high CO pressures the reaction exhibits negative reaction order, and the catalytic activity decreases with time (see Fig. 3.17b and also Fig. 3.8). The data measured after two hours of reaction are also shown in Fig. 3.20a, for comparison.

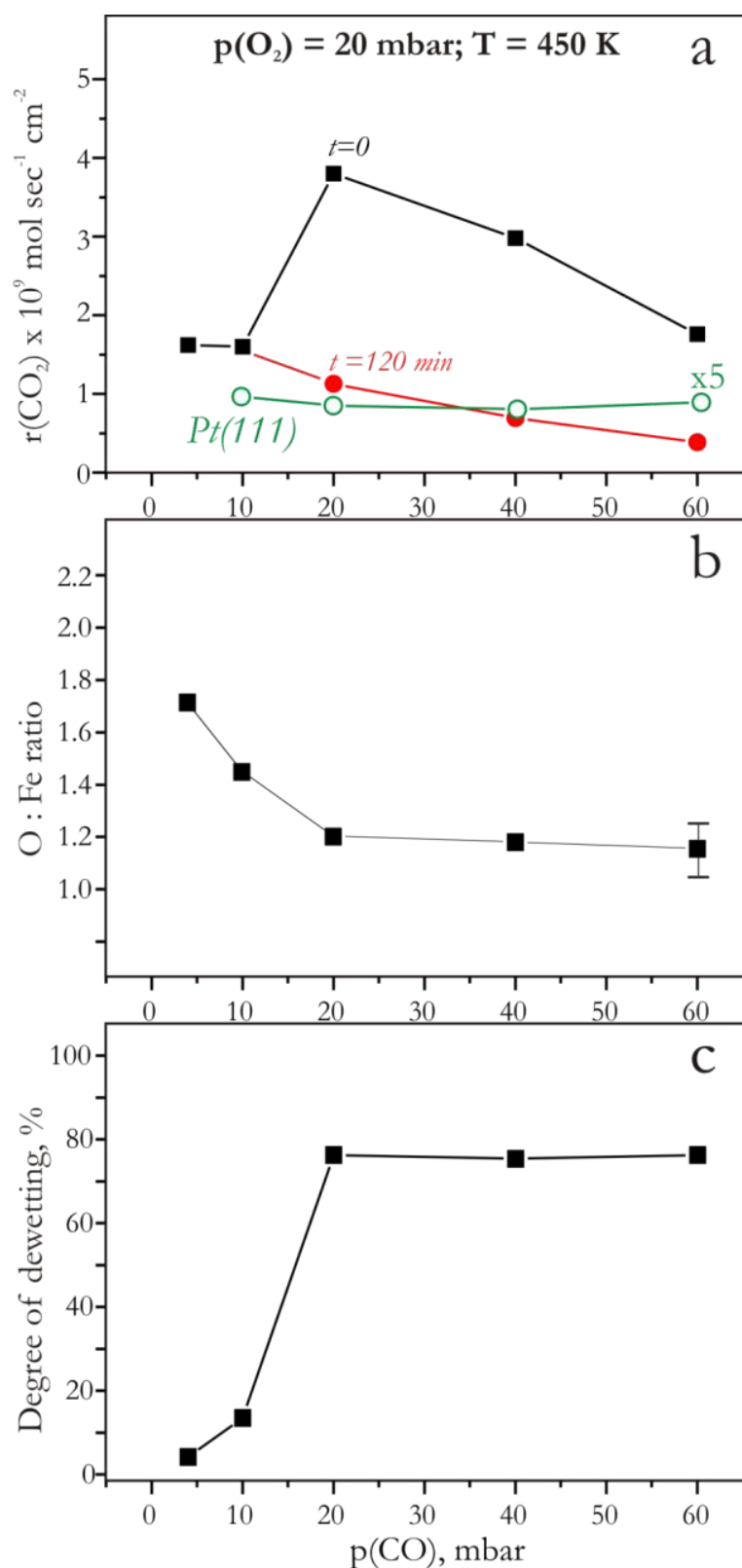


Fig. 3.20 Reaction rate (a), average stoichiometry (b) and degree of dewetting (c) of the spent FeO/Pt catalysts as a function of O_2 pressure in the mixture with 10 mbar of CO, balance by He to 1 bar. The reaction rates measured after 120 min on stream as well as data for clean Pt(111) are also shown. The reaction temperature is 450 K.

Certainly, whenever reactions at elevated pressures are carried out, very careful attention needs to be considered towards impurities in the feedstock, particularly to those having high reaction probability. There are evidences in the literature showing that oxide surfaces may be very sensitive to the traces of water in an ambient, even in the vacuum background [157-159]. In order to see whether water and hydrogen as impurities in the reaction ambient affect the reactivity data presented in Fig. 3.17, we have performed experiments in the TPD-GC setup using the mixture of 10 mbar CO + 50 mbar O₂ with additional 0.5 mbar of water. The results showed no effect of water on reactivity under these conditions. Meanwhile, adding 0.5 mbar of H₂ to a CO + O₂ mixture dramatically increased the reaction rate, by factor of 2. However, in the latter case the reaction most likely proceeds through the different mechanism (to be discussed in Chapter 6).

3.2.3. Proposed Mechanism

The key observations presented in the previous sections can be summarized as follows.

- (1) FeO(111) monolayer films grown on Pt(111) show much higher CO oxidation activity than Pt(111) at 400 - 450 K in a wide range of CO:O₂ ratios (between 1:5 and 5:1).
- (2) The reaction rate at 450 K exhibits first order for O₂ and non-monotonously depends on CO pressure.
- (3) The effect is observed only in the mbar pressure range. The reaction is accompanied by strong structural transformations. In O₂-rich ambient, the films become enriched with oxygen while maintaining the long range ordering. Under CO-rich conditions, the films undergo dewetting that causes the catalyst's deactivation. Dewetting is a reaction induced process and cannot be observed in pure O₂ or CO ambient. The wetting/dewetting process is reversible depending on the ambient conditions.
- (4) The surface of the O-rich film formed at elevated O₂ partial pressures is in fact the most active. The surface transformations resulting in this surface seem to be relatively fast since the reaction rate in the O-rich atmosphere is practically constant from the onset.

Before turning to the proposed mechanism of our system, it is instructive here to briefly review the reaction mechanism of oxidation reactions on oxides. A Mars-van Krevelen scheme [160] is usually considered which invokes a surface redox process where the reactant is oxidized by lattice oxygen and the reduced catalyst is subsequently reoxidized by molecular oxygen. However, the recent analysis by Vannice [161] revealed a number of inconsistencies in the assumptions incorporated into the derivation of the rate expression, even though still the experimental data may be fitted.

Oxidation of CO on iron oxides (Fe_2O_3) has been previously studied both experimentally and theoretically [162-165]. The reaction is typically carried out at temperatures above 500 K in excess of oxygen, although the reaction may occur even in the absence of external oxygen over iron oxide nanoparticles [163]. It was found that the reaction proceeds through dissociative adsorption of O_2 , which is considered to be a non-activated process, and removal of oxygen by a gas-phase CO via an Eley-Rideal type mechanism [161, 163]. The reaction showed zero-order kinetics for O_2 and first order for CO at 520 – 570 K. Microkinetic modeling revealed that the reaction between CO and surface O species is the rate-determining step [165]. The Eley-Rideal mechanism was corroborated theoretically for the (100) surface of Fe_2O_3 , whereas on the oxygen terminated (0001) surface the preference towards the Langmuir-Hinshelwood mechanism (i.e., CO adsorption before reaction with O) was observed [162].

Certainly, in these studies the bulk structure of iron oxide was assumed to remain unchanged during reaction, whereas the monolayer FeO films undergo strong transformations, which should be taken into account in the reaction kinetics. Our results showed first order kinetics for O_2 , i.e., in variance to the above-mentioned iron oxides catalysts showing zero order. Therefore, it may well be that the oxygen pressure dependence reflects the kinetics of structural transformations resulting in the O-rich phase rather than the reaction itself. It seems plausible that the whole reaction starts with the formation of the O-rich surface domains, which react with CO producing CO_2 . The lattice oxygen is then replenished from the gas phase. In excess of CO the formation of the O-rich film competes with the film reduction accompanied by dewetting, leading to the deactivation of the catalyst. The proposed mechanism is displayed schematically in Fig. 3.21. The structural information of the oxygen-rich FeO_x film surface will be discussed in Chapter 4.

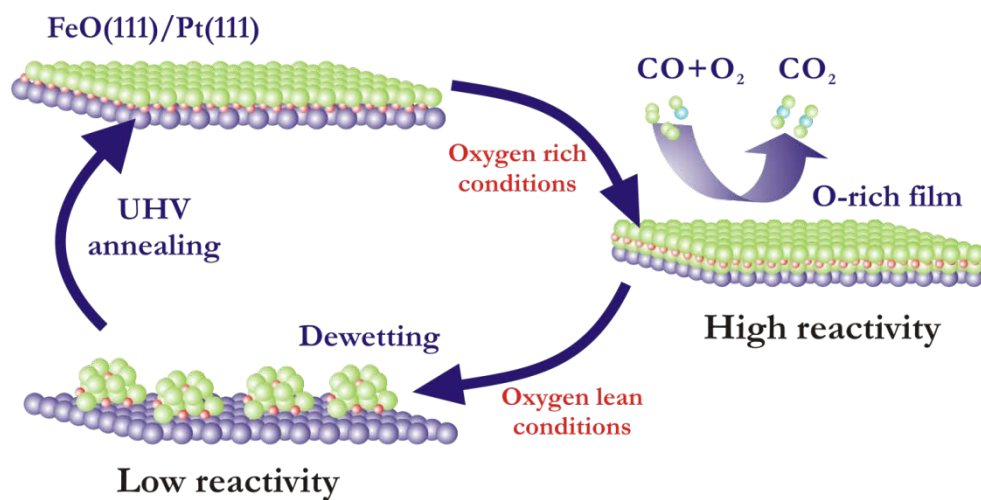


Fig. 3.21 Schematic illustration of the proposed structure transformations of the FeO/Pt(111) at different conditions.

4

Oxidation of the FeO Films

The FeO overlayer on Pt promotes CO oxidation via formation of O-rich FeO film as shown in chapter 3. The oxygen rich iron oxide film formed during the reaction is considered to be the key structure of the reaction. In this chapter, we present both experimental evidences for the structure of the active film, and the theoretical modeling of its formation. The oxidant effect has also been investigated.

4.1. The Structure of Oxygen Rich Iron Oxide Films

The atomic structure of ultrathin FeO(111) film grown on Pt(111) is well established (see Fig. 2.24). The film comprises two close-packed layers of O and Fe stacked as O-Fe-Pt-Pt... . Due to the $\sim 10\%$ mismatch between FeO(111) and Pt(111) hexagonal lattices the surface exhibits the Moiré superstructure with a $\sim 25 \text{ \AA}$ periodicity.

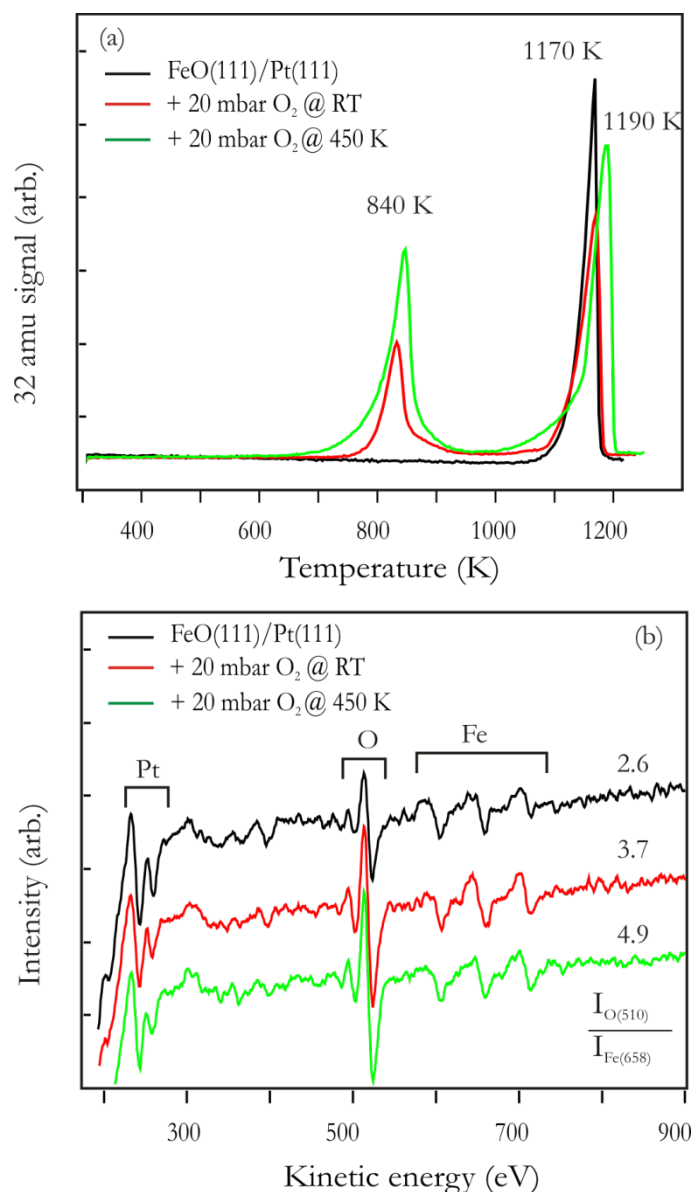


Fig. 4.1 (a) Thermal desorption spectra of a pristine FeO(111) film (black line), an O-rich film produced by exposure to 20 mbar of O₂ at RT (red) and 450 K (green) (32 amu (O₂) signal is shown). **(b)** The corresponding AES spectra are shown in the same color code. The peak ratios for O(510 eV) and Fe(658 eV) are indicated.

At low pressures up to 10^{-3} mbar (at RT) the film is essentially inert towards CO and O₂. The film restructures upon increasing O₂ pressure: It becomes enriched in oxygen and approaches the formal stoichiometry FeO_x ($x \sim 1.8-1.9$) upon exposure to 20 mbar O₂ at 450 K as measured by AES. The oxygen enrichment in these films is further evidenced by TPD. Pristine FeO films show a single O₂ desorption peak at ~ 1170 K as a result of the film decomposition (see Fig. 4.1a). In addition to the high temperature peak at ~ 1190 K, O-rich films exhibit oxygen desorption at 840 K, clearly showing that the O-rich film

possesses two energetically different O species. The integral intensity of the low-temperature peak is 80-90 % of the high-temperature peak, on average, which is in turn almost equal in intensity to that measured on pristine films. This finding is in full agreement with ~90 % enrichment observed by AES. Apparently, upon recombinative desorption of weakly bound oxygen at 840 K, the O-rich film reconstructs back to the bilayer FeO(111) structure and decomposes similarly to the pristine FeO film. Note that the TPD spectra on heating to 1200 K did not reveal water desorption. Only tiny amounts of water, as calibrated by water TPD on pristine FeO [139], was found desorbing in a broad signal at 400 - 700 K upon adding 0.15 mbar of H₂ into 20 mbar of O₂. Therefore, the TPD results suggest no hydroxyls to be present on the O-rich film surface under reaction conditions.

In order to shed more light on differentiating two O-species formed upon high pressure O₂ treatment, the isotopic experiments were performed. Fig. 4.2 shows TPD spectra of the pristine Fe¹⁸O films and the Fe¹⁸O films treated with 20 mbar ¹⁶O₂ at 300 K and 450 K for 20 min. The ¹⁶O¹⁶O signal (32 amu), ¹⁶O¹⁸O signal (34 amu), and ¹⁸O¹⁸O signal (36 amu) were monitored. All three signals at 1170 K have been detected on pristine Fe¹⁸O film upon heating to 1300 K, with the signal 36 as the dominant one, which indicates that the iron oxide film prepared with ¹⁸O₂ mainly contains ¹⁸O atoms. After exposing the film to 20 mbar ¹⁶O₂, in addition to the high temperature peak at ~1170 K, the peak at 840 K appears, which is indicative for the O-rich film formation. The ratios of the two oxygen desorption peaks are basically the same for all three masses (¹⁶O¹⁶O, ¹⁶O¹⁸O, and ¹⁸O¹⁸O). The 34 amu signal has the highest intensity, which means two oxygen layers in the O-rich film basically contain similar amount of ¹⁶O and ¹⁸O, no matter whether were the films treated at 300 K or at 450 K. Therefore, the results suggest that, the O-induced film reconstruction proceeds through the entire iron oxide film, and there seems to be intense O-scrambling between O-layers in the films upon formation of tri-layer film.

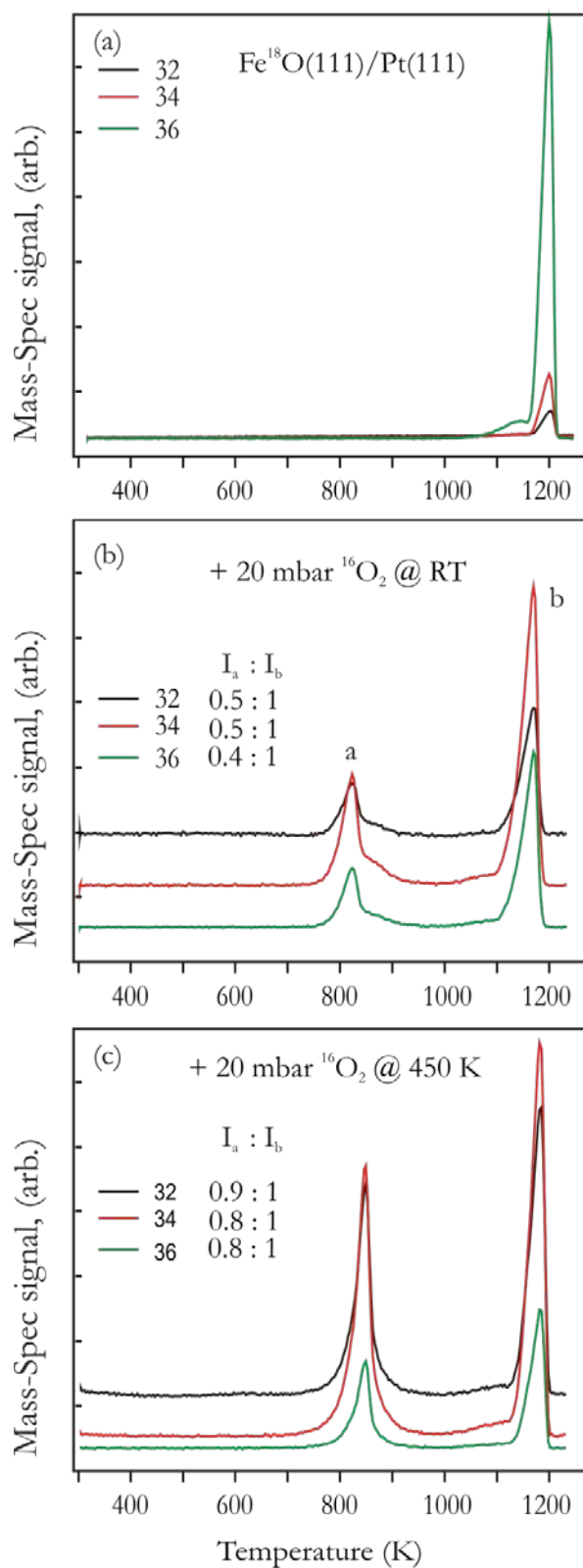


Fig. 4.2 Thermal desorption spectra of a pristine $\text{Fe}^{18}\text{O}(111)$ film (a), an O-rich film produced by exposure to 20 mbar of O_2 at RT (b) and 450 K (c). 32 amu ($^{16}\text{O}_2$), 34 amu ($^{16}\text{O}^{18}\text{O}$) and 36 amu ($^{18}\text{O}_2$) signals are shown. The heating rate is 3 K s^{-1} .

Fig. 4.3a show $100 \text{ nm} \times 100 \text{ nm}$ STM image of the FeO film exposed to 20 mbar O_2 at 450 K for 10 min. It is clear that the oxidized surface exhibits the long-range periodicity very similar to that of FeO. This is also evident from the comparison of LEED patterns shown in Fig. 4.4b. However, in contrast to the pristine FeO films, where the Moiré superstructure is extremely well ordered, the oxidized surface shows a multi-domain structure within the same terrace. The profile line presented in Fig. 4.3c reveals height modulation about 0.6 \AA in amplitude (independent of the bias polarity), i.e., much higher than $\sim 0.1 \text{ \AA}$ observed on the pristine FeO films under the same tunneling conditions (e.g., see inset in Fig. 4.3b). Tentatively, we propose that this effect may be assigned to the formation of well-ordered, planar O-Fe-O islands rather than of a continuous FeO_2 film, or to a wave-like buckling (rumpling) of the Fe and O sub-layers, or both.

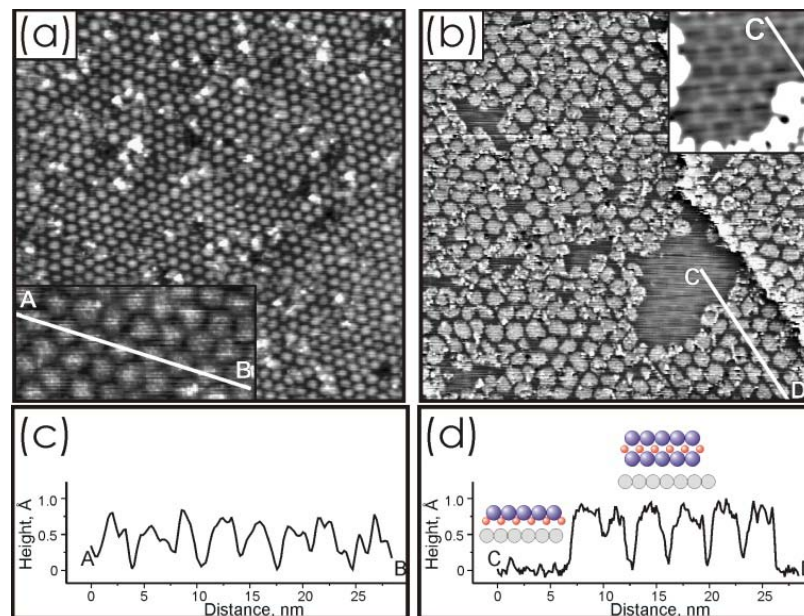


Fig. 4.3 STM images and profile lines of the FeO films exposed to 20 mbar O_2 at 450 K for 10 min (a, c) and 2 mbar O_2 at 300 K for 5 h (b, d). The insets show close-ups of the corresponding surfaces. The Moiré superstructure of the pristine FeO film is shown in the inset of (b). Image sizes are $100 \text{ nm} \times 100 \text{ nm}$ (a) and $50 \text{ nm} \times 50 \text{ nm}$ (b), tunneling bias and current were 1V, 0.7 nA (a) and 0.25 V, 0.3 nA (b). (provided by S. Shaikhutdinov and M. Lewandowski)

The phase stability of the FeO film indeed strongly depends on the oxygen chemical potential. The FeO film treated with 20 mbar O_2 at 300 K results in partial surface restructuring, as revealed by AES and TPD (see Fig. 4.1), showing lower extent of O-enrichment ($\text{FeO}_{1.4}$) as compared to the film treated with O_2 at 450 K ($\text{FeO}_{1.8}$). These results indicate the presence of the pristine FeO surface and the reconstructed surface

upon treatment at 300 K, which allows us to measure the height difference between them. The height measured, i.e., $\sim 0.65 \text{ \AA}$ as shown in Fig. 4.3b, basically coincides with a FeO interlayer distance on FeO(111)/Pt(111) measured by photoelectron diffraction [135]. This finding is fully consistent with the formation of additional O-layer upon film restructuring as schematically shown in Fig. 4.3d.

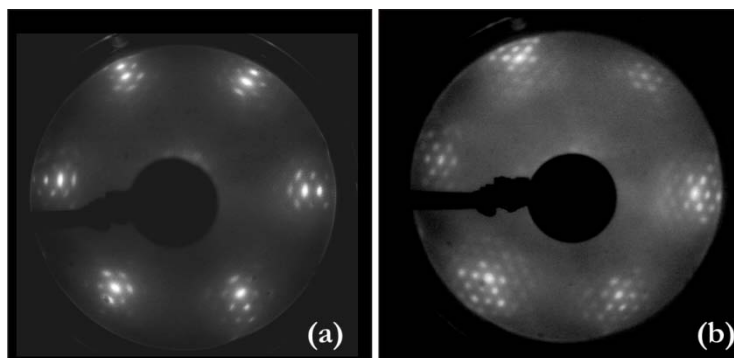


Fig. 4.4 LEED patterns ($E=60 \text{ eV}$) of a pristine FeO film (a) and an O-rich film by exposure to 20 mbar of O_2 at 450 K (b).

A comparative analysis of the LEED patterns where Pt and FeO diffraction spots are clearly distinguished was performed. The analysis reveals that the lattice constant of the oxide film decreases from 3.09 \AA to 3.05 \AA , on average. Indeed the same trend of the film reconstruction upon oxidation was found by STM. Fig. 4.3b shows that the Moiré lattice on the oxidized FeO_{2-x} patches is expanded by $\sim 3 \%$, as compared to the FeO film. (On the fully oxidized surfaces formed at $\sim 450 \text{ K}$ the expansion, as measured by STM, is apparently larger (up to 10%)(see Fig. 4.3a), although the uncertainty is higher, too.) In general, there is an inverse relation between the lattice constants of the oxide layer and the Moiré superstructure: The smaller the lattice constant of FeO(111), the larger the Moiré cell, and vice versa. Therefore, the STM results suggest that the lattice constant of the FeO_{2-x} film is slightly shorter than that of FeO(111). To accommodate these small changes while maintaining a coincidence superstructure, the transformation of the FeO film into the FeO_{2-x} film must be accompanied by a small rotation with respect to the Pt(111) substrate. High-resolution STM images revealed even more structural complexity of the oxidized films (see Fig. 4.5). It has turned out that the FeO_{2-x} island surfaces exhibit a $\sqrt{3} \times \sqrt{3} R30^\circ$ structure with respect to the pristine FeO(111) more clearly seen in Fig. 4.5b [166].

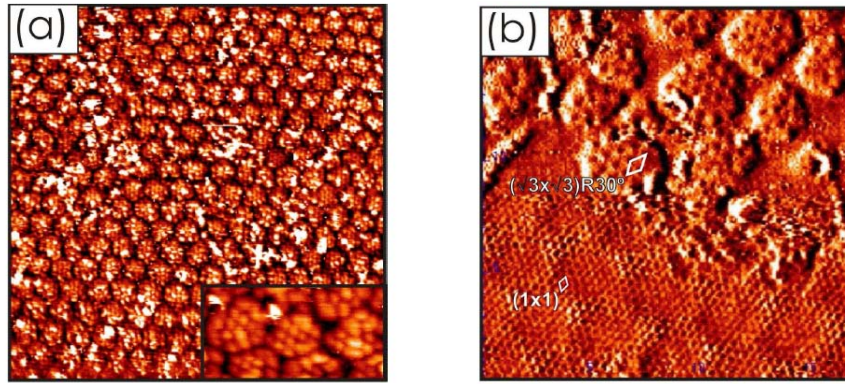


Fig. 4.5 (a) $100 \text{ nm} \times 100 \text{ nm}$ STM image of the FeO film exposed to 14 mbar of O_2 at 450 K for 10 min. The inset zooms in the $\sqrt{3} \times \sqrt{3} R30^0$ structure with respect to pristine FeO, which is more clearly observed in the image (b), presented in the differentiated contrast. (b) $100 \text{ nm} \times 100 \text{ nm}$ image of the FeO film exposed to 0.5 mbar of O_2 for 10 min at 350 K. The unit cells are indicated. Tunneling bias and current are 0.25 V, 0.7 A (a); 1.0 V, 0.7 nA (b); 0.1 V, 0.7 nA (inset), respectively. (provided by M. Lewandowski [166])

To explain the observed STM contrast, one could, in principle, address the stoichiometry of the oxidized film. In order to create the $\sqrt{3} \times \sqrt{3} R30^0$ structure within the ideal FeO_2 film proposed in the model, one could remove $1/3$ or $2/3$ of the O atoms in the topmost close-packed O-layer. (Note that the amount of Fe does not change during oxidation). This model would result in $\text{FeO}_{1.66}$ and $\text{FeO}_{1.33}$ stoichiometry, respectively. The TDS and AES results showing $\text{FeO}_{1.8}$ stoichiometry are in consistent with models suggesting an oxygen deficiency in the topmost O-layer. In addition, we find that the observation of the $\sqrt{3} \times \sqrt{3} R30^0$ structure by STM is not limited to the particular tunneling conditions and bias polarity. This favors the conclusion that the STM contrast is determined by Fe rather than O species forming electronic states near the Fermi level. Therefore, the combined STM, TDS and AES results suggest a buckling of the Fe layer upon oxidation. This structure was rationalized by DFT calculations [166] in terms of strong relaxations within the Fe sub-layer and can be considered as an intermediate state in the transformation of the $\text{FeO}(111)$ into $\text{Fe}_2\text{O}_3(0001)$ film.

The proposed structure and CO oxidation mechanism were fully supported by DFT calculations by Pacchioni's and Noguera's groups [167]. DFT results suggested that the formation of the tri-layer film as follows (see Fig. 4.6): (i) O_2 chemisorbs molecularly with adsorption energy of 0.7 eV on the Fe atom, which is pulled out from the pristine FeO film. The presence of a small barrier (0.3 eV) to reach the chemisorbed state implies that an

oxygen pressure is necessary, since thermal activation would result in O₂ desorption. (ii) In the chemisorbed state electrons are transferred from the oxide/metal substrate, and adsorbed O₂ becomes negatively charged. The O-O bond length expands to 1.46 Å, and the magnetic moment is fully quenched, indicating the formation of O₂²⁻ peroxy species. Such an electron transfer is enabled mainly by a local inversion of the rumpling in the oxide film which lowers locally the work function of the support ($\Delta\Phi \sim -1.5\text{eV}$), similar to transition metal ad-atoms on metal-supported oxide films (see introduction). (iii) The activated O₂ then dissociates relatively easily at mild temperature (0.4 eV), resulting in the formation of an O-Fe-O tri-layer structure with FeO₂ stoichiometry, with a total energy gain of 3 eV.

The reaction with CO involves the extraction of an oxygen atom from the oxide film with formation of a CO₂ molecule leaving behind an oxygen vacancy. This reaction occurs by overcoming a barrier of ~ 0.2 eV, which is considerably lower than the computed barrier on Pt(111), of the order of 1 eV. The cost for CO₂ desorption is only 0.3 eV. The formation of a strong C-O bond in CO₂ overcompensates the cost of removing an O atom such that the overall reaction is highly exothermic, with a computed enthalpy of -1.9 eV. This is due to the relatively low formation energy of an oxygen vacancy on the FeO₂/Pt(111) surface (1.3 eV with respect to 1/2O₂), about one-half of that calculated for the pristine FeO film (2.8 eV). This finding is in full agreement with the TDS results shown in Fig. 4.1, where oxygen desorbs from FeO-rich films at much lower temperature than from FeO. To end the catalytic cycle via the Mars-van Krevelen type mechanism the oxygen vacancies must be replenished through the reaction with gas-phase oxygen that restores the original stoichiometry of the film.

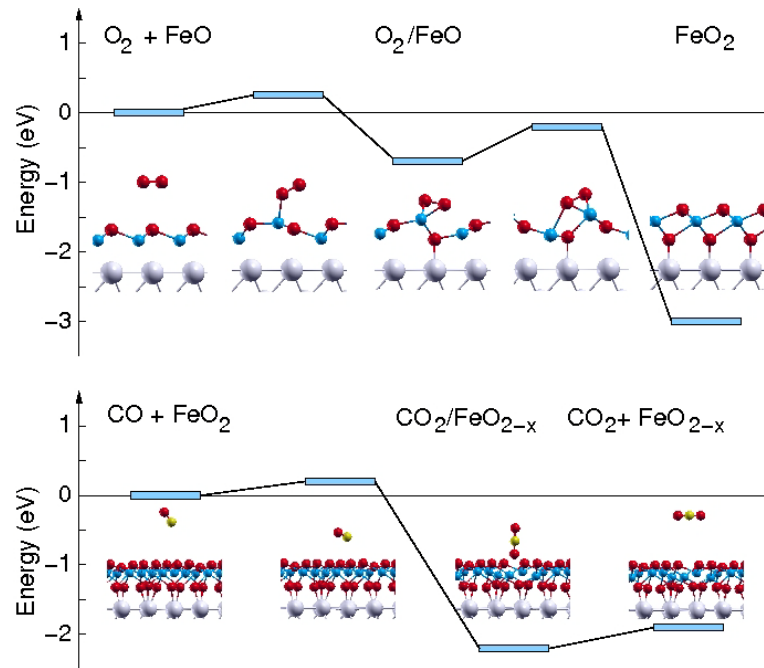


Fig. 4.6 (top) Energy profile for oxidation of the FeO/Pt(111) film on exposure to O_2 at high oxygen coverage. (bottom) energy profile for CO oxidation on FeO₂/Pt(111) film at low CO coverage. Fe blue, O red, C yellow, Pt gray. (from [167])

4.2. The Effect of Oxidants (NO vs. O₂)

In attempts to shed light on the possible effects of the oxidants on structure and reactivity of thin oxide films, we have investigated the reaction of CO+NO. In addition, the choice of NO is also due to the great importance of the reaction of CO and NO in automotive exhaust catalysis.

Before turning to reactivity study under ambient conditions, we studied the interaction of NO with Pt(111) single crystal and FeO(111) films under UHV conditions. In Fig. 4.7 the TPD spectra of NO adsorbed on surfaces are displayed as a function of exposure at 100 K. The spectra are obtained by monitoring the 30 signal while applying a constant heating rate of 3 Ks⁻¹. On Pt(111), three distinct desorption states were observed at saturated coverage, usually designated as the α , β , and γ states, desorbing at 200 K, 324 K and 373 K respectively. Based on the literature results [168-173], the γ state corresponds to a NO coverage of $\theta = 0.25$ ML, and can be assigned to NO adsorbed on the (111) facets in fcc sites. With increasing coverage, a second peak at 324 K emerges, corresponding to the β state, and can be attributed to NO occupying on-top sites. Upon further increasing to the saturation coverage of $\theta = 0.75$ ML, the third peak at 200 K develops, correlated with the γ

state, and can be ascribed to NO populated on hcp sites. It should be noted that NO does not dissociate on the Pt(111) surface.

The bonding of NO on transition metal surfaces is usually within the scope of the Blyholder model [174, 175], proceeding via σ -donation and π -back donation, which results in strong bonding with chemisorption energies between 100 and 200 kJ/mol. For the interaction of molecules with oxide surfaces, electrostatic forces and Pauli's repulsion dominate, resulting in rather weak adsorption. Hence, a weaker interaction of NO with FeO(111) films are expected. As shown in Fig. 4.7, two desorption peaks at 165 K and 218 K were obtained. The peak temperatures are lower than those on Pt(111), which confirms the expectation. In addition, there is no observation of signal 44 (N_2O and CO_2), 28 (CO and N_2) or 46 (NO_2), which indicates that NO dissociation does not occur on the FeO(111) surfaces. Furthermore, as compared to CO molecules, NO interacts with the FeO films more strongly, since CO does not adsorb on the same surface at the temperatures above 100 K under UHV conditions.

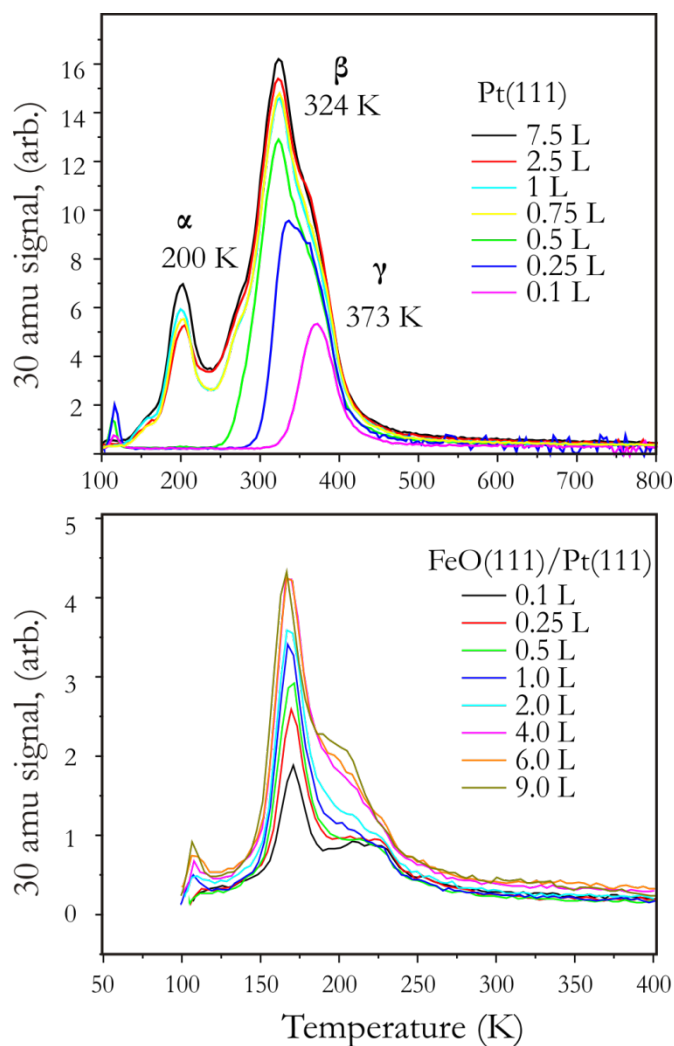


Fig. 4.7 TPD spectra of NO on Pt(111) (top) and FeO(111) (bottom) as a function of NO exposure at 100 K. The heating rate is 3 K s^{-1} .

FeO(111) films after exposure to 20 mbar NO at two different temperatures, 300 K and 450 K exhibited long-range ordering structure of the films as revealed by LEED, which almost identical to the LEED pattern observed on the O-rich iron oxide films treated by O_2 . The TPD spectra of the FeO films treated by NO are displayed in Fig. 4.8. As in the case of O_2 , two oxygen desorption states at 840 K and 1190 K are observed. Again, the 1190 K peak is ascribed to the desorption of oxygen from FeO; the sharp peak at 840 K is attributed to the desorption of new O-species formed upon oxidation by NO. The fact that integral amounts of NO adsorbed on FeO is $\sim 5\%$ of that on Pt(111) suggests that NO probably adsorbs on defect sites of FeO films.

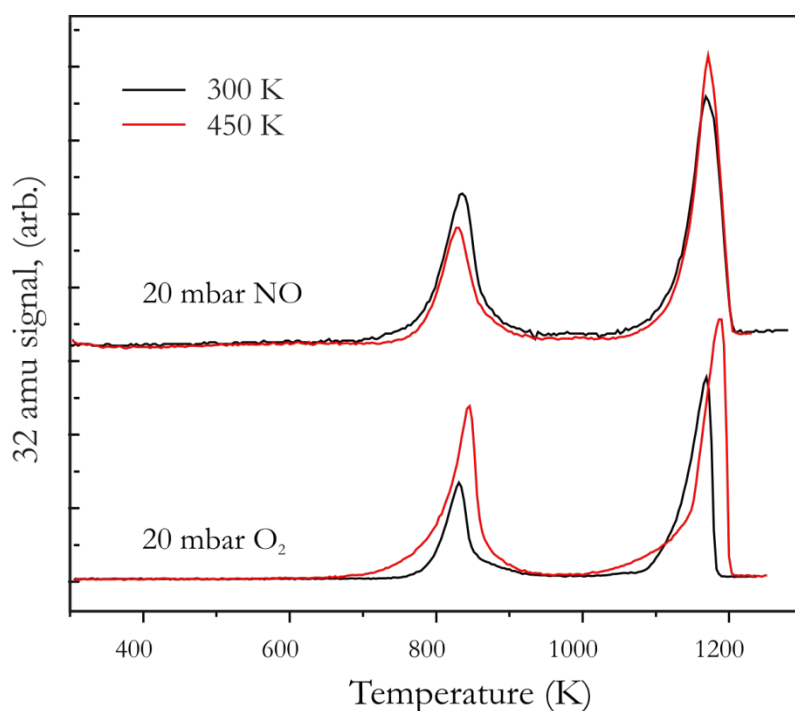


Fig. 4.8 TPD spectra of the decomposition of the FeO(111) films after exposing to 20 mbar of pure NO and pure O₂ at 300 K and 450 K for 20 min. O₂ (32 amu) signal is monitored. The heating rate is 3 Ks⁻¹.

The O:Fe ratios in the films oxidized by O₂ and NO are shown in Tab. 4.1. The AES results also provide additional evidence for the O-enrichment upon oxidation treatment, which are in good agreement with the TPD results. It is noteworthy that there is no indication of N incorporation with the films after the NO treatment, neither by AES nor TPD. However, the O-content of the films prepared by O₂ increases with increasing temperature (from 300 K to 450 K), whereas the treatment with NO follows the opposite trends, that is the integral intensity of the low-temperature peak is 70 % of the high-temperature peak of the film treated at 300 K, and only 50% at 450 K. This effect may be related with the different activation barriers of the film transformation.

NO was also used to characterize FeO surfaces as a probe molecule. Fig. 4.9 displays TPD spectra of the fresh FeO films and the O-rich iron oxide films upon adsorbing saturated amount of NO at 100 K and subsequently heating to 600 K. The comparison of two sets of spectra shows that NO adsorbed on O-rich iron oxide films, no matter prepared by NO or O₂, desorbs at temperatures ~85 K higher than NO adsorbed on fresh FeO(111) films. These findings again confirm that the structure of the O-rich iron oxide

films is different from that of fresh FeO films, and the interaction of NO with the FeO films is similar to that of O₂.

Tab. 4.1 O-content of different iron oxide films treated by NO and O₂ at 300 K and 450 K determined by TPD and AES measurements.

Oxidants (20 mbar)	O:Fe (TPD)		O:Fe (AES)	
	300 K	450 K	300 K	450 K
NO	1.7	1.5	1.7	1.5
O ₂	1.4	1.9	1.5	1.9

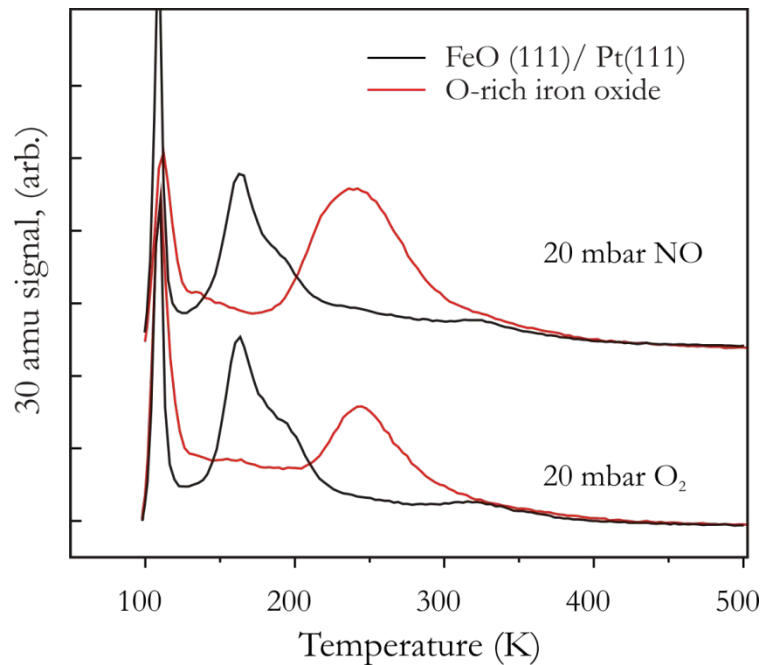


Fig. 4.9 TPD spectra of the fresh FeO films and the O-rich iron oxide films prepared by NO and O₂ oxidation upon adsorbing saturated amount of NO (7.5 L) at 100 K. The heating rate is 3 Ks⁻¹.

In the next step, CO+NO reaction under mbar pressure range has been investigated. Fig. 4.10 shows CO₂ formation in the mixture of 10 mbar CO and 50 mbar NO balanced by He up to 1 bar at 450 K on FeO surfaces. The CO lean condition is chosen since the O-rich phase is more stable under this condition. The same experiment for CO + O₂ is shown for comparison. The most striking observation is that in contrast to CO + O₂, the

CO_2 production from $\text{CO} + \text{NO}$ is negligible. Moreover, the reaction at 400 K results in an even more rapid deactivation.

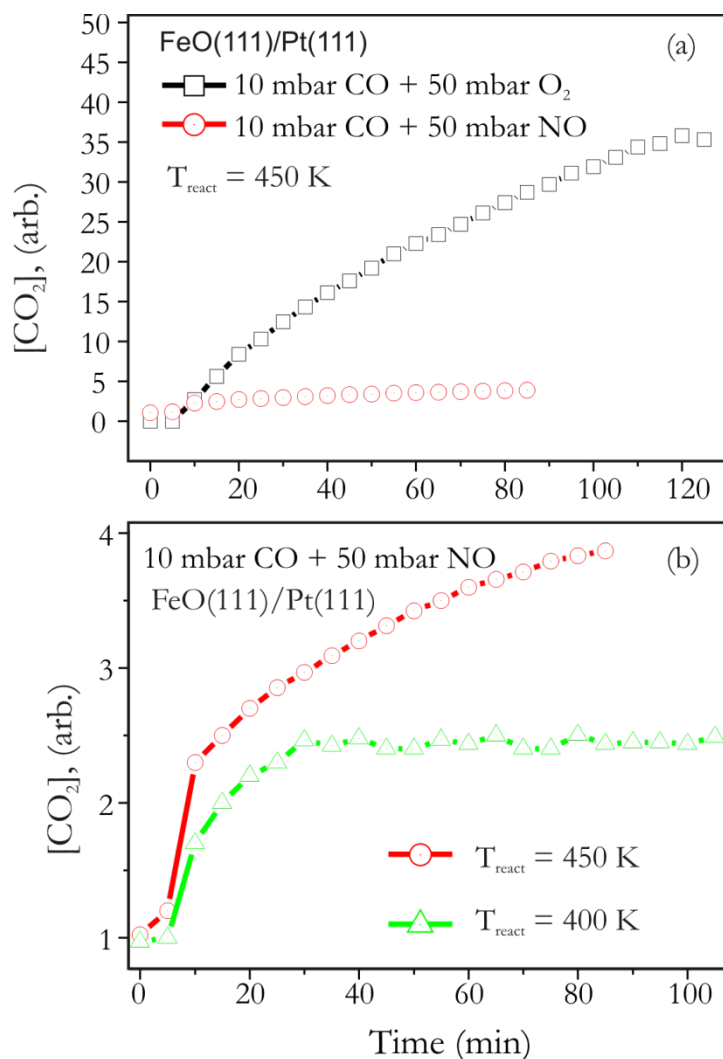


Fig. 4.10 Kinetics of CO_2 production over $\text{FeO}(111)/\text{Pt}(111)$. (a) 10 mbar $\text{CO} + 50 \text{ mbar NO}$ and 10 mbar $\text{CO} + 50 \text{ mbar O}_2$ at 450 K (b) 10 mbar $\text{CO} + 50 \text{ mbar NO}$ at indicated temperatures. Time zero corresponds to the start of the sample heating (1 K s^{-1}) from 300 K.

The post reaction characterization shows that after $\text{CO} + \text{NO}$ reaction at 450 K for 2 hours, the spent catalyst displays diffuse $\text{Pt}(111)$ spots, which is different from the FeO -like LEED pattern observed after $\text{CO} + \text{O}_2$ reaction at 450 K.

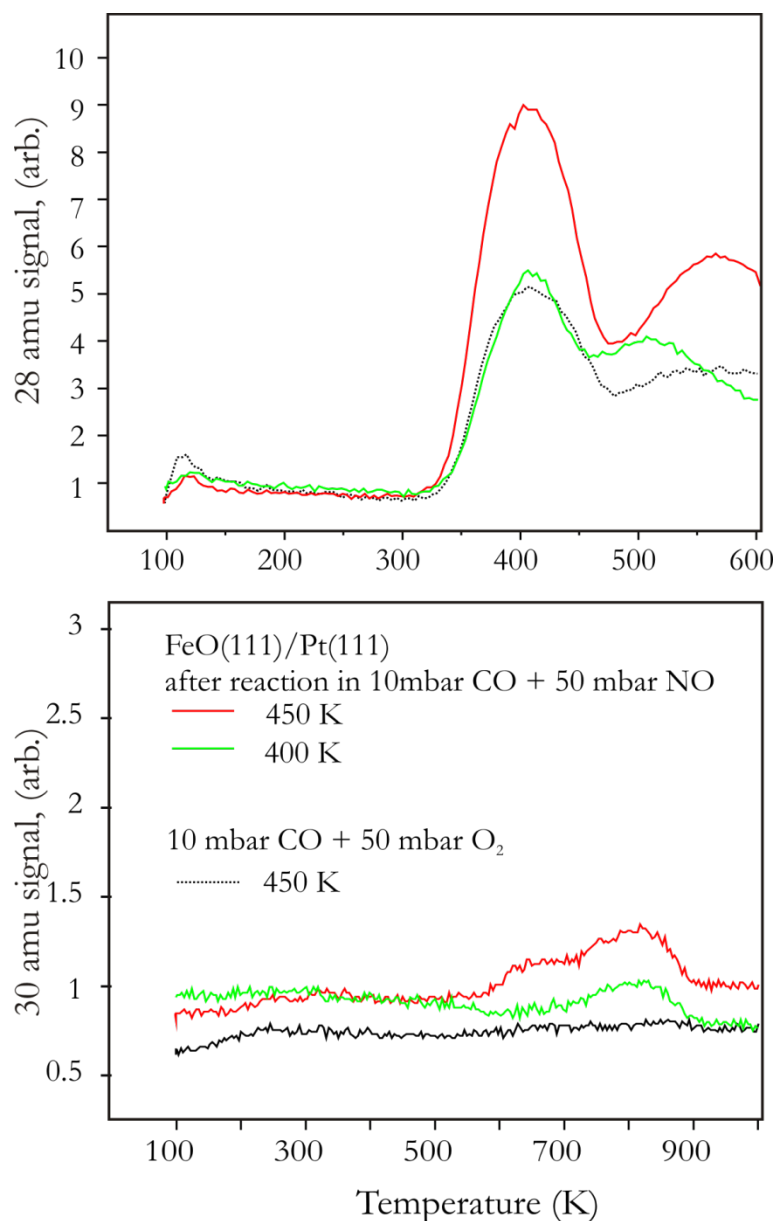


Fig. 4.11 CO (28 amu) and NO (30 amu) signals in TPD spectra of a FeO(111)/Pt(111) film reacted in 10 mbar CO + 50 mbar NO for 120 min at indicated temperatures. The spectrum of a FeO(111)/Pt(111) reacted in 10 mbar + 50 mbar O₂ for 120 min is shown in dotted line for comparison. The heating rate is 3 Ks⁻¹.

Further information on the structure of the spent samples was obtained by TPD. In CO + O₂ reaction, only CO and CO₂ were found as desorbing species upon heating of the spent sample in UHV. The desorption peak at 380-390 K is assigned to CO adsorbed on dewetted Pt surfaces in the course of the reaction, while the peak at T > 500 K may be attributed to the reaction of carbonaceous species with surface oxygen. The integrated area of the CO TPD signal between 300 K and 500 K is used to estimate the degree of dewetting, by using the TPD spectrum for CO/Pt(111) as a reference (see chapter 3). The

same desorption features have been observed on the spent catalysts after the CO + NO reaction as displayed in Fig. 4.11. It is found that after 2 hours of the reaction, less than 5% of the surface expose the clean Pt(111) substrate, though slightly larger than that from the sample used in the CO + O₂ reaction. This finding is in line with the LEED observation, which implies that the reconstruction of the surface due to the reaction seems to be stronger in the CO + NO reaction.

One important observation is that, during the TPD process, in addition to CO and CO₂ desorption, a broad 30 amu signal between 600 and 900 K was observed. This signal must be attributed to the reaction limited desorption of NO due to recombination of N-species with O from the surface, which may indicates the incorporation of N with the FeO film in the course of the reaction, since this signal is absent on the surface treated with pure NO. The fact that N was not observed in samples treated with NO only indicates that this incorporation (if any) occurs in the course of the CO + NO reaction.

One may raise the question such that: why the reactivity of the reaction CO + NO is so different from the reaction CO + O₂ under the same conditions, since both NO and O₂ could interact with FeO(111) films and form virtually identical O-rich iron oxide surfaces. We assume that CO oxidation reaction proceeds as follows:

1. NO (O₂) interacts with the film, forming O-rich iron oxide structure.
2. CO interacts with the O-rich films, forming CO₂ that desorbs and leaves the oxygen vacancy.
3. The replenishment of O vacancies with NO (O₂) occurs to restore the O-rich film.

The first step has been discussed in detail in the section 4.1. It is concluded that NO interacts with the FeO films in the similar way as O₂ does. For the second step, the energy barrier for extracting an O atom from the surface by CO should be the same in both reactions. Therefore, the third step is likely the rate limiting step. Indeed, the TPD study on the spent catalyst after CO+NO reaction showed incorporation of N-species in the film in the course of the reaction, which may results in inhibiting the O-replenishment by NO.

Pt Particles on Fe₃O₄ (111)

This chapter provides results on the characterization of Pt/Fe₃O₄(111) model catalysts, including the identification of different CO adsorption sites, CO dissociation, and SMSI effects. CO oxidation reaction has been investigated on Pt/Fe₃O₄(111) at realistic conditions to compare with FeO/Pt(111) system studied in previous Chapters.

5.1. Preparation and Structure

Pt particles supported on metal oxides are widely used in many industrially important catalytic processes, such as CO oxidation, PROX in polymer electrolyte fuel cells, etc. Structure and reactivity of Pt model systems such as Pt/TiO₂(110) and Pt/CeO₂(111) have been studied quite extensively by using surface science techniques [176-181]. Less is known about the interaction of Pt particles with iron oxide surfaces. It has turned out that metal deposited on FeO films (as well as ultrathin alumina films [182]) exhibits low thermal stability. Metal particles may migrate into the metal substrate underneath through the film. On the contrary, Fe₃O₄(111) film can be grown thick (~10nm) on Pt(111), which ensures the relatively high thermal stability of the Pt/Fe₃O₄.

Pt particles are deposited on Fe₃O₄(111) films by PVD with desirable coverages at 100 K under UHV conditions. During each Pt evaporation iron oxides were biased to a retarding voltage in order to decelerate Pt ions, which otherwise may induce defects affecting the particles growth. By choosing appropriate preparation conditions, a certain size distribution of metal particles can be obtained. It is essential to note that the growth of metal particles depends strongly on the strength of the metal-support interaction. Strong interaction results in the formation of a high density of nucleation centers and hence a large number of small aggregates. On the other hand, weak interaction gives rise to the

formation of larger particles of low density. STM studies showed that Pt particles on Fe₃O₄ exhibit a rather broad lateral size distribution and random dispersion on the iron oxide terraces with almost no decoration of the step edges, indicating relatively strong Pt-Fe₃O₄ interaction [183, 184]. Certainly, the growth of the Pt particles at 100 K may be a kinetically limited process, leading to the formation of disordered aggregates and non-equilibrium shapes. Therefore, in this work, Pt particles grown at 100 K were annealed in vacuum at 600 K for 5 min in order to eliminate structural changes. Large-scale STM images of Pt/Fe₃O₄(111) surfaces are displayed in Fig. 5.1. Pt particles grow on a Fe₃O₄(111) film via the same epitaxial relationships as between the film and the Pt(111) substrate underneath [183, 184]. Interestingly, at sub-monolayer coverages Pt forms two-dimensional islands of ~ 0.5 nm in height, that roughly corresponds to 2 layers of Pt(111) (see Fig. 5.1a). These particles exhibit mostly an irregular shape, although some preferential orientation for the island edges can be seen. At high coverages, large, well-faceted three-dimensional Pt particles up to 1 nm in height are formed, exposing atomically flat Pt(111) top facets as shown in Fig. 5.1b.

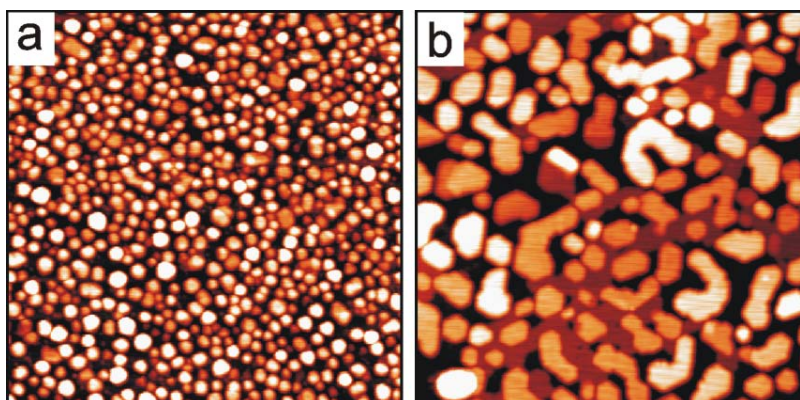


Fig. 5.1 STM images of the Pt/Fe₃O₄(111) surface annealed to 600 K in UHV for 5 min at 0.8 ML Pt (a) and 2.6 ML (b) Pt coverages. Image size is 100 nm x 100 nm; tunneling bias and current are $V = 1.4$ V, $I = 1$ nA (a); 1.4 V, 0.7 nA (b). (provided by Z.-H. Qin and M. Lewandowski)

5.2. CO Adsorption on Fe₃O₄(111) Supported Pt Particles

Adsorption properties of the iron oxide Fe₃O₄ supported Pt particles have been probed by CO TPD. Before turning to the details on CO adsorption on Fe₃O₄ supported Pt particles, we recall adsorption of carbon monoxide on platinum surfaces, which is one of the most explored reactions in surface science (see [154] and references therein). The process is well explained by the Blyholder model [174, 175]: The chemical bond between

CO and Pt is formed in terms of electronic charge transfer from the weakly bonding 5σ MO of CO into the highly dispersed empty conduction bands of metal and backdonation from the occupied metal d-bands into the unoccupied $2\pi^*$ anti-bonding MO of CO. The backdonation depends very sensitively on the geometry and local electronic structure of the adsorption sites, which provides the possibility to identify different adsorption sites. Generally, enhanced CO adsorption energies at surface defect sites such as step edges or kinks, which possess reduced coordination, are expected. Indeed it has been reported that the binding energy of CO depends on the Pt surface structure. From surfaces with the low Miller indices CO desorbs in a relatively broad signal, between 300 K and 550 K, in TPD spectra [9, 11, 16, 147, 148]. Stepped and kinked Pt surfaces typically exhibit two distinct desorption states, i.e. at ~ 400 and 500 K [10, 11, 13]. The low temperature state centered at ~ 400 K has been attributed to the (111)-like terraces, while the high temperature state (above 500 K) to the CO adsorption on low-coordination sites. Basically, a similar assignment was applied for supported Pt particles [180, 185-187]. For example, Pt particles, deposited at low coverage both on amorphous alumina and α -Al₂O₃(0001) supports at 300 K, showed a single desorption state at ~ 510 K, while the larger particles revealed an additional desorption state at ~ 400 K [185, 186].

In this work, CO adsorption on the Pt particles has been systematically studied as a function of the particle size. Fig. 5.2a shows CO TPD spectra of a Pt/Fe₃O₄(111) surface annealed to 600 K at different Pt coverages. The low temperature signals, i.e., below 200 K, were observed on the pristine films prior to Pt deposition (see Fig. 2.26). The highest desorption state, found for the clean films, i.e. at ~ 230 K (see also Fig. 2.26), has been associated with defects sites, which are now decorated by Pt and are, therefore, not visible in the spectra presented. Thus, three desorption peaks, centered at 270, 400 and 480 K, with the coverage-dependent intensity ratios are related to Pt particles. The latter peak is more pronounced at the low Pt coverage, whereas the signals at 400 and 270 K gain intensity with increasing coverage. On the basis of the literature results discussed above, the desorption states at 400 and 480 K can be explained in terms of CO adsorbed on Pt(111) facets and low-coordination sites, respectively. To validate this assignment, Fig. 5.2b depicts a TPD spectrum of CO obtained on the Pt(111) surface produced by 1 keV Ar⁺ ion sputtering at 300 K and subsequent annealing at 600 K for 5 min. This treatment yields a rough surface with a small width of Pt(111) terraces and a high density of low-coordination sites (step edges and kinks), as illustrated by the STM image in Fig. 5.2b (see

also [14]). Besides the main TPD signal from the Pt(111) surface (centered at 400 K), an additional peak at ~ 510 K is clearly seen, that is attributed to CO adsorption on the low-coordinated Pt atoms.

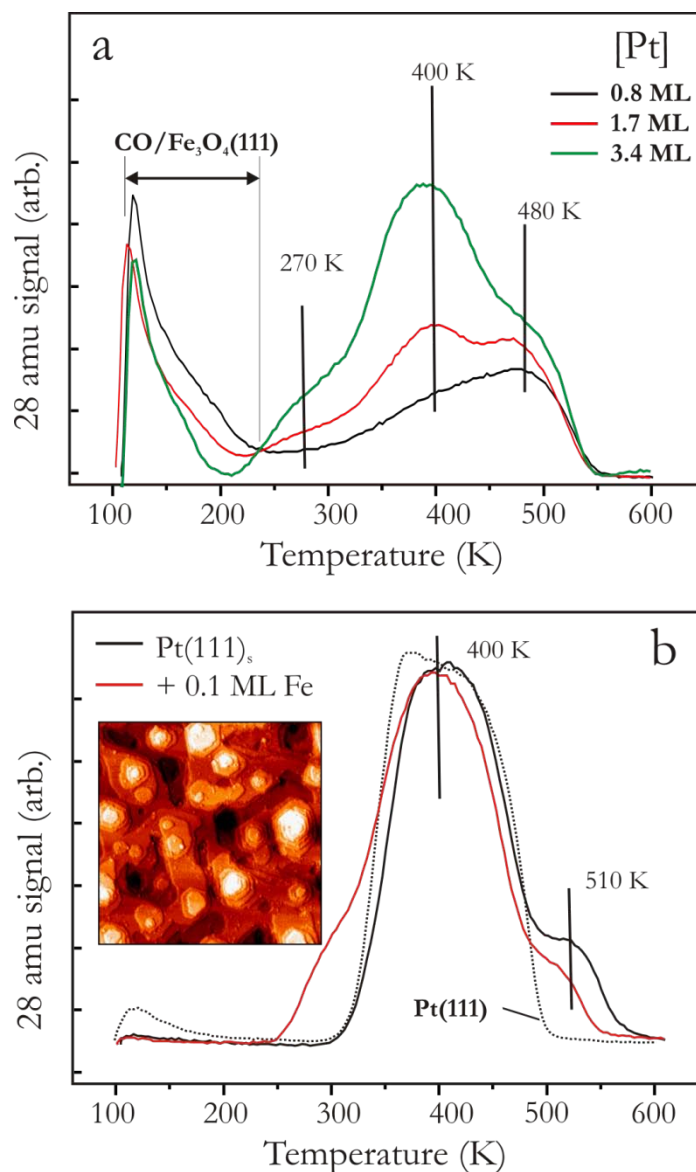


Fig. 5.2 (a) TPD spectra of CO on Pt/Fe₃O₄(111) annealed at 600 K for 5 min as a function of Pt coverage as indicated. (b) TPD spectra of CO on the stepped Pt(111) surface prepared by 1 keV Ar⁺ sputtering at 300 K and annealing at 600 K for 5 min, denoted as Pt(111)_s. Subsequently, 0.1 ML of Fe were deposited onto Pt(111)_s surface and annealed for 5 min at 600 K prior to CO adsorption. TPD spectrum of CO on clean Pt(111) surface is shown in dashed line for comparison. 7.5 L of CO were dosed at 100 K in each case. The heating rate is 3 K/sec. STM Image in (b) (provided by M. Lewandowski), presented in differentiated contrast, shows a Pt(111)_s surface. Image size is 100 nm x 100 nm; tunneling bias and current are V = 0.7 V, I = 0.4 nA.

In Fig. 5.2a the 270 K state is absent on the roughened Pt(111) surface, which indicates that this state is intrinsic to the Pt/Fe₃O₄(111) surface. One could, in principle, associate this feature with other than (111) facets, constituting a particle surface, such as (100) and, to a lesser extent, (110) [188]. However, to the best of our knowledge, these two surfaces do not exhibit such a low temperature desorption peak [12, 15, 189-191]. In fact, the Pt(100) surface exhibits a desorption peak at higher temperature than that of Pt(111). Finite size effects are unlikely, too: The particles contain hundreds of Pt atoms, on average, and showed almost bulk behaviour in x-ray photoelectron spectra (not shown). If the 270 K state were the metal/oxide interfacial sites, one would expect to have more of these sites at low Pt coverage where the particles are smaller and the density is higher (see Fig. 5.1). In fact, Fig. 5.2a shows that the intensity of the 270 K signal scales with Pt coverage.

We have tentatively linked the 270 K signal to the interaction of Pt particles with the Fe₃O₄(111) support. This interaction could, in principle, result in the support material (Fe, O) migration onto the Pt particles at 600 K. An O spillover onto Pt seems to be hardly possible since the affinity of Pt for oxygen is obviously lower than that of Fe. Therefore, we first address Fe migration onto Pt. To examine this hypothesis, we studied CO adsorption on 0.1 ML Fe deposited onto the stepped Pt(111) surface at 300 K and subsequently annealed in UHV at 600 K for 5 min, i.e. as in the case of Pt/Fe₃O₄. For this low Fe coverage one would expect Fe decorating the step edges. However, according to infrared studies [192] and Monte-Carlo simulations [193], the Fe atoms may also migrate into the sub-surface region of Pt at temperatures above ~ 450 K. Nonetheless, Fig. 5.2b shows that the intensity of the high temperature peak (~ 510 K) on the Fe/Pt(111) surface is reduced by a factor of 2, while the CO capacity of the (111) terraces is almost unchanged. Interestingly, the new CO desorption state emerges below 300 K, i.e. very similar to that observed on the Pt/Fe₃O₄ surface (see Fig. 5.2a). Weakening of the CO bond on Pt-Fe surfaces has previously been reported for the Pt-terminated Pt₈₀Fe₂₀(111)-(2x2) surface, where a main desorption peak is observed at ~ 340 K [194]. The similar downshift of CO desorption by surface alloying with other metals has also been reported, e.g. on Pt-Sn [195] and Pt-Ce [196] surfaces. Therefore, the results indicate that the 270 K peak observed on the Pt particles originates from Fe migration onto the Pt particles or partial Pt-Fe intermixing upon heating to elevated temperatures.

5.3. CO Dissociation on Pt/Fe₃O₄(111)

Another important question concerning chemisorption of CO on Pt surfaces is that whether CO dissociates on the surfaces or not? The dissociation of CO forming active carbon is an essential step for Fischer-Tropsch synthesis [197]. It was generally believed that Pt does not or hardly dissociate CO, although controversial results were reported [10, 11, 13, 147, 198-201]. Somorjai and co-workers first showed that CO dissociation on Pt is, in fact, a surface structure sensitive reaction [198]. Using x-ray photoelectron spectroscopy, they observed carbon deposition upon CO adsorption on the Pt(s)-6(111)x(710) surface. The Pt atoms at steps and kinks were assigned to the sites for CO dissociation. Using field emission microscopy of a Pt single crystal rod, Li and Vanselow [200] also showed that the kinked areas facilitate CO dissociation. In contrary, no indication of CO dissociation on the stepped or kinked surfaces of Pt was found by Hopster and Ibach [11] using high resolution electron energy loss spectroscopy and TPD under their experimental conditions. However, they did find some evidence for a minority species characterized by a rather low C-O stretch frequency which were proposed to be due to the adsorption at kink sites and may indicate that CO tends more toward dissociation at these sites than on others.

The CO dissociation was also clearly observed at elevated CO pressures. Using SFG at 40 Torr of CO and AES, McCrea et al. showed that CO dissociation emerges on Pt(111), Pt(557) and Pt(100) at 673, 548 and 500 K, respectively [202]. The authors suggested that dissociation proceeds via CO-induced surface roughening at high pressures and temperatures, but this mechanism was revisited in the more recent work by Rupprechter et al. [100].

In this work, the ability of Fe₃O₄(111) supported Pt particles to dissociate CO has been studied. We have first investigated the stability of Pt/Fe₃O₄(111) upon CO adsorption under UHV conditions. In Fig. 5.3 repeated CO TPD spectra on 1.7 ML Pt/Fe₃O₄(111) are displayed. Both CO signal (28 amu) and the CO₂ signal (44 amu) were monitored. Two CO₂ desorption peaks are observed at ~ 150 and ~ 500 K, which are definitely not due to CO cracking in the mass-spectrometer. The signal at 150 K has been detected on pristine Fe₃O₄(111) films and thus assigned to CO₂ adsorption on the oxide surface from the vacuum background upon cooling the sample to 100 K. The experiments with CO on O-precovered Pt(111) revealed CO₂ formation in a broad peak between 300 and 400 K (see Fig. 3.5), which is missing in these spectra. Although there is some CO₂ intensity at around

200 and 300 K, which could, in principle, be assigned to CO + O reaction on Pt(100) facets [191], the signal does not change upon repeating the spectra and most likely originates from the heating wires, etc. and thus can be neglected. Therefore, the results show no evidence for O spillover onto Pt particles.

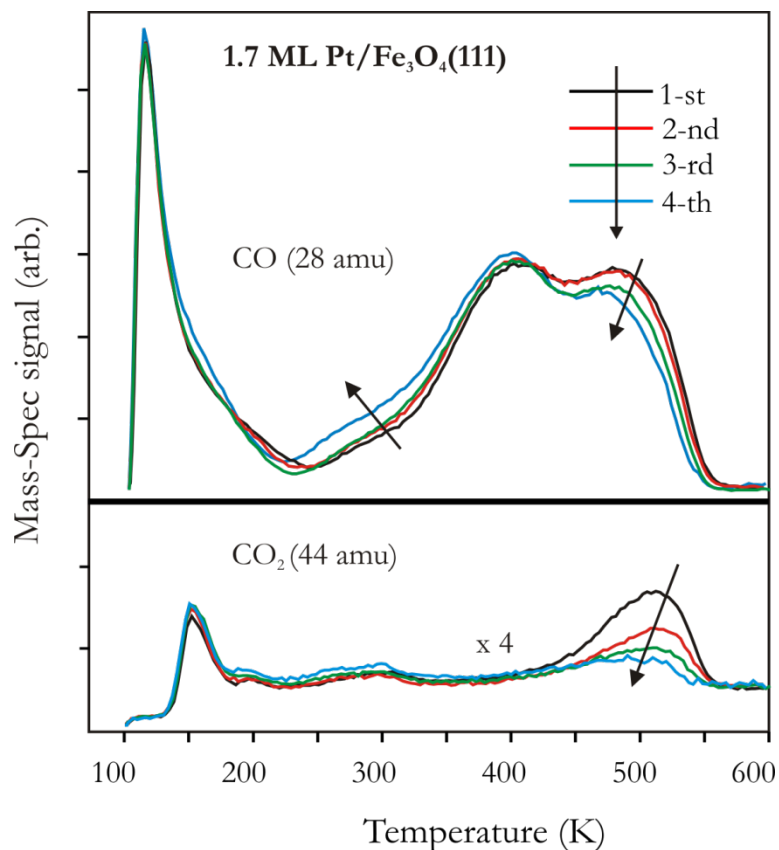


Fig. 5.3 Repeated TPD spectra of 7.5 L CO adsorbed at 100 K on 1.7 ML Pt/Fe₃O₄(111). The 28 (CO) and 44 (CO₂) amu signals are shown.

The most prominent signal at ~ 500 K must be attributed to the reaction limited desorption of CO₂ that forms on the Pt/Fe₃O₄(111) interface. The isotopic experiments with C¹⁸O revealed that the O atoms for this reaction come from the iron oxide film as solely the formation of C¹⁶O¹⁸O was observed on the Pt/Fe₃¹⁶O₄(111) surface as shown in Fig. 5.4. Since CO on the (111) facets desorbs at much lower temperatures, CO₂ can only be formed from CO more strongly bound to the sites that are interfacial in nature. This finding further supports the conclusion that the 270 K state cannot be assigned to the metal/oxide interface. In addition, the results show that CO on the interface sites desorbs at the same temperature (i.e., 480 K) as for other low-coordination sites such as edges and corners.

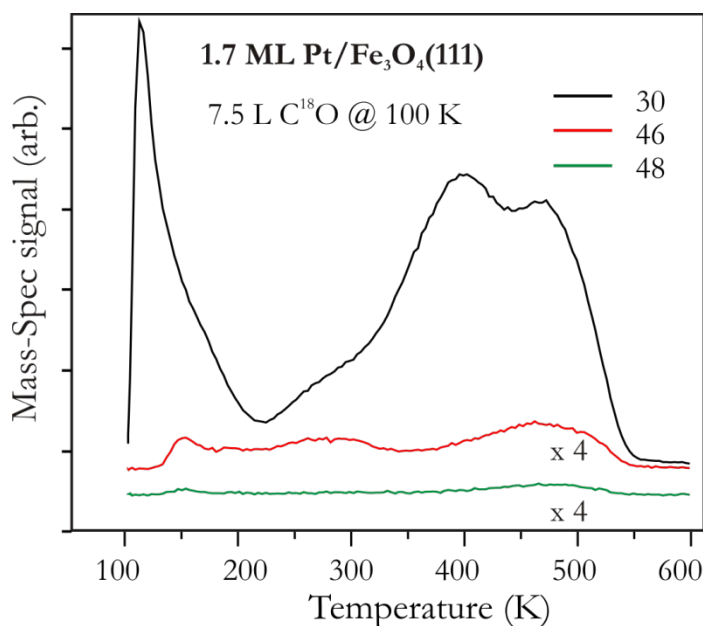


Fig. 5.4 TPD spectra of 7.5 L C¹⁸O adsorbed at 100 K on Pt/Fe₃¹⁶O₄(111) surface. The 30 (C¹⁸O), 46 (C¹⁶O¹⁸O) and 48 (C¹⁸O¹⁸O) amu signals are shown. The heating rate is 3 Ks⁻¹.

Fig. 5.3 shows that the CO₂ production at 500 K gradually decreases in repeated CO TPD runs, indicating that oxygen reacted with CO cannot be replenished under these conditions. Interestingly, the high temperature CO peak also loses intensity. In fact, the CO capacity for this state is reduced even more if one takes into account the amounts of CO that is not desorbed, but consumed to form CO₂ in the previous runs. In principle, this effect could be explained by CO-induced surface restructuring (note, that the surface has been annealed for 5 min at 600 K in UHV prior to TPD studies), site blocking by carbon deposition through CO dissociation (note, however, that the above isotopic experiments showed the Boudouard reaction ($2C^{18}O \rightarrow C^{18}O_2 + C$) to be unfavorable), or both. The effects are expected to manifest themselves more strongly at high CO exposures.

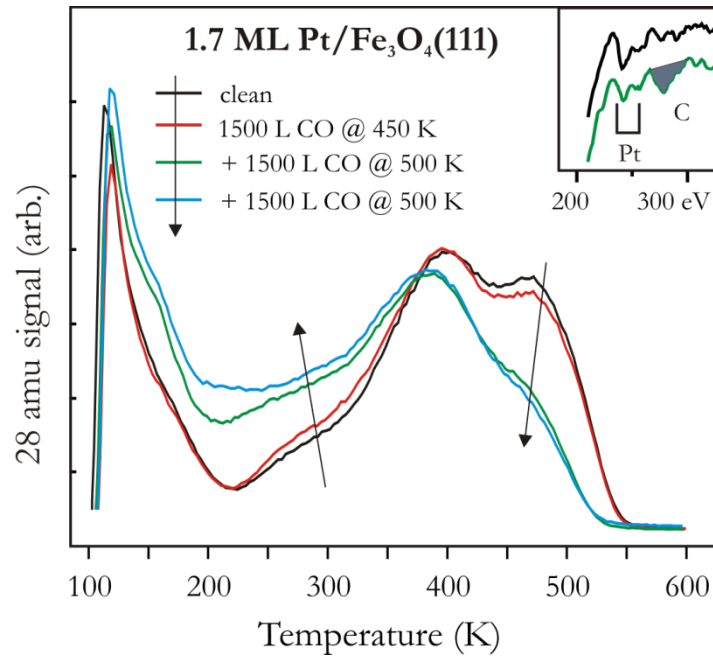


Fig. 5.5 TPD spectra of 7.5 L CO on Pt/ $\text{Fe}_3\text{O}_4(111)$ surface. The sample was treated with 1500 L of CO at 450 K and 500 K. The heating rate is 3 Ks^{-1} . The insets show corresponding AES spectra (in the same color code). Formation of carbon upon exposure at 500 K is observed.

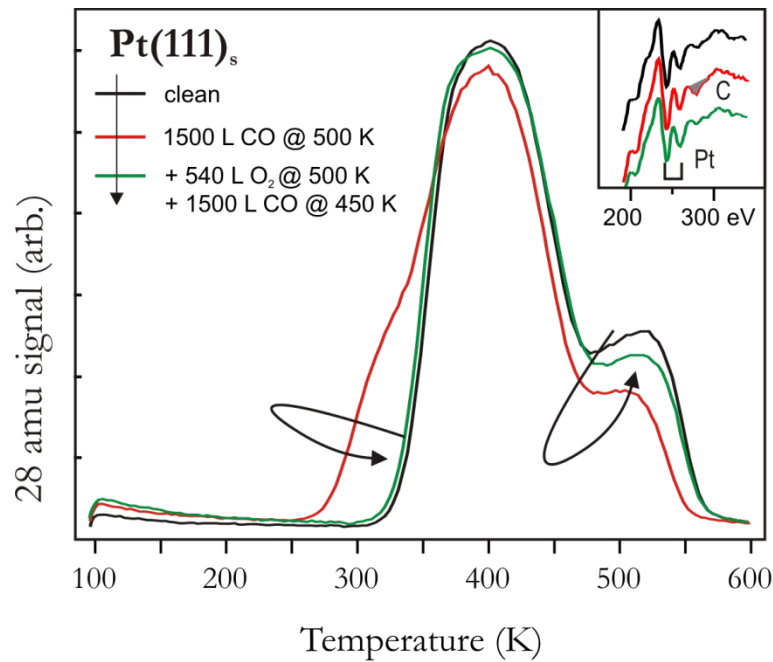


Fig. 5.6 TPD spectra of 7.5 L CO on stepped Pt(111)_s surface. The sample was treated with 1500 L of CO at 500 K. Subsequently, the sample was exposed to 540 L O₂ at 500 K and 1500 L CO at 450 K. The heating rate is 3 Ks^{-1} . The insets show corresponding AES spectra (in the same color code). Formation of carbon upon exposure at 500 K is observed.

Fig. 5.5 shows CO TPD spectra for 1.7 ML Pt/Fe₃O₄ pre-exposed to 1500 L CO ($\sim 10^{-6}$ mbar, 30 min) first at 450 and then at 500 K. It is clear that CO exposure at 450 K essentially causes no change, whereas the exposure at 500 K (i) strongly reduces CO desorption from the high temperature state (i.e., 480 K); (ii) does not appreciably change CO capacity on Pt(111) terrace sites (at ~ 400 K); and (iii) increases the signal at 100 - 300 K overlapping with the signal from the support. Very similar results are observed for highly stepped Pt(111) as shown in Fig. 5.6. Also for the 0.1 ML Fe/Pt(111)_s surface, the CO exposure at 500 K further reduces the signal at ~ 500 K and increases the intensity of the low-temperature shoulder (see Fig. 5.7). AES analysis revealed carbon formation after CO treatment at 500 K (see the insets). Meanwhile, the same treatment, applied to the perfect Pt(111) surface, showed no carbon signal in Auger spectra and no changes in CO TPD (shown in Fig. 5.8).

Therefore, the results suggest that it is not the Fe-Pt intermixing within the supported Pt particles that is responsible for the CO dissociation at 500 K. In fact, the effect on Fe/Pt(111)_s is less pronounced than on the clean Pt(111)_s surface (cf Fig. 5.7 and Fig. 5.8), most likely due to Fe decorating the low-coordinated Pt surface atoms on which CO dissociation occurs. Indeed, both at 450 and 500 K, the (111) terraces are virtually clean in the 10^{-6} mbar CO pressure used in these experiments, while CO has sufficient residence time on the low coordination sites to dissociate before desorption. Apparently, the activation energy for CO dissociation is comparable with CO desorption energy on these sites, i.e. about 130 kJ/mol calculated using the Redhead formula (see chapter 2) and a frequency pre-factor 10^{13} s⁻¹. The carbon left by CO dissociation accumulates on the Pt low-coordinated sites and thus suppresses CO desorption from the high temperature state, i.e. at 480 – 500 K.

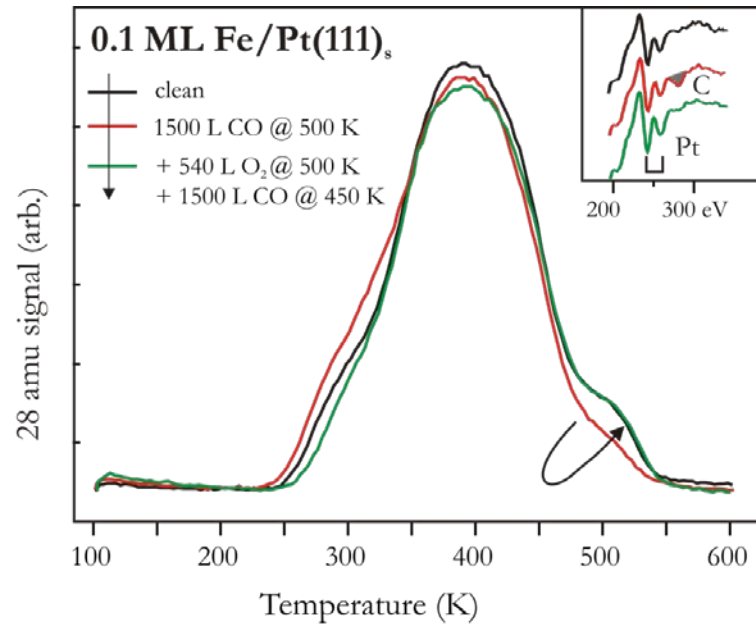


Fig. 5.7 TPD spectra of 7.5 L CO on 0.1 ML Fe/Pt(111)_s surface. The sample was treated with 1500 L of CO at 500 K. Subsequently, the sample was exposed to 540 L O₂ at 500 K and 1500 L CO at 450 K. The heating rate is 3 Ks⁻¹. The insets show corresponding AES spectra (in the same color code). Formation of carbon upon exposure at 500 K is observed.

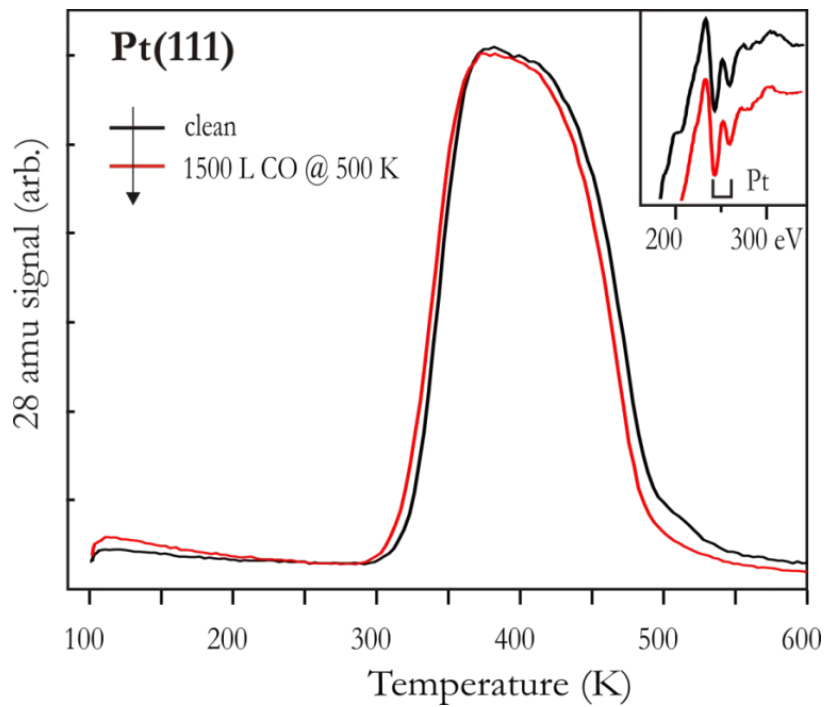


Fig. 5.8 TPD spectra of 7.5 L CO on clean Pt(111) surface. The sample was treated with 1500 L of CO at 500 K. The heating rate is 3 Ks⁻¹. The insets show corresponding AES spectra (in the same color code). Formation of carbon upon exposure at 500 K is observed.

In order to determine whether CO dissociation depends on the Pt particle size, the experiments were performed for different Pt coverages as shown in Fig. 5.9. For all samples, high CO exposure at 500 K resulted in carbon deposition as shown in the AES spectra presented in the insets. Concomitantly, the 480 K peak is strongly reduced, in particular for the highest Pt coverage studied, while a broad desorption signal at temperatures below 300 K gains intensity and overlaps with the signal of the bare support. (Note that the same exposure to pure Fe₃O₄(111) films did not result in new CO desorption states and carbon deposition).

The results, presented in Fig. 5.6, Fig. 5.8 and Fig. 5.9, show that the CO capacity for the (111) terrace sites is least affected by carbon deposition (as more clearly observed on the stepped Pt(111)_s surface). Therefore, it is plausible that carbon blocks the low-coordinated Pt sites and thus weakens CO bonding to the adjacent terrace sites, ultimately resulting in the low-temperature desorption state as a shoulder TPD spectra below 300 K.

The carbon deposits can be removed by reaction with 10⁻⁶ mbar O₂ at 500 K. The chemisorbed oxygen left on the Pt surface is in turn removed by CO at 450 K, i.e., at the temperature when no CO dissociation occurs (see Fig. 5.5). This procedure is similar to that previously used for the Pd/Al₂O₃/NiAl(110) system [182, 203], and practically recovers the original CO TPD spectra and cleanliness of the Pt surfaces as judged by AES (see Fig. 5.9). Another interesting finding is that the shoulder in the TPD spectra range from 250 K-300 K returns back after removing carbon deposits (see Fig. 5.9). Similar changes are observed on highly stepped Pt(111)_s, as well as on the 0.1 ML Fe/Pt(111)_s surface as shown in Fig. 5.7 and Fig. 5.8. These results suggest that carbon deposits modify CO adsorption properties in a similar way as Fe migration on to Pt particles upon UHV annealing at 600 K.

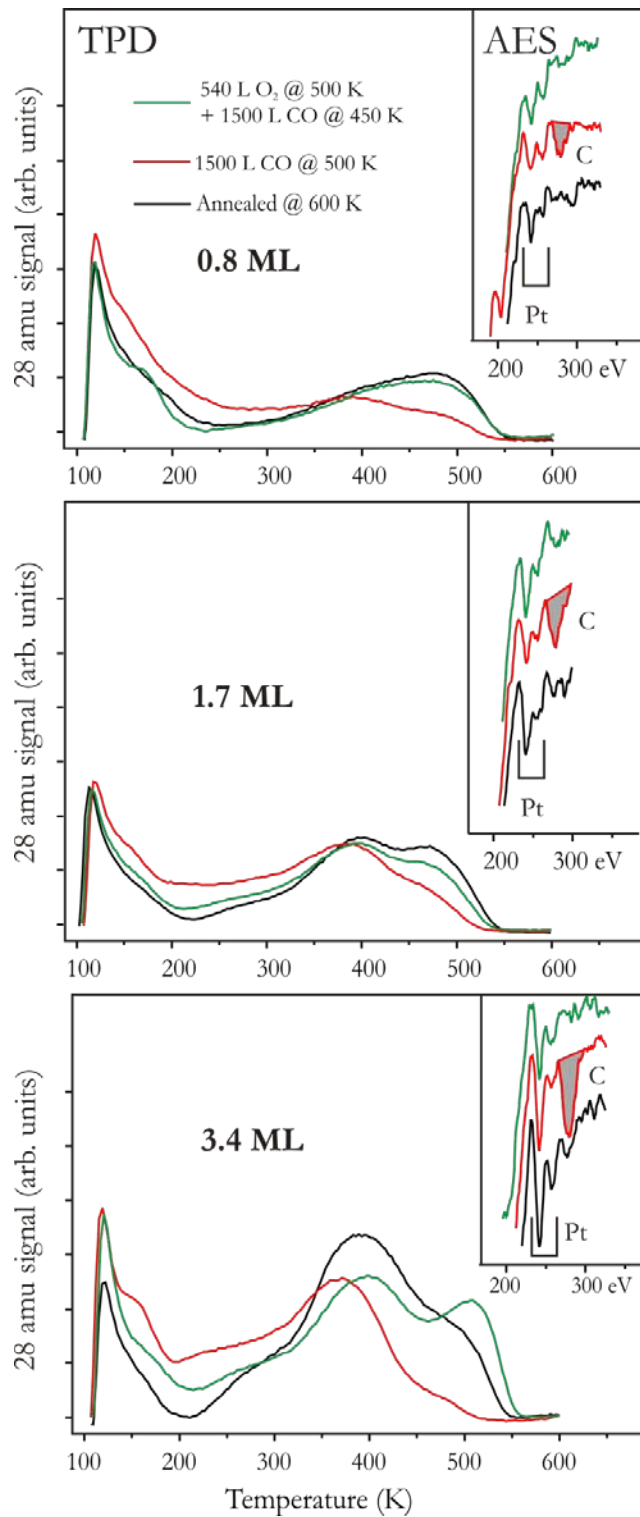


Fig. 5.9 TPD spectra of CO on Pt/Fe₃O₄(111) annealed at 600 K for 5 min as a function of Pt coverage as indicated. Then each sample was treated with 1500 L of CO at 500 K. Subsequently, the sample was exposed to 540 L O₂ at 500 K and 1500 L CO at 450 K. 7.5 L of CO were dosed at 100 K in each case. Heating rate is 3 Ksec⁻¹. The corresponding AES spectra are shown in the insets in the same color code.

In conclusions, both on Pt/Fe₃O₄(111) and stepped Pt(111)_s surfaces CO is found to dissociate at 500 K resulting in deposition of carbon, supporting the previous literature results on the key role of low-coordinated sites in CO dissociation on Pt. The results also suggest that carbon accumulation occurs on the low-coordinated Pt sites. Carbon deposits can be removed by mild oxidation at 500 K.

5.4. SMSI Effect

When supported on reducible transition metal oxides, Pt particles often exhibit SMSI effect, resulting in a dramatic decrease of CO and H₂ uptake. SMSI has attracted much attention since its first report by Tauster et al. in 1978 [65], because it shows important differences in the catalytic activity and selectivity of hydrogenation reaction when reduced at high temperature (typically, above 700 K). Since encapsulation always results in the formation of thin oxide layers on top of the metal particles, it is reasonably expected that encapsulation leads to suppression of the catalytic reactions occurring on metal surfaces due to the site-blocking effects.

Two major factors contribute to the SMSI states, so-called electronic and geometric factors [60, 61]. The electronic factor is determined by a perturbation of the electronic structure of the metal catalyst. This perturbation originates from an interaction between the cluster and the oxide support, for example, a charge transfer between the metal and the oxide. The geometric factor is due to a physical covering of metal particles by a thin layer of reduced oxide support (encapsulation or decoration model). In general, minimization of surface energy is considered as one of the main driving forces for encapsulation. A variety of experiments in different groups have confirmed the encapsulation of Pt particles by a thin oxide layer on TiO₂(110) and reduced CeO₂(111) [60, 61, 180, 204].

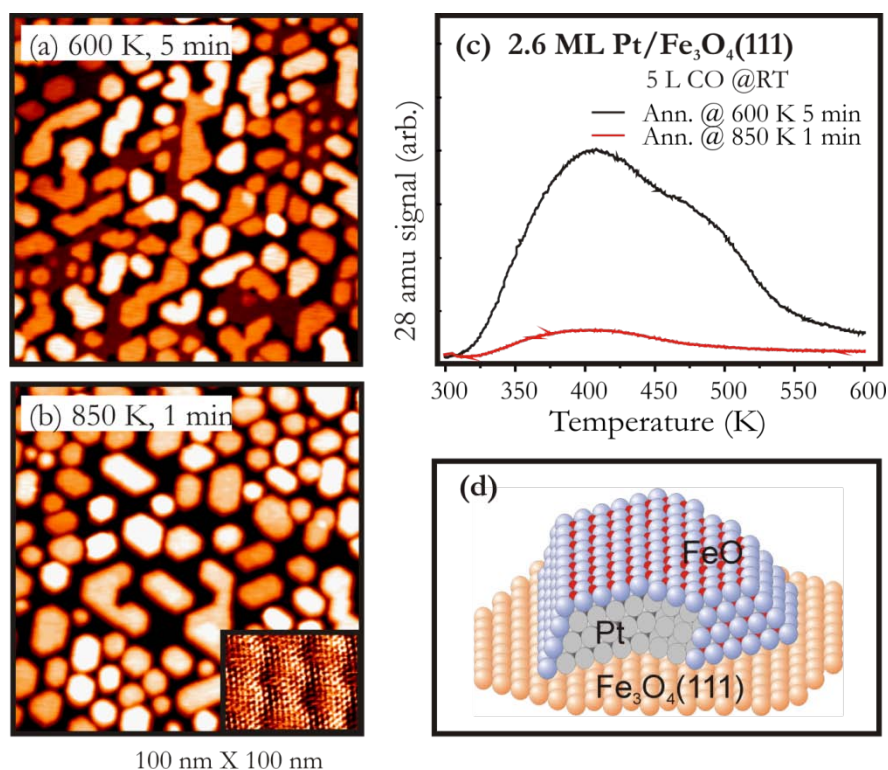


Fig. 5.10 STM images (provided by Z.-H Qin and M. Lewandowski) ($100\text{ nm} \times 100\text{ nm}$) of a 2.6 ML Pt/Fe₃O₄(111) sample as deposited at 300 K and after annealing at 600 K for 5 min (a) and at 850 K for 1 min (b). The inset in (b) (provided by M. Lewandowski) shows a high resolution image presented in the current mode to increase the contrast and to show moiré superstructure with 2.6 nm periodicity observed on the top facets due to the formation of an FeO encapsulating layer; $V = 1.4\text{ V}$, $I = 0.7\text{ nA}$. The CO TPD spectra from these samples are shown in (c) as indicated (provided by Z.-H. Qin and M. Lewandowski). The heating rate is 3 Ks^{-1} . (d) Schematic presentation of Pt particles encapsulated by a FeO(111) layer.

In section 5.3, it has been shown that Fe₃O₄(111) supported Pt nanoparticles annealed at 600 K exhibit a desorption state at $\sim 270\text{ K}$, which is associated with Fe-Pt intermixing. Annealing to even higher temperatures $\sim 850\text{ K}$ resulted in total suppression of CO uptake. The decrease in CO uptake is far beyond that caused by particle sintering as shown in STM images in Fig. 5.10a-b. This is a “classical” manifestation of SMSI. The direct prove of the Pt particles encapsulation came from the high resolution STM study as shown in the inset in Fig. 5.10b. The top facets of the largest encapsulated particles exhibit the hexagonal lattice of protrusion with a $\sim 3\text{ \AA}$ periodicity, in turn forming the superstructure with 25 \AA periodicity which is very similar to FeO (111) films grown on Pt(111) as shown in chapter 2. Therefore it is concluded that Pt particles are encapsulated by a FeO(111) like layer at high temperatures as schematically shown in Fig. 5.10d.

Interestingly, the encapsulation of Pt particles supported on $\text{Fe}_3\text{O}_4(111)$ is found to be a coverage dependent process as shown in Fig. 5.11. At high Pt coverage, CO adsorption capacity drops almost to zero upon annealing at 850 K, whereas at lower coverages, the effect is less pronounced. CO uptake: the ratios before and after annealing are 0.2 and 0.3 for 1.6 ML and 0.8 ML Pt coverage, respectively. This effect can be rationalized on the basis of results shown in section 5.2. Firstly, the 270 K desorption state on Pt/ $\text{Fe}_3\text{O}_4(111)$ scales with Pt coverage, and is assigned to the initial stage of SMSI via intermixing. This feature cannot be associated with the metal/oxide interfacial sites, which otherwise should have more pronounced effect at low Pt coverage. It seems that the initial Fe-Pt intermixing step is important and essential for the subsequent encapsulation process at higher temperatures. Secondly, the size of Pt particles on $\text{Fe}_3\text{O}_4(111)$ after annealing at 600 K increases with increasing coverage. The large, well faceted particles expose the (111) facets on top. We may speculate that the activation energy of encapsulation is related to the surface structure of the facets, and the lowest for (111), which dominates for large particles. Small particles formed at low Pt coverage exhibit ill-defined shape, and as such showed less pronounced CO uptake drop (see Fig. 5.11). However, further studies remain to be done to elucidate the encapsulation mechanism on Pt/ Fe_3O_4 .

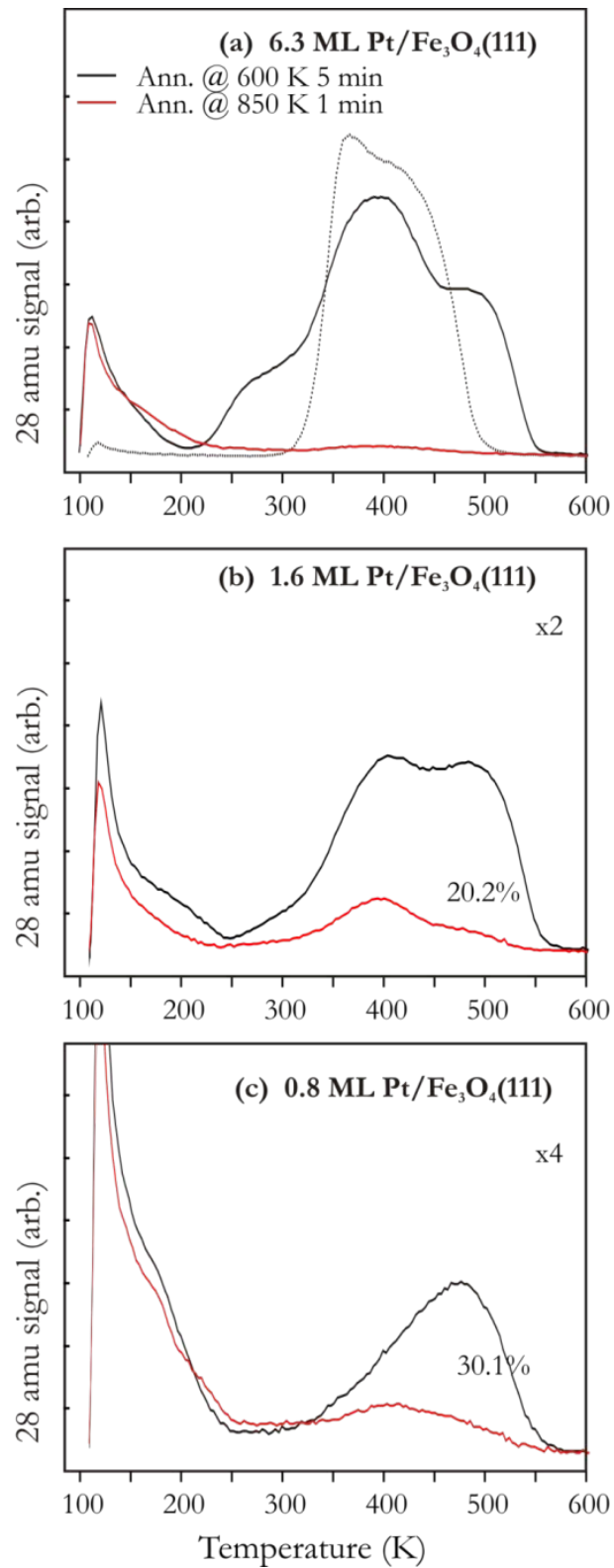


Fig. 5.11 TPD spectra of 7.5 L of CO adsorbed at 100 K on Pt/Fe₃O₄(111) annealed at 600 K for 5 min (in black) and 850 K for 1 min (in red) as a function of Pt coverage as indicated. TPD spectrum of 7.5 L of CO adsorbed at 100 K on clean Pt(111) is shown in dashed line for comparison. Heating rate is 3 Ks⁻¹.

5.5. CO Oxidation on Pt/Fe₃O₄(111).

In the previous section it has been shown that Pt particles supported on Fe₃O₄(111) films are encapsulated by an iron oxide film which is structurally very similar to FeO(111)/Pt(111). Now we extend the reactivity studies on ultrathin FeO(111) films on Pt(111) to the Pt nanoparticles supported on Fe₃O₄. In the following we will refer to Pt annealed to 850 K as an “encapsulated” system to discriminate from a “clean” Pt/Fe₃O₄ annealed to 600 K, although in the latter case partial Fe-Pt intermixing is observed as the initial stage of the encapsulation as shown in section 5.2.

Model Pt/Fe₃O₄ catalysts were examined in the CO oxidation reaction at the stoichiometric ratio (40 mbar CO + 20 mbar O₂, He balance) and under O-rich conditions (10 mbar CO + 50 mbar O₂). Fig. 5.12 shows kinetic curves of CO₂ production at 450 K on clean (solid symbols) and encapsulated (open symbols) Pt particles at two coverages (1.6 and 6.3 ML). The results for pristine Fe₃O₄(111) films under the same conditions are also shown, for comparison.

Fig. 5.12 shows that activity of the Pt/Fe₃O₄ catalysts increases with increasing Pt coverage. In addition, the average reaction rate increases, by a factor of ~2, upon increasing oxygen pressure from 20 to 50 mbar, in fair agreement with the reaction order for O₂ (0.85) measured on a Pt(111) single crystal under the same experimental conditions. Note, however, that in the O-rich ambient reactivity of the Fe₃O₄(111) support is greatly enhanced and becomes comparable with the Pt particles formed at low coverage. This finding suggests a positive reaction order for O₂, at variance with the zero-order observed on the powdered Fe₂O₃ catalysts, although at much higher temperatures (520 – 570 K) than used here (450 K) [163, 165]. The discrepancy may also be related to the different red-ox properties of magnetite (Fe₃O₄) and hematite (Fe₂O₃) surfaces.

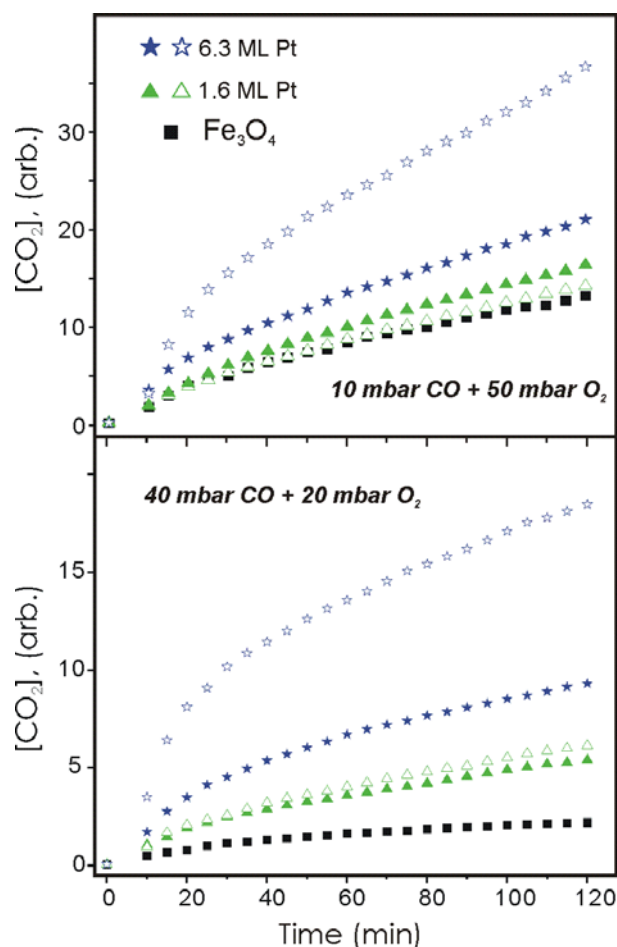


Fig. 5.12 CO₂ production as a function of time measured on Pt/Fe₃O₄(111) at Pt coverages and CO+O₂ partial pressures as indicated. The catalysts were annealed at 600 K (solid symbols) and 850 K (open symbols) prior to reaction. The results for pristine Fe₃O₄(111) films under the same conditions are shown for comparison. Time zero corresponds to the start of heating with a rate 1 Ksec⁻¹ to the reaction temperature, 450 K.

However, the most intriguing result revealed in these experiments is the higher reactivity of the encapsulated Pt particles than of their clean counterparts. This effect is clearly observed for the high Pt coverage at both CO:O₂ ratios studied. At the low Pt coverage, the catalysts showed comparable activities. However, when normalized to the CO uptake as a measure of the total Pt surface area (which is much lower in the case of encapsulation), the reactivity of the encapsulated particles is remarkably higher at the low Pt coverage, too. The rate enhancement can tentatively be linked to the presence of the FeO(111) film covering Pt particles which greatly promotes CO oxidation when grown on a Pt(111) single crystal as shown in Chapter 3.

Reactivity of FeO/Pt(111) in PROX

PROX reaction is an important process to purify H_2 for use in polymer electrolyte fuel cells [205]. H_2 produced from gasoline or natural gas contains some amounts of CO. The concentration of CO in the hydrogen feed must be kept below 100 ppm to avoid the catalyst's poisoning by CO. Therefore, the desired reaction in PROX is ($2CO + O_2 \rightarrow 2CO_2$), while the reaction ($2H_2 + O_2 \rightarrow 2H_2O$) is undesired.

Supported Pt catalysts have been used for PROX reaction, showing promising performance (see e.g. [206-211]). Recently the promotional effect of the iron oxide layer on Pt catalysts has been reported, exhibiting both higher reactivity and selectivity in PROX reaction [212-215]. For example, Liu et al. [213] have found the enhanced performance of the iron oxide on Pt/ γ -alumina catalyst by a combination of electron microscopic and spectroscopic techniques. They proposed a noncompetitive dual site adsorption mechanism, with the adsorption of CO on Pt sites and the supply of O from iron oxide at the interface of Pt-iron oxide. Tanaka et al. [215] also found the marked enhancement of PROX reactivity by deposition of a large quantity of FeO_x on Pt catalysts. However, as the authors highlighted, the role of FeO_x is still a big puzzle. They suggested that one vital role of FeO_x is the formation of bridged CO adsorption sites, which may be Pt-Fe sites, leading to the decrease of the CO adsorption energy and the increase of the O population. Indeed Pt-Fe catalysts have been reported to have high activity and selectivity for PROX reaction. Watanabe et al. [212] proposed new Pt-Fe/mordenite catalysts for the PROX, which is superior to conventional Pt/ Al_2O_3 catalysts, and Pt/mordenite. Based on their reactivity data, they proposed the so-called "bifunctional mechanism" for the distinctive performance at Pt-Fe catalysts, where the Pt sites acts as a CO adsorption site and the Fe site acts as an O_2 dissociative-adsorption site and enhances the surface reaction between the reactants on the neighboring sites. Sirijaruphan et al. [216] confirmed the Fe

promotional effect on PROX reaction on Pt/ γ -Al₂O₃ by using isotopic transient kinetic analysis (ITKA). However the PtFe catalyst deactivated rapidly most probably due to the oxidation of Fe, leading to the loss of the active intrinsic sites.

The presence of H₂ have been found to show positive effect on CO oxidation. The understanding of the promotional effect of H₂ is still limited. First, H₂ as a reductive agent could contribute to the change of the oxidation states of Fe species, and hence change the reactivity. Liu et al. [217], for the first time, provided strong evidence that the Fe²⁺ species in their Fe-Ir catalysts play a key role in the PROX reaction. On the other hand, some authors explained the H₂ influence on the reaction in terms of the formation of hydroxyl groups on the oxide support, either giving a water-gas shift reaction ($CO + H_2O \rightarrow CO_2 + H_2$) pathway in addition to CO oxidation [217, 218], or promoting the decomposition of reaction intermediates (carbonate or formate) which are formed in the presence of hydroxyl [219-223].

In order to address the promotional role of iron oxide on Pt catalysts in PROX reaction, we have employed combined GC, TPD, AES and LEED to investigate the reactivity and selectivity of the reaction on FeO(111)/Pt(111) model system. For comparison the PROX reaction has also been studied on Fe/Pt(111) catalysts. Furthermore, the influence of H₂ on CO oxidation has been investigated.

6.1. Reactivity and Selectivity

The catalytic performance of Pt(111) and FeO(111)/Pt(111) catalysts in CO oxidation reaction in the presence of 500 mbar H₂ is shown in Fig. 6.1. For comparison, the reaction in the absence of H₂ under the same conditions is shown in black curves. Upon slow heating of the Pt(111) single crystal and the FeO(111) film, CO₂ evolution is clearly observed at temperatures above 400 K for FeO and 430 K for Pt(111) catalyst. The reaction rate apparently increases with increasing temperature. FeO films exhibit higher reactivity than that of Pt(111) substrates, similar to what has been observed in CO oxidation reaction as shown here and in Chapter 3. The presence of H₂ greatly enhances the activity of both catalysts.

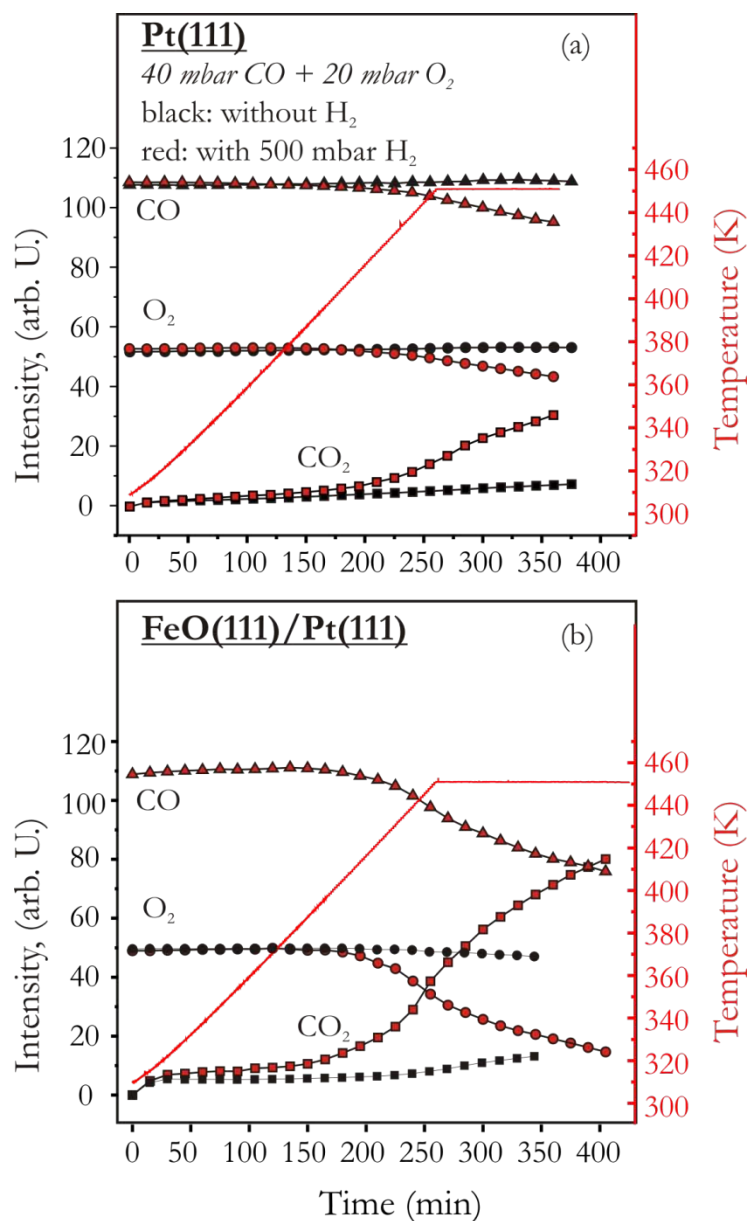


Fig. 6.1 Temperature-programmed reaction profile of CO₂ production, CO and O₂ consumption over Pt(111) (a) and FeO(111)/Pt(111) (b) on slow heating (1 Kmin⁻¹) in 40 mbar CO + 20 mbar O₂ + 500 mbar H₂ balanced by He to 1 bar. The reaction profile under the same conditions in the absence of H₂ is shown in black for comparison.

In order to mimic the conditions used in commercial PROX process, trace amounts of CO are used in the reaction. The selectivity of PROX reaction (for desired CO₂ formation) is an important factor to evaluate the performance of PROX catalysts, where the CO selectivity is defined as the moles of CO converted to CO₂ divided by the total moles of O₂ reacted:

$$\text{selectivity} = \frac{\frac{1}{2} [\text{moles of CO converted to CO}_2]}{\text{total moles of O}_2 \text{ reacted}}$$

$$= \frac{\frac{1}{2} \text{CO conversion} \times [\text{CO}]}{\text{O}_2 \text{ conversion}}$$

Tab. 6.1 CO and O₂ conversion and O₂ selectivity towards CO₂ formation over FeO(111)/Pt(111) as a function of O₂ pressure in the mixture with 500 mbar H₂ and 1 mbar CO after 30 min of the reaction (upper) or 10 mbar CO after 60 min of the reaction (bottom), balance by He. The reaction temperature is 450 K.

1 mbar CO (after 30 min)

PO ₂	Conversion		Selectivity
	CO	O ₂	
1.5 mbar	47%	100%	16%
3 mbar	95%	100%	16%
4 mbar	100%	100%	12%

10 mbar CO (after 60 min)

PO ₂	Conversion		Selectivity
	CO	O ₂	
5 mbar	20%	97%	22%
10 mbar	31%	90%	20%
20 mbar	65%	84%	23%

The stoichiometric condition is enough for the CO oxidation alone, but excess O₂ is needed for high conversion of CO due to the consumption of O₂ in the H₂ oxidation. Hence, the CO selectivity was studied under excess of O₂. Fig. 6.2 and Fig. 6.3 show a series of reactivity studies as a function of O₂ partial pressure in the presence of CO (1 mbar and 10 mbar) and 500 mbar H₂ at 450 K. The results are summarized in Tab. 6.1.

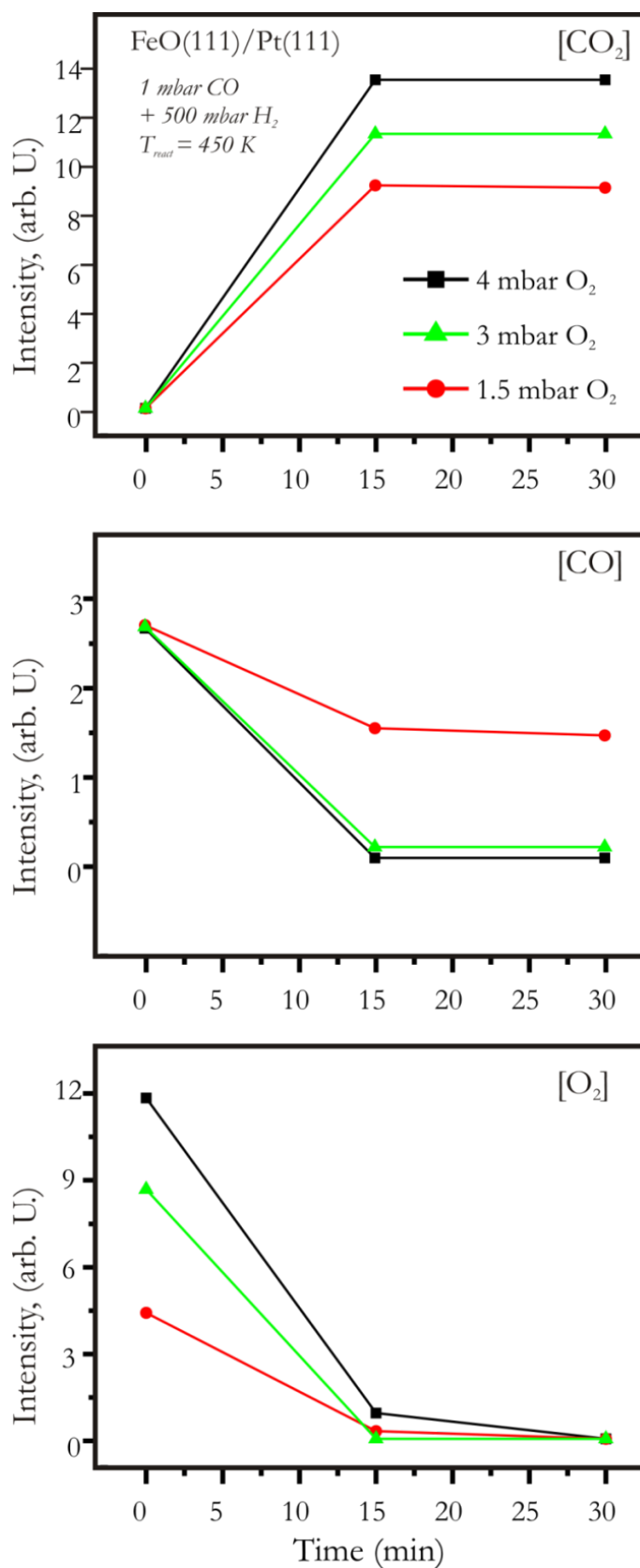


Fig. 6.2 Kinetics of CO₂ production, CO and O₂ consumption over FeO(111)/Pt(111) as a function of O₂ pressure in the mixture with 500 mbar H₂ and 1 mbar CO, balance by He. The reaction temperature is 450 K.

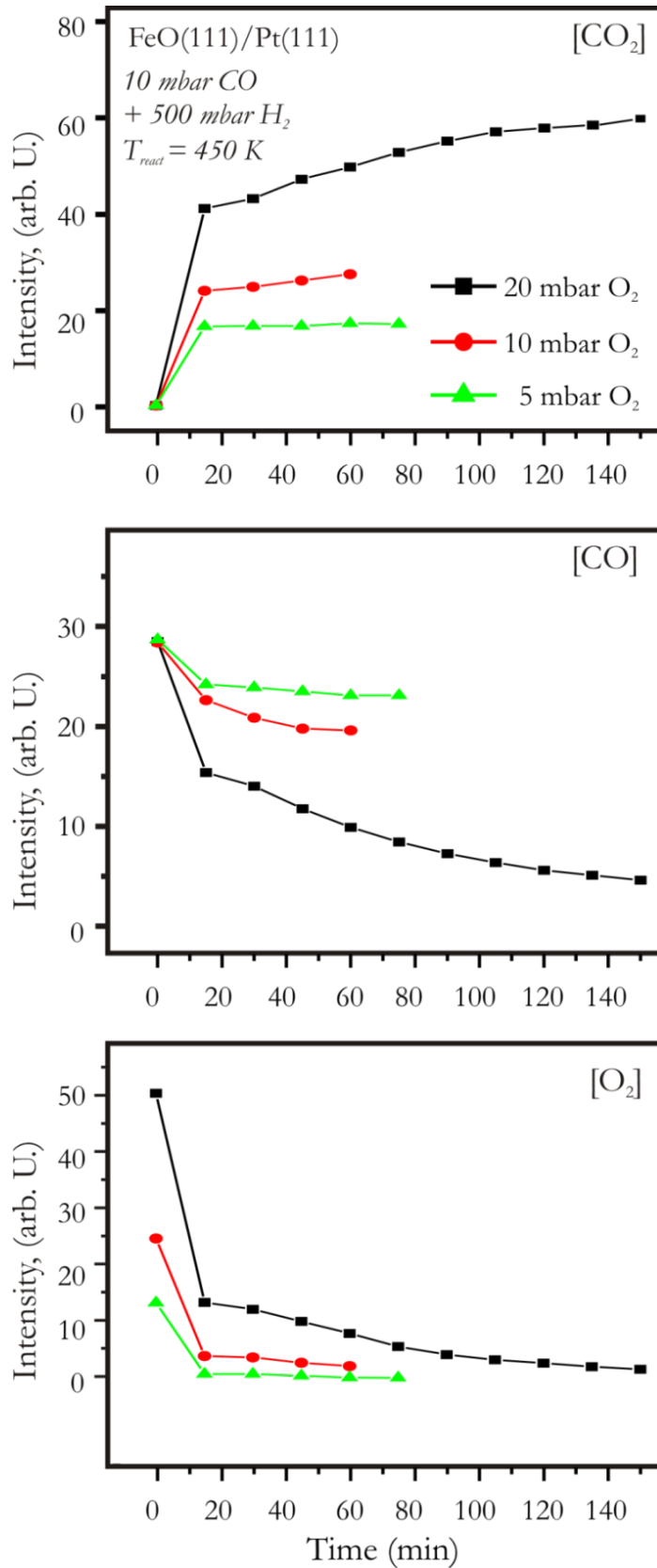


Fig. 6.3 Kinetics of CO₂ production, CO and O₂ consumption over FeO(111)/Pt(111) as a function of O₂ pressure in the mixture with 500 mbar H₂ and 10 mbar CO, balance by He. The reaction temperature is 450 K.

In the first set of the experiments where the pressure of CO was kept at 1 mbar, after 30 min of reactions at 450 K, the O₂ conversions were 100% at all three O₂ pressures studied. As the pressure of O₂ increases, the CO conversion increased significantly from 47% to 100 %, with the slight decrease of the selectivity from 16 % to 12 %. In the second set of the experiments where the pressure of CO was kept at 10 mbar, after 60 min of reactions at 450 K, with the increasing O₂ pressure, the conversion of O₂ decreases from 97 % to 84 %, while CO conversion increases. The selectivity was kept stable around 20-22 %.

The temperature dependence of the reaction has also been studied. Fig. 6.4 displays the kinetics of the CO₂ formation at 430 K and 450 K in the presence of 10 mbar CO, 20 mbar O₂ and 500 mbar H₂. After 30 min of reactions, the conversion of CO and O₂ dropped remarkably with increasing temperature, whereas the selectivity with respect to CO oxidation increased only slightly (see Tab. 6.2). One interesting finding is that abrupt O₂ consumption after 180 min of the reaction coincides with the total consumption of CO as shown in Fig. 6.4. This result indicates that oxygen primarily reacts with CO than H₂ at the beginning of the reaction.

Our results clearly show that the FeO/Pt catalyst is active under PROX conditions, and comparable with 1% Pt/CeO₂ catalysts [224], showing that at 1:1 CO:O₂ ratio, the CO conversion is ~60%, and the selectivity is 30%.

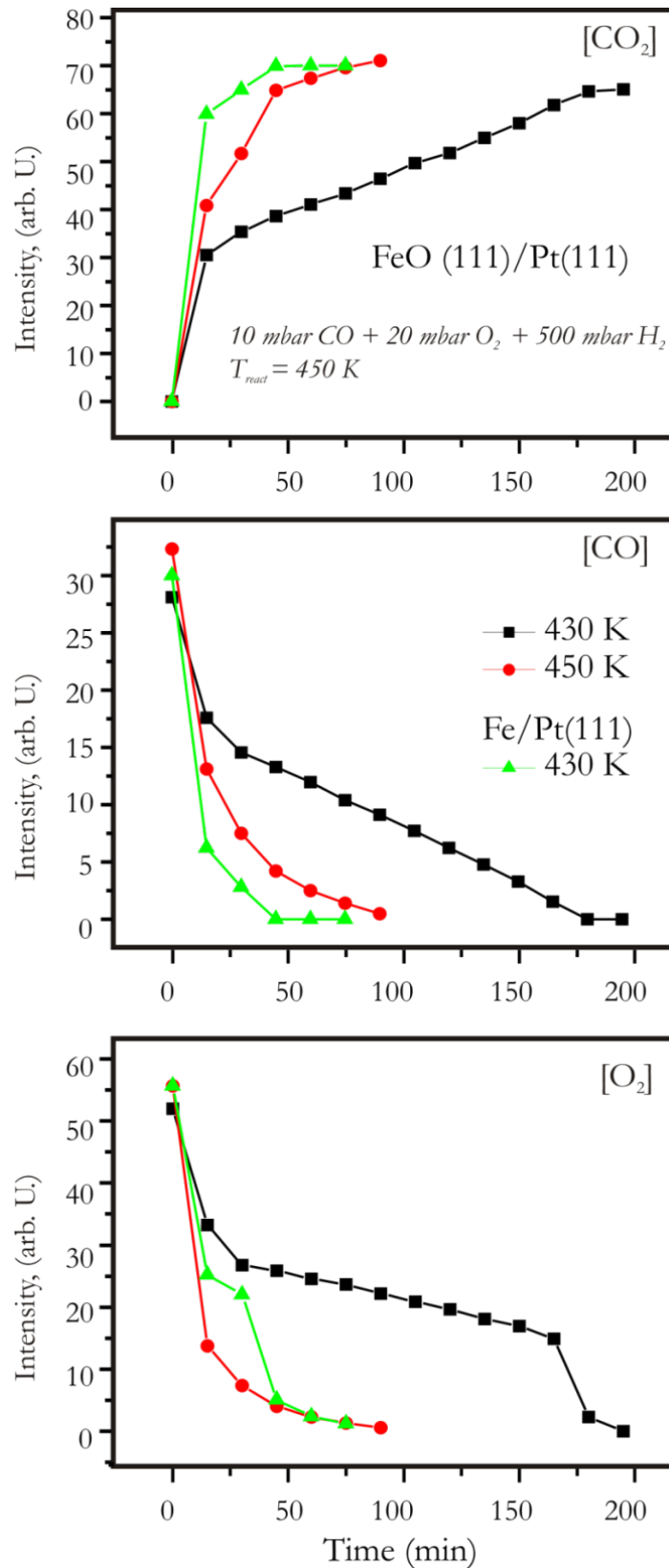


Fig. 6.4 Kinetics of CO₂ production, CO and O₂ consumption over FeO(111)/Pt(111) as a function of temperatures in the mixture with 10 mbar CO, 20 mbar O₂ and 500 mbar H₂ balance by He. Kinetics over Fe/Pt(111) surface at 430 K under the same conditions are also shown.

Tab. 6.2 CO and O₂ conversion and O₂ selectivity towards CO₂ formation over FeO(111)/Pt(111) as a function of temperatures in the mixture with 10 mbar CO, 20 mbar O₂ and 500 mbar H₂ balance by He after 30 min of reaction. Kinetics over Fe/Pt(111) surface at 430 K under the same conditions are also shown.

after 30 min

	Conversion		Selectivity
	CO	O ₂	
FeO(450 K)	77%	87%	22%
FeO (430 K)	48%	48%	25%
FePt (430 K)	91%	61%	37%

6.2. Structural Characterization

The spent FeO/Pt catalysts after the reaction at 450 K in the presence of 10 mbar CO, 20 mbar O₂ and 500 mbar H₂ showed diffuse diffraction spots of Pt(111) (see Fig. 6.5), which indicates that the FeO(111) films undergo strong reconstruction. The AES study of the spent catalysts reveal only small amounts of carbon beyond the Pt, O and Fe elements as shown in Fig. 6.6, which is similar to the results observed on the FeO films after CO oxidation reaction in the absence of H₂. However, using the Auger O:Fe signal ratio of the pristine FeO films as a reference, the iron oxide phase in PROX exhibits a FeO_{0.9} stoichiometry, on average. In addition, subsequent UHV annealing at temperatures above 800 K cannot restore the original LEED pattern and the O:Fe ratio of the original film as it was the case for FeO films in CO+O₂ ambient (see Fig. 6.5).

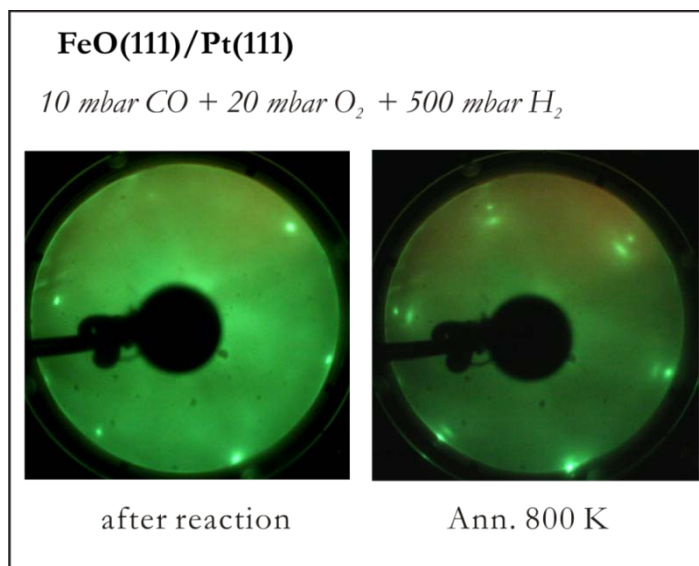


Fig. 6.5 LEED patterns ($E = 60$ eV) of the FeO(111) film after reaction at 450 K (left) in 40 mbar CO + 20 mbar O₂ + 500 mbar H₂ in He and subsequently annealed in vacuum at 800 K (right).

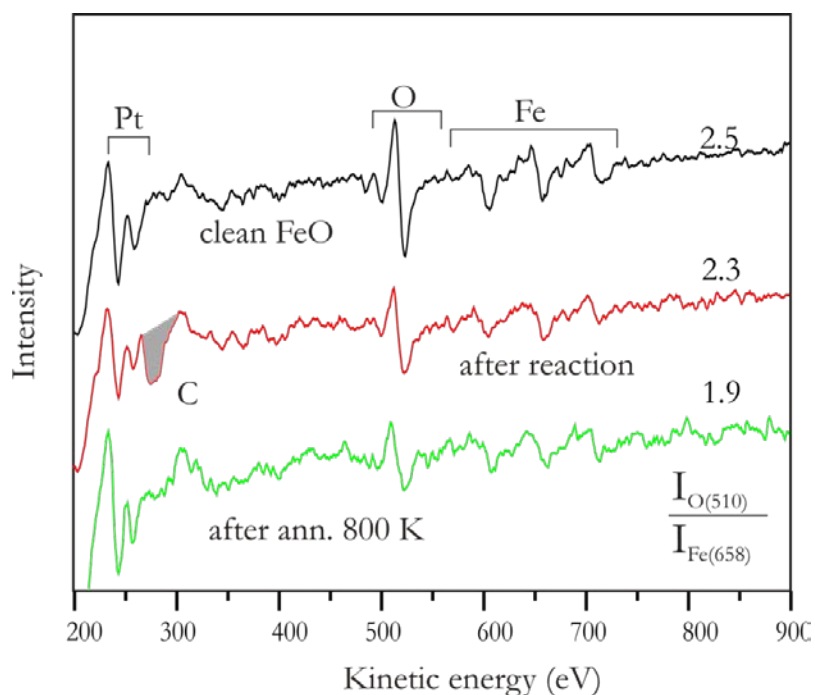


Fig. 6.6 AES spectra of the clean FeO(111) film (top), after the reaction in 40 mbar CO + 20 mbar O₂ + 500 mbar H₂ at 450 K (middle) and subsequent annealing to 800 K for 2 min (bottom). The corresponding peak ratios for O(510 eV) and Fe(658 eV) are indicated.

Further information on the structure of the post-reacted FeO/Pt surfaces was obtained by TPD (see Fig. 6.7). CO, CO₂, H₂, and H₂O were found as desorbing species upon heating of the spent catalysts in UHV. By analogy with the previous assignment in chapter 3, CO desorption signals at 350–500 K is related to CO adsorbing on exposed

Pt(111) substrates. The desorption traces of CO at temperatures above 500 K, may be attributed to the reaction of carbonaceous species with surface oxygen. This oxygen is coming from the iron oxide particles since the carbon peak in AES spectra disappears upon heating to 800 K with a simultaneous further decrease of the Auger O:Fe ratio Fig. 6.6. Annealing to 800 K leads to the low temperature shift of the CO desorption peak with a shoulder at ~ 250 K, which is indicative of the Fe-Pt intermixing as discussed previously in Chapter 5. Upon UHV annealing, there is still CO adsorption characteristic for metallic surfaces, which is in good agreement with the LEED and AES observation. These results differ from those obtained on FeO/Pt after CO oxidation in the absence of H_2 , which shows oxygen enrichment and *reversible* surface reconstruction. Therefore, it is clear that H_2 strongly reconstructs the FeO surfaces.

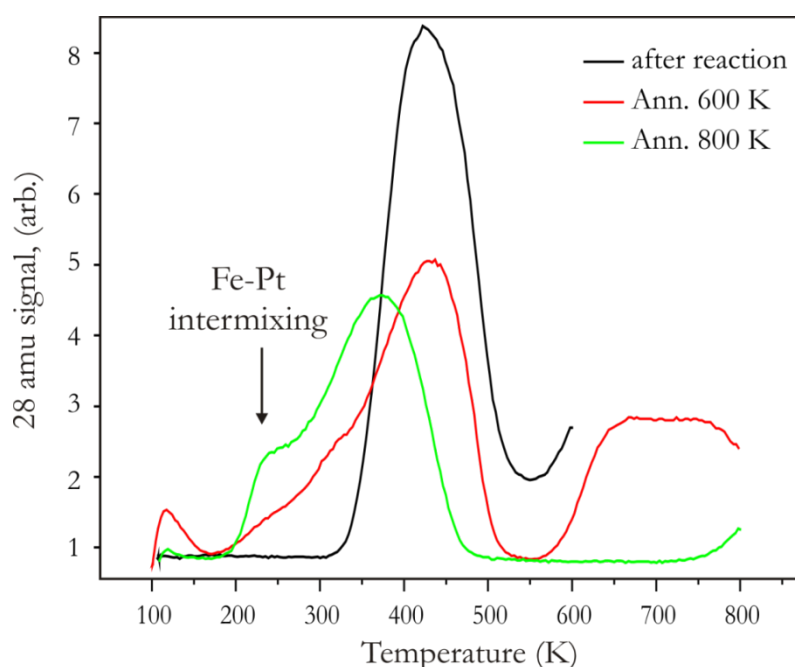


Fig. 6.7 TPD spectra of CO adsorbed at 100 K on the FeO(111)/Pt(111) after reaction (black line) and after step-wise UHV annealing at 600 K (red line) and 800 K (green line).

Note, that at low pressures FeO film is inert towards H_2 . In order to elucidate the role of H_2 on the surface reconstruction, the FeO film was exposed to 500 mbar H_2 at 450 K for 30 min. Fig. 6.8 shows the LEED pattern of the treated sample. The Moiré superstructure of the original FeO(111) film disappeared, instead it exhibited sharp diffraction spots of Pt(111). The AES study of the treated catalysts showed a significant decrease of O content, from FeO to $FeO_{0.5}$, on average (see Fig. 6.9). The TPD study also confirmed the reduction and dewetting of the FeO film, showing CO desorption with a

shoulder at ~ 250 K, which is indicative for the formation of Pt-Fe alloy [194]. In addition, the film cannot be recovered upon UHV annealing. Based on these results, it is suggested that under PROX conditions, the reaction most probably undergoes the reduction of the FeO films, forming Pt-Fe alloy, which then serves as the catalyst in the reaction.

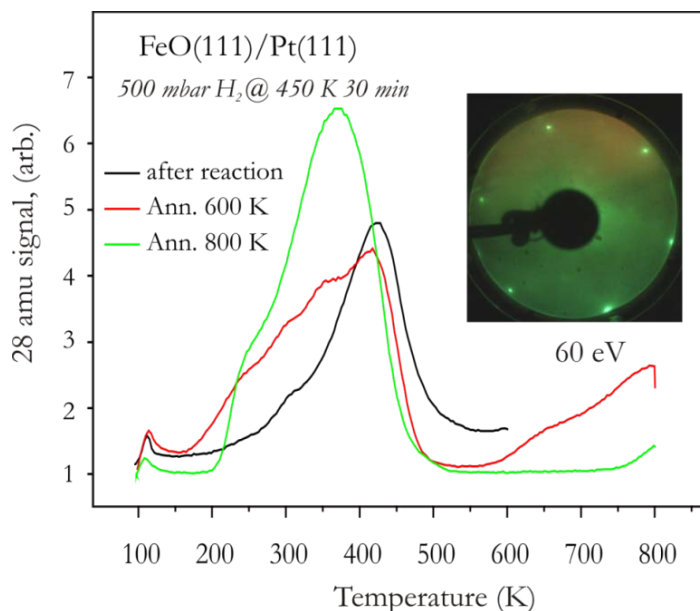


Fig. 6.8 TPD spectra of CO adsorbed at 300 K on FeO(111)/Pt(111) by exposure to 500 mbar H_2 at 450 K (black line) and after step-wise UHV annealing at 600 K (red line) and 800 K (green line).

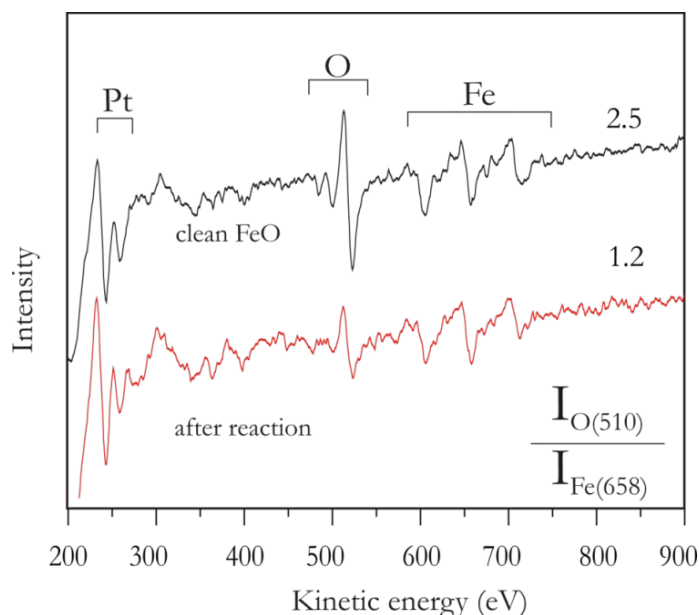


Fig. 6.9 AES spectra of the clean FeO(111) film (top), after the reaction in 500 mbar H_2 at 450 K (bottom). The corresponding peak ratios for O(510 eV) and Fe(658 eV) are indicated.

This conclusion is further supported by the experiments with Fe/Pt(111). The preparation of Fe/Pt(111) surfaces involves physical vapor deposition of 1 ML Fe onto Pt(111) surfaces at RT and subsequent UHV annealing at 450 K for 1 min. The resulted surface showed a low temperature shift of the CO desorption peak, as compared to that of Pt(111) surfaces (see Fig. 6.10), with a broad signal below 300 K, indicative of Fe-Pt intermixing. The results are consistent with those reported by Wadsyama et al. [225]. Their IRAS measurements for CO on Fe/Pt(111) surfaces showed that upon iron deposition, Fe may diffuses into Pt substrates, leading to the formation of an outermost Pt layer. The intensity of CO-Pt band at around 2090 cm^{-1} decreased significantly, and a new absorption band emerged at around 2060 cm^{-1} , which is ascribed to CO adsorption on the outermost Pt layer. The red-shift in peak frequency indicates the weakening of the CO-Pt bond strength.

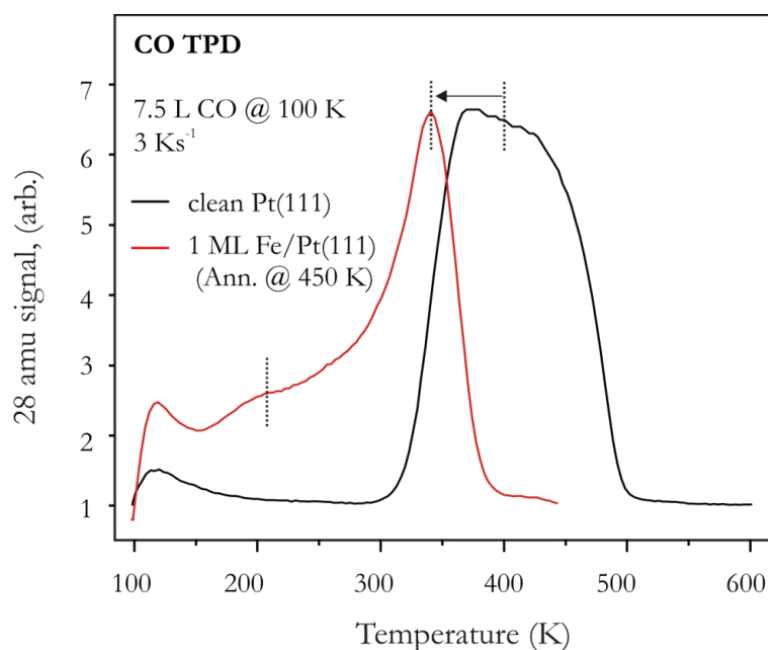


Fig. 6.10 TPD spectra of 7.5 L of CO adsorbed at 100 K on Pt (111) surface and 1 ML Fe precovered Pt(111) sample. Fe/Pt(111) surface was annealed at 450 K for 1 min. The heating rate is 3 Ks^{-1} .

Fig. 6.4 shows CO and O₂ consumption as well as CO₂ formation on Fe/Pt surfaces at 430 K in the mixture of 10 mbar CO, 20 mbar O₂ and 500 mbar H₂. After reaction for 30 min, the Fe/Pt(111) catalyst exhibits 91% CO conversion and 37% selectivity. Therefore, the Fe/Pt(111) catalyst shows in fact higher CO conversion and selectivity than does FeO/Pt(111) (see Tab. 6.2).

This suggests that promotional effect of Fe-oxides on reactivity of Pt catalysts in PROX is most likely explained by formation of Fe-Pt alloy surfaces, where Fe-oxides is the precursor. In the absence of H_2 the reaction over FeO(111) proceeds through formation of O-rich FeO phase. However, in order to see whether H_2 can promote CO oxidation, we have studied $CO+O_2$ reaction by adding small amounts of H_2 into the $CO+O_2$ mixture.

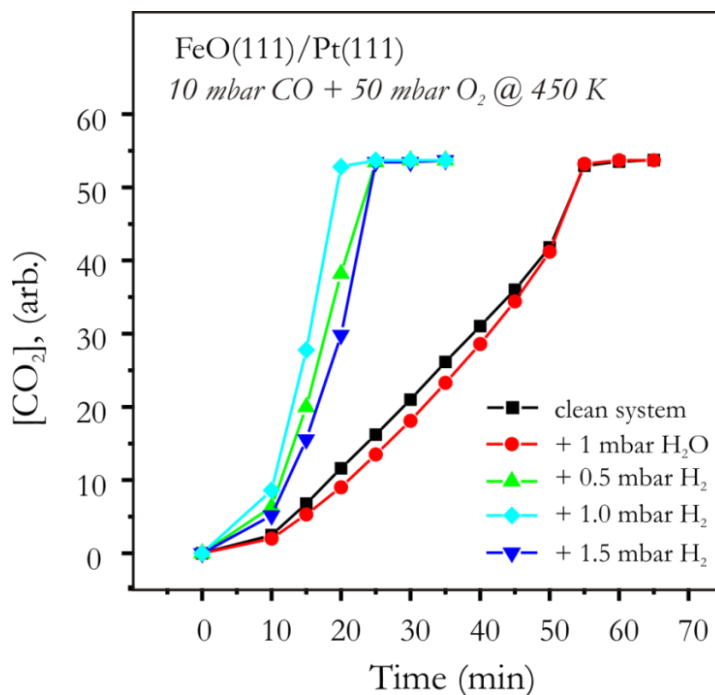


Fig. 6.11 Kinetics of CO_2 production at 450 K over FeO(111)/Pt(111) as a function of H_2 pressure in the mixture with 10 mbar of CO and 50 mbar of O_2 , balanced by He. The reaction data in the absence of H_2 and in the presence of 1 mbar of H_2O are shown for comparison.

Fig. 6.11 shows CO_2 formation on FeO(111) films as a function of H_2 pressures. Adding 0.5 mbar of H_2 to a $CO + O_2$ mixture increased the reaction rate, by factor of 2. However, the effect is not dependent on H_2 amount in the range 0.5-1.5 mbar. At very high H_2 pressure, the FeO(111) film likely reconstructs in a different manner as discussed in the previous section.

As mentioned in the beginning of this chapter, many researchers attributed the promotional effect of H_2 to the formation of H_2O , which participates directly in the reaction via water-gas shift reaction. In order to elucidate whether the same mechanism could be applied to our system, we supplied 1 mbar of water vapor into the mixture of 10 mbar $CO + 50$ mbar O_2 . The results showed no effect of water on reactivity under these conditions. Therefore, it seems unlikely that water-gas shift pathway is involved in the CO

oxidation reaction in our system. Perhaps, CO oxidation is promoted by H₂ via the formation and decomposition of carbonate or formate intermediates created by the combination of surface OH groups with CO, but this hypothesis needs further experiments using IRAS.

Summary and Outlook

A catalytic reaction involves many steps in a complex system. Needless to say, it may be very difficult to extract the information on reaction mechanism. For this reason, a bottom-up approach is used to simplify the system. The application of model catalysts with well-defined structure provides a unique possibility to have a detailed understanding of the reaction kinetics and mechanism at the microscopic level by employing modern surface science techniques. However, results obtained under UHV conditions cannot be straightforwardly extended to reactions at realistic conditions. To bridge the “pressure gap”, reactivity studies at elevated pressures with structural characterization of systems are highly demanding. Here we demonstrated that monolayer FeO(111) films supported on Pt(111), which is essentially inert under UHV conditions, exhibits higher reactivity in low temperature CO oxidation than Pt(111) in the mbar pressure range. The proposed reaction mechanism involves first transformation of bi-layer Fe-O film into the tri-layer O-Fe-O (FeO₂) film that catalyses CO oxidation via Mars–van Krevelen type mechanism. Theoretical modeling corroborated this scenario and suggested that the oxidation step proceeds through activation of molecular oxygen by electrons that are transferred from the oxide/metal interface, thus resulting in O₂²⁻ species, which dissociate, ultimately forming an O-Fe-O film, which is considered as the key structure in the reaction.

We have extended our studies to Pt particles supported on Fe₃O₄(111) films. The results showed that Pt particles on Fe₃O₄(111) films exhibit the SMSI effect via encapsulation by a thin FeO(111) upon annealing to 850 K in UHV. The encapsulated Pt particles showed rate enhancement in low temperature CO oxidation, indicating that the FeO overlayer on top of Pt particles promotes CO oxidation in the same way as extended FeO film on Pt(111) single crystal.

The enhanced reactivity of thin oxide films returns us back to the so-called “electronic theory of catalysis” (see introduction). Briefly it states that oxide films on metal substrates and their thickness could be utilized to control electron transfer to surface-bonded species and render them catalytically active. This process, in principle, is determined by the work function of metal substrates and the electron affinity of adsorbates. Note that both of them may be modified by the presence of the oxide layer. In addition, the oxide film should be very thin to allow the charge transfer since thin films possess lattice flexibility which may significantly contribute to stabilize charged adsorbates (polaronic distortion). This property is not present in a thicker film, which behaves like the bulk counterpart.

FeO/Pt(111) films exhibit a high work function, mainly determined by the Pt(111) surface, which makes electron transfer from the metal/oxide interface to the adsorbate unlikely. However, due to the local restructuring of the film that is possible for limited thickness, the work function is locally lowered, and this allows charge transfer and the formation of a peroxo species. However, the work function of the tri-layer O-Fe-O phase is still high to transform adsorbed O₂ molecules spontaneously into superoxide anions O₂⁻ and promote CO oxidation via Eley-Rideal mechanism, which is the case for 2-3 MgO layers supported on Ag(100) due to the relatively low work function of the system [91].

Therefore, metal supported ultrathin oxide films may serve as potential catalysts, showing tunable physical and chemical properties by the appropriate combination of adsorbates and metal-oxide system. The electron affinity of different adsorbates and work function of some substrates are summarized in Tab. 7.1 and Tab. 7.2, respectively. In our work, we have replaced O₂ with NO for CO oxidation on FeO(111)/Pt(111). The results showed similar ability of NO in forming O-rich iron oxide films, though electron affinity of NO is lower than that of O₂. The mechanism of FeO oxidation is not determined yet. Nevertheless, CO+NO reaction shows much lower reactivity than that of CO+O₂ on FeO(111) films. Therefore, the results suggest that the rate-limiting step of the CO oxidation on FeO films may be associated with the oxygen replenishment step.

Tab. 7.1 Electron affinity of different adsorbates (eV)

Compound	E_a (eV)	Compound	E_a (eV)	Compound	E_a (eV)
H ₂	-5.771 [226]	C ₂ H ₄	-1.77 [226]	N ₂ O	0.15 [227]
HF	-3.875 [226]	HCN	-1.756 [226]	NO	0.10 [227]
H ₂ O	-2.938 [226]	C ₂ H ₂	-1.435 [226]	O ₂	0.45 [228]
NH ₃	-2.3 [226]	CO	-1.283 [226]	SO ₂	1.05 [229]
CH ₄	-1.9 [226]	C ₆ H ₆	-1.12 [230]	O ₃	2.10 [231]
N ₂	-1.9 [226]	CO ₂	-0.922 [226]	Cl ₂	2.4 [232]
Au	2.3 [83]	Pd	0.56 [83]	NO ₂	2.5 [233]

Tab. 7.2 Work function of different substrates (eV)

Sample	Φ (eV)	Sample	Φ (eV)	
Al (100)	4.20 [234]	1ML		
Ag (100)	4.22 [235]		LiF/Ag (100)	3.52 [236]
Mo (100)	4.53 [237]		NaCl/Ag 100)	3.53 [236]
Au (100)	5.22 [238]		MgO/Ag(100)	3.29 [236]
Pd (100)	5.55 [239]		Cas/Ag(100)	3.27 [236]
Pt (100)	5.84 [240]		BaO/Ag(100)	1.91 [236]
Pd (111)	5.60 [241]			
Pt (111)	6.10 [242]	3ML		
FeO/Pt(111)	5.50 [96]		MgO/Al(100)	2.86 [236]
MgO/Pt(111)	4.70 [96]		MgO/Mo(100)	2.15 [236]
			MgO/Ag(100)	2.96 [236]
			MgO/Au(100)	3.53 [236]
			BaO/Pd(100)	1.99 [236]
			BaO/Pt(100)	1.63 [236]
			BaO/Ag(100)	2.03 [236]
		BaO/Au(100)	2.33 [236]	

Another way in tuning the system is to change work function of the substrate. We performed preliminary experiments on CO+O₂ reactions on FeO(111) film grown on Pd(111). Well ordered FeO(111) films can be grown successfully on Pd(111) single crystals as shown in Fig. 7.1a, due to the similar lattice constant of Pd(111) (2.75 Å) to that of Pt(111) (2.78 Å). CO oxidation on FeO/Pd(111) in the mixture of 10 mbar CO and 50 mbar O₂ at 450 K was investigated. The same experiments on Pd(111) and FeO/Pt(111) are given for comparison. FeO overlayer on Pd(111) shows enhanced reactivity than the clean Pd, but proceeds slower than that on Pt(111) (see Fig. 7.1). It is contradict to the

expectation, since the work function of Pd(111) is lower than Pt(111), one would expect the higher reactivity for FeO films on Pd(111). One explanation is that besides charge transfer effects on metal-thin oxide systems, other factors should be taken into account. For example in this case palladium oxide layer underneath iron oxide may be formed, which makes the elucidation of the reaction mechanism further complicated.

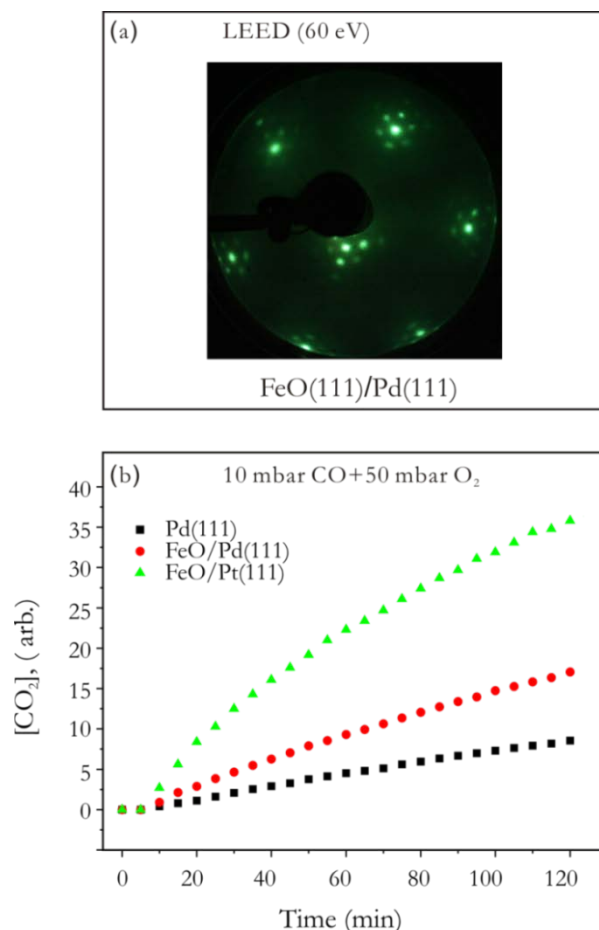


Fig. 7.1 (a) LEED pattern ($E= 60$ eV) of the FeO(111) film grown on Pd(111). (b) CO₂ production over Pd(111), FeO film on Pd(111) and FeO film on Pt(111) in 10 mbar CO + 50 mbar O₂ balanced by He at 450 K.

In summary, the results presented in the thesis may aid in our understanding of the interplay between structure and reactivity on metal supported ultrathin oxide films. Metal supported ultrathin film systems have designable properties. We believe that with the help of modern experimental techniques a new field in catalytic applications of ultrathin film may be developed in the future.

Abbreviations

AES	Auger Electron Spectroscopy
DFT	Density Function Theory
DOS	Density of States
ETC	Electronic Theory of Catalysis
FID	Flame Ionization Detector
GC	Gas Chromatography
HREELS	High Resolution Electron Energy Loss Spectroscopy
IRAS	Infrared Reflection Absorption Spectroscopy
LDOS	Local Density of States
LEED	Low Energy Electron Diffraction
ML	Monolayer
PM-IRAS	Polarization Modulated Infrared Reflection Absorption Spectroscopy
PROX	Preferential Oxidation of CO in H ₂
PVD	Physical Vapor Deposition
QMS	Quadrupole Mass Spectrometer
SFG	Sum Frequency Generation
SMSI	Strong Metal-Support Interaction
STM	Scanning Tunneling Microscopy
TCD	Thermal Conductivity Detector
TDS	Thermal Desorption Spectroscopy
TPD	Temperature Programmed Desorption
TPR	Temperature Programmed Reaction
UHV	Ultra-high Vacuum
XPS	X-ray Photoemission Spectroscopy

Curriculum Vitae

For reasons of data protection,
the curriculum vitae is not included in the online version

Publications

1. **Y.-N. Sun**, L. Giordano, J. Goniakowski, M. Lewandowski, Z.-H. Qin, C. Noguera, S. Shaikhutdinov, G. Pacchioni, H.-J. Freund, The interplay between structure and CO oxidation catalysis on metal-supported ultrathin oxide films. **Angewandte Chemie International Edition**, 49(26): p. 4418-4421, (2010). **Angewandte Chemie**, 122(26): p. 4520-4523, (2010).
2. M. Lewandowski, **Y.-N. Sun**, Z.-H. Qin, S. Shaikhutdinov, H.-J. Freund, Promotional effect of metal encapsulation on reactivity of iron oxide supported Pt catalysts. **Applied Catalysis A: General**, in press, (2010).
3. L. Giordano, M. Lewandowski, I. Groot, **Y.-N. Sun**, J. Goniakowski, C. Noguera, S. Shaikhutdinov, G. Pacchioni, H.-J. Freund, Oxygen-induced transformations of a FeO(111) film on Pt(111): a combined DFT and STM study. *Journal of Physical Chemistry C*, in press (2010).
4. Y. Lei, M. Lewandowski, **Y.-N. Sun**, Y. Fujimori, Y. Martynova, I.M.N. Groot, R. Meyer, L. Giordano, G. Pacchioni, J. Goniakowski, C. Noguera, S. Shaikhutdinov, H.-J. Freund, CO+NO vs CO+O₂ reaction on monolayer FeO(111) films on Pt(111). Submitted to *ChemCatChem*, (2010).
5. B. Brandt, **Y.-N. Sun**, J.-H. Fischer, J. Libuda, S. Shaikhutdinov, S. Schauermaun, H.-J. Freund, Methanol dissociation on Fe₃O₄/Pt(111) model oxide film. In Preparation, (2010).
6. **Y.-N. Sun**, Z.-H. Qin, M. Lewandowski, S. Shaikhutdinov, H.-J. Freund, Monolayer iron oxide film on platinum promotes low temperature CO oxidation. **Journal of Catalysis**, 266(2): p. 359-368, (2009).
7. **Y.-N. Sun**, Z.-H. Qin, M. Lewandowski, S. Shaikhutdinov, H.-J. Freund, CO adsorption and dissociation on iron oxide supported Pt particles. **Surface Science**, 603(20): p. 3099-3103, (2009)
8. Z.-H. Qin, M. Lewandowski, **Y.-N. Sun**, S. Shaikhutdinov, H.-J. Freund, Morphology and CO adsorption on platinum supported on thin Fe₃O₄(111) films. **Journal of Physics: Condensed Matter**, 21(13): p. 134019, (2009).
9. **Y.-N. Sun**, Z.-H. Qin, M. Lewandowski, S. Shaikhutdinov, H.-J. Freund, When an encapsulating oxide Layer promotes reaction on noble metals: dewetting and in situ formation of an “inverted” FeO_x/Pt catalyst. **Catalysis Letters**, 126(1-2): p. 31-35, (2008)
10. Z.-H. Qin, M. Lewandowski, **Y.-N. Sun**, S. Shaikhutdinov, H.-J. Freund, Encapsulation of Pt nanoparticles as a result of strong metal-support interaction with Fe₃O₄ (111). **Journal of Physical Chemistry C**, 112(27): p. 10209-10213, (2008).
11. S. Kaya, **Y.-N. Sun**, J. Weissenrieder, D. Stacchiola, S. Shaikhutdinov, H.-J. Freund, Ice-assisted preparation of silica-supported vanadium oxide particles. **Journal of Physical Chemistry C**, 111(14): p. 5337-5344, (2007).

Bibliography

1. Satterfield, C., *Heterogeneous Catalysis in Practice*. 1980: McGraw-Hill.
2. Ertl, G., H. Knözinger, and J. Weitkamp, *Handbook of heterogeneous catalysis*. 1997: Wiley VCH.
3. Thomas, J. and M. Thomas, *Principles and Practice of Heterogeneous Catalysis*. 1997: Wiley VCH.
4. Ertl, G., H. Knözinger, and J. Weitkamp, *Environmental catalysis*. 1999: Wiley VCH.
5. Freund, H., *Gerhard Ertl: Congratulations!* Surface Science Reports, 2008. **63**(2): p. iii-iv.
6. Ertl, G., *Reactions at Surfaces: From Atoms to Complexity (Nobel Lecture)*. Angewandte Chemie International Edition, 2008. **47**(19): p. 3524-3535.
7. Freund, H.J. and H. Knözinger, *Foreword for the Gerhard Ertl Festschrift*. Journal of Physical Chemistry B, 2004. **108**(38): p. 14183.
8. Christmann, K., G. Ertl, and T. Pignet, *Adsorption of hydrogen on a Pt(111) surface*. Surface Science, 1976. **54**(2): p. 365-392.
9. Ertl, G., M. Neumann, and K.M. Streit, *Chemisorption of CO on the Pt(111) surface*. Surface Science, 1977. **64**(2): p. 393-410.
10. Hayden, B.E., et al., *An infrared study of the adsorption of CO on a stepped platinum surface*. Surface Science, 1985. **149**(2-3): p. 394-406.
11. Hopster, H. and H. Ibach, *Adsorption of CO on Pt(111) and Pt 6(111) × (111) studied by high resolution electron energy loss spectroscopy and thermal desorption spectroscopy*. Surface Science, 1978. **77**(1): p. 109-117.
12. Kneringer, G. and F.P. Netzer, *Adsorption studies of oxygen and carbon monoxide on a Pt (100) surface*. Surface Science, 1975. **49**(1): p. 125-142.
13. McClellan, M.R., J.L. Gland, and F.R. McFeeley, *Carbon monoxide adsorption on the kinked Pt(321) surface*. Surface Science, 1981. **112**(1-2): p. 63-77.
14. Michely, T. and G. Comsa, *Temperature dependence of the sputtering morphology of Pt(111)*. Surface Science, 1991. **256**(3): p. 217-226.
15. Sharma, R.K., W.A. Brown, and D.A. King, *The adsorption of CO on Pt{110} over the temperature range from 90 to 300 K studied by RAIRS*. Surface Science, 1998. **414**(1-2): p. 68-76.
16. Steininger, H., S. Lehwald, and H. Ibach, *On the adsorption of CO on Pt(111)*. Surface Science, 1982. **123**(2-3): p. 264-282.
17. Goodman, D.W., *Model catalytic studies over metal single-crystals*. Accounts of Chemical Research, 1984. **17**(5): p. 194-200.
18. Goodman, D.W., *Model catalysis from extended single-crystals to supported particles*. Surface Review and Letters, 1995. **2**(1): p. 9-24.
19. Bäumer, M., J. Libuda, and H.J. Freund, *In chemisorption and reactivity on supported clusters and thin films*, ed. R.M. Lambert and G. Pacchioni. 1997, Dordrecht: Kluwer Acad. Press.
20. Campbell, C.T., *Ultrathin metal films and particles on oxide surfaces: structural, electronic and chemisorptive properties*. Surface Science Reports, 1997. **27**(1-3): p. 1-111.
21. Freund, H. and G. Pacchioni, *Oxide ultra-thin films on metals: new materials for the design of supported metal catalysts*. Chemical Society Reviews, 2008: p. 2224-2242.

22. Freund, H.-J., *Metal oxide surfaces: electronic structure and molecular adsorption*. Physica Status Solidi (b), 1995. **192**(2): p. 407-440.
23. Henry, C.R., *Surface studies of supported model catalysts*. Surface Science Reports, 1998. **31**(7-8): p. 231-325.
24. Street, S.C., C. Xu, and D.W. Goodman, *The Physical and Chemical Properties of Ultrathin Oxide Films*. Annual Review of Physical Chemistry, 1997. **48**(1): p. 43-68.
25. Goodman, D.W., *Model Studies in Catalysis Using Surface Science Probes*. Chemical Reviews, 1995. **95**(3): p. 523-536.
26. Vurens, G.H., et al., *Growth, structure and chemical properties of FeO overlayers on Pt(100) and Pt(111)*. Surface Science, 1992. **268**(1-3): p. 170-178.
27. Vurens, G.H., M. Salmeron, and G.A. Somorjai, *Structure, composition and chemisorption studies of thin ordered iron oxide films on platinum (111)*. Surface Science, 1988. **201**(1-2): p. 129-144.
28. Corneille, J.S., J.-W. He, and D.W. Goodman, *XPS characterization of ultrathin MgO films on a Mo(100) surface*. Surface Science, 1994. **306**(3): p. 269-278.
29. Jian-Wei, H., et al., *CO adsorption on ultrathin MgO films grown on a Mo(100) surface: an IRAS study*. Surface Science, 1992. **261**(1-3): p. 164-170.
30. Wu, M.C., et al., *Model surface studies of metal-oxides-adsorption of water and methanol on ultrathin MgO films on Mo(110)*. Journal of Chemical Physics, 1992. **96**(5): p. 3892-3900.
31. Wu, M.-C., et al., *Synthesis and characterization of ultra-thin MgO films on Mo(100)*. Chemical Physics Letters, 1991. **182**(5): p. 472-478.
32. Wu, M.-C., C.A. Estrada, and D.W. Goodman, *New approach to high-resolution electron-energy-loss spectroscopy of polar materials: Studies of water and methanol adsorption on ultrathin MgO(100) films*. Physical Review Letters, 1991. **67**(20): p. 2910.
33. Cappus, D., et al., *CO on NiO(100): orientation and bonding*. Surface Science, 1995. **325**(3): p. L421-L427.
34. Cappus, D., et al., *Hydroxyl groups on oxide surfaces: NiO(100), NiO(111) and Cr₂O₃(111)*. Chemical Physics, 1993. **177**(2): p. 533-546.
35. Freitag, A., et al., *Electronic surface state of NiO (100)*. Chemical Physics Letters, 1993. **210**(1-3): p. 10-14.
36. Kuhlbeck, H., et al., *Molecular adsorption on oxide surfaces: Electronic structure and orientation of NO on NiO(100)/Ni(100) and on NiO(100) as determined from electron spectroscopies and ab initio cluster calculations*. Physical Review B, 1991. **43**(3): p. 1969.
37. Rohr, F., et al., *Hydroxyl driven reconstruction of the polar NiO(111) surface*. Surface Science, 1994. **315**(1-2): p. L977-L982.
38. Schröder, T., et al., *Epitaxial growth of SiO₂ on Mo(112)*. Surface Review Letters, 2000. **7**: p. 7-14.
39. Schröder, S.L.M., et al., *Temperature programmed desorption*. 2002: Advanced Physical Chemistry Laboratory, FU Berlin.
40. Weissenrieder, J., et al., *Atomic structure of a thin silica film on a Mo(112) substrate: A two-dimensional network of SiO₄ tetrahedra*. Physical Review Letters, 2005. **95**(7): p. 076103.
41. Jaeger, R.M., et al., *Formation of a well-ordered aluminium oxide overlayer by oxidation of NiAl(110)*. Surface Science, 1991. **259**(3): p. 235-252.

42. Kresse, G., et al., *Structure of the ultrathin aluminum oxide film on NiAl(110)*. Science, 2005. **308**(5727): p. 1440-1442.
43. Kulawik, M., et al., *Atomic structure of antiphase domain boundaries of a thin Al₂O₃ film on NiAl(110)*. Physical Review Letters, 2003. **91**(25): p. 256101.
44. Libuda, J., et al., *Structure and defects of an ordered alumina film on NiAl(110)*. Surface Science, 1994. **318**(1-2): p. 61-73.
45. Bäumer, M. and H.-J. Freund, *Metal deposits on well-ordered oxide films*. Progress in Surface Science, 1999. **61**(7-8): p. 127-198.
46. Bäumer, M., et al., *The growth and properties of Pd and Pt on Al₂O₃/NiAl(110)*. Berichte der Bunsen-Gesellschaft-Physical Chemistry Chemical Physics, 1995. **99**(11): p. 1381-1386.
47. Freund, H.J., *Clusters and islands on oxides: from catalysis via electronics and magnetism to optics*. Surface Science, 2002. **500**(1-3): p. 271-299.
48. Lemire, C., et al., *CO adsorption on oxide supported gold: from small clusters to monolayer islands and three-dimensional nanoparticles*. Surface Science, 2004. **552**(1-3): p. 27-34.
49. Baron, M., et al., *Interaction of gold with cerium Oxide Supports: CeO₂(111) thin films vs CeO_x nanoparticles*. Journal of Physical Chemistry C, 2009. **113**(15): p. 6042-6049.
50. Libuda, J., et al., *Model studies in heterogeneous catalysis. from structure to kinetics*. Monatshefte für Chemie / Chemical Monthly, 2005. **136**(1): p. 59-75.
51. Lu, J.L., et al., *Gold supported on well-ordered ceria films: nucleation, growth and morphology in CO oxidation reaction*. Catalysis Letters, 2007. **114**(1-2): p. 8-16.
52. Meyer, R., et al., *Two-dimensional growth of Pd on a thin FeO(111) film: a physical manifestation of strong metal-support interaction*. Surface Science, 2003. **546**(2-3): p. L813-L819.
53. Meyer, R., et al., *CO adsorption and thermal stability of Pd deposited on a thin FeO(111) film*. Surface Science, 2005. **586**(1-3): p. 174-182.
54. Schalow, T., et al., *Formation of interface and surface oxides on supported Pd nanoparticles*. Surface Science, 2006. **600**(12): p. 2528-2542.
55. Shaikhutdinov, S.K., et al., *Determination of atomic structure of the metal-oxide interface: Pd nanodeposits on an FeO(111) film*. Physical Review Letters, 2003. **91**(7): p. 076102.
56. Schalow, T., et al., *CO oxidation on partially oxidized Pd nanoparticles*. Journal of Catalysis, 2006. **242**(1): p. 58-70.
57. Schalow, T., et al., *Oxygen-induced restructuring of a Pd/Fe₃O₄ model catalyst*. Catalysis Letters, 2006. **107**(3-4): p. 189-196.
58. Knözinger, H. and E. Taglauer, *Handbook of Heterogeneous Catalysis*, 1997. **1**: p. 216-231.
59. Datye, A.K., et al., *Comparison of metal-support Interactions in Pt/TiO₂ and Pt/CeO₂*. Journal of Catalysis, 1995. **155**(1): p. 148-153.
60. Fu, Q. and T. Wagner, *Interaction of nanostructured metal overlayers with oxide surfaces*. Surface Science Reports, 2007. **62**(11): p. 431-498.
61. Fu, Q., et al., *Metal-oxide interfacial reactions: Encapsulation of Pd on TiO₂ (110)*. Journal of Physical Chemistry B, 2005. **109**(2): p. 944-951.
62. Haller, G.L. and D.E. Resasco, *Metal-support interaction: Group VIII metals and reducible oxides*. Advances in Catalysis, 1989. **36**: p. 173-235.

63. Henrich, V.E., *The surfaces of metal oxides*. Reports on Progress in Physics, 1985. **48**(11): p. 1481-1541.
64. Solymosi, F., *Comments on electronic effects in strong metal-support interactions on titania-deposited metal catalysts*. Journal of Catalysis, 1985. **94**(2): p. 581-585.
65. Tauster, S.J., S.C. Fung, and R.L. Garten, *Strong metal-support interactions. Group 8 noble metals supported on TiO₂*. Journal of the American Chemical Society, 1978. **100**(1): p. 170-175.
66. Tung, R.T., *Recent advances in Schottky barrier concepts*. Materials Science and Engineering: R: Reports, 2001. **35**(1-3): p. 1-138.
67. Didier, F. and J. Jupille, *The van der Waals contribution to the adhesion energy at metal-oxide interfaces*. Surface Science, 1994. **314**(3): p. 378-384.
68. Stoneham, A.M. and P.W. Tasker, *Metal-non-metal and other interfaces: the role of image interactions*. Journal of Physics C: Solid State Physics, 1985. **18**(19): p. L543.
69. Duffy, D.M., J.H. Harding, and A.M. Stoneham, *Atomistic modelling of metal-oxide interfaces with image interactions*. Philosophical Magazine A, 1993. **67**(4): p. 865 - 882.
70. Schottky, W., *Halbleitertheorie der Sperrschicht*. Naturwissenschaften, 1938. **26**(52): p. 843-843.
71. Mott, N., *Note on the contact between a metal and an insulator or semiconductor*. Mathematical Proceedings of the Cambridge Philosophical Society, 1938. **34**: p. 568-572.
72. Bardeen, J., *Surface States and Rectification at a Metal Semi-Conductor Contact*. Physical Review, 1947. **71**(10): p. 717.
73. Cowley, A.M. and S.M. Sze, *Surface States and Barrier Height of Metal-Semiconductor Systems*. Journal of Applied Physics, 1965. **36**(10): p. 3212-3220.
74. Cabrera, N. and N.F. Mott, *Theory of the oxidation of metals*. Reports on Progress in Physics, 1948. **12**: p. 163-184.
75. Aigrain, P. and C. Dugas, *Adsorption sur les semi-conducteurs*. Zeitschrift Für Elektrochemie, 1952. **56**(4): p. 363-366.
76. Weisz, P.B., *Electronic Barrier Layer Phenomena in Chemisorption and Catalysis*. The Journal of Chemical Physics, 1952. **20**(9): p. 1483-1484.
77. Hauffe, K., *The application of the theory of semiconductors to problems of heterogeneous catalysis*. Advances in Catalysis, 1955. **7**: p. 213-257.
78. Hauffe, K. and H.J. Engell, *Zum Mechanismus der Chemisorption vom Standpunkt der Fehlordnungstheorie*. Zeitschrift Für Elektrochemie, 1952. **56**(4): p. 366-373.
79. Vol'kenshtein, F.F., *EXPERIMENT AND THE ELECTRONIC THEORY OF CATALYSIS*. Russian Chemical Reviews, 1966. **35**(7): p. 537.
80. Schwab, G.M., J. Block, and D. Schultze, *Intensification of contact catalysts by means of doped carriers*. Angewandte Chemie-International Edition, 1959. **71**(3): p. 101-104.
81. Schwab, G.-M., *Electronics of Supported Catalysts*, in *Advances in Catalysis*. 1978, Academic Press. p. 1-22.
82. Schwab, G.M., *Boundary-layer Catalysis*. Angewandte Chemie-International Edition, 1967. **6**(4): p. 375.

83. Frondelius, P., et al., *Charging of atoms, clusters, and molecules on metal-supported oxides: A general and long-ranged phenomenon*. Physical Review B, 2008. **78**(8): p. 085426.
84. Giordano, L. and G. Pacchioni, *Charge transfers at metal/oxide interfaces: a DFT study of formation of $K^{\delta+}$ and $Au^{\delta-}$ species on MgO/Ag(100) ultra-thin films from deposition of neutral atoms*. Physical Chemistry Chemical Physics, 2006. **8**(28): p. 3335-3341.
85. Pacchioni, G., L. Giordano, and M. Baistrocchi, *Charging of metal atoms on ultrathin MgO/Mo(100) Films*. Physical Review Letters, 2005. **94**(22): p. 226104.
86. Ricci, D., et al., *Bonding trends and dimensionality crossover of gold nanoclusters on metal-supported MgO thin films*. Physical Review Letters, 2006. **97**(3): p. 036106.
87. Sterrer, M., et al., *Control of the charge state of metal atoms on thin MgO films*. Physical Review Letters, 2007. **98**(9).
88. Honkala, K. and H. Hakkinen, *Au adsorption on regular and defected thin MgO(100) films supported by Mo*. Journal of Physical Chemistry C, 2007. **111**(11): p. 4319-4327.
89. Gronbeck, H., *Mechanism for NO_2 charging on metal supported MgO*. Journal of Physical Chemistry B, 2006. **110**(24): p. 11977-11981.
90. Starr, D.E., et al., *NO_2 adsorption on Ag(100) supported MgO(100) thin films: Controlling the adsorption state with film thickness*. Journal of Physical Chemistry C, 2009. **113**(17): p. 7355-7363.
91. Hellman, A., S. Klacar, and H. Gronbeck, *Low temperature CO oxidation over supported ultrathin MgO films*. Journal of the American Chemical Society, 2009. **132**(46): p. 16636-16637.
92. Giordano, L., et al., *Charging of metal adatoms on ultrathin oxide films: Au and Pd on FeO/Pt(111)*. Physical Review Letters, 2008. **101**(2).
93. Nilius, N., et al., *Self-organization of gold atoms on a polar FeO(111) surface*. Physical Review Letters, 2005. **95**(6): p. 066101.
94. Martinez, U., L. Giordano, and G. Pacchioni, *Tuning the work function of ultrathin oxide films on metals by adsorption of alkali atoms*. Journal of Chemical Physics, 2008. **128**(16): p. 164707-164708.
95. Zhao, W., et al., *Interaction and diffusion of potassium on $Cr_2O_3(0001)/Cr(110)$* . Physical Review B, 2000. **62**(11): p. 7527-7534.
96. Goniakowski, J., et al., *Adsorption of metal adatoms on FeO(111) and MgO(111) monolayers: Effects of charge state of adsorbate on rumpling of supported oxide film*. Physical Review B, 2009. **80**(12): p. 125403.
97. Weiss, W. and W. Ranke, *Surface chemistry and catalysis on well-defined epitaxial iron-oxide layers*. Progress in Surface Science, 2002. **70**(1-3): p. 1-151.
98. T. Engel and G. Ertl, *Elementary steps in the catalytic oxidation of carbon monoxide on platinum metals*. Advances in Catalysis, 1979. **28**: p. 1.
99. T. Engel and G. Ertl, *The Chemical Physics of Solid Surfaces and Heterogeneous Catalysts*, ed. D. A. King, D. P. Woodruff, and Eds. Vol. 4. 1982: Elsevier.
100. Rupprechter, G., *Surface vibrational spectroscopy from ultrahigh vacuum to atmospheric pressure: adsorption and reactions on single crystals and nanoparticle model catalysts monitored by sum frequency generation spectroscopy*. Physical Chemistry Chemical Physics, 2001. **3**(21): p. 4621-4632.

101. Rupprechter, G., 8 *Surface vibrational spectroscopy on noble metal catalysts from ultrahigh vacuum to atmospheric pressure*. Annual Reports Section "C" (Physical Chemistry), 2004. **100**: p. 237-311.
102. Rupprechter, G., et al., *Structure-activity correlations on Rh/Al₂O₃ and Rh/TiO₂ thin film model catalysts after oxidation and reduction*. Journal of Catalysis, 1999. **186**(1): p. 201-213.
103. Somorjai, G., *Surface science at high pressures*. Zeitschrift für Physikalische Chemie, 1996. **197**: p. 1.
104. Somorjai, G.A., *The flexible surface. Correlation between reactivity and restructuring ability*. Langmuir, 1991. **7**(12): p. 3176-3182.
105. King, D.A. and M.G. Wells, *Molecular beam investigation of adsorption kinetics on bulk metal targets: nitrogen on tungsten*. Surface Science, 1972. **29**: p. 454-482.
106. Clarke, L.J., *Surface Crystallography*. 1985: John Wiley & Sons Ltd.
107. Masel, R.I., *Principles of adsorption and reaction on solid surface*. 1996: Wiley.
108. Woodruff, D.P. and T.A. Delchar, *Modern techniques of surface science* 1994: Cambridge university Press.
109. Christmann, K., *Introduction to surface physical chemistry (Topic in physical chemistry)*. 1991, Darmstadt: Steinkopff-Verlag.
110. Venables, J.A., *Introduction to surface and thin film processes*. 1991: Cambridge university press.
111. Seah, M.P. and W.A. Dench, *Quantitative electron spectroscopy of surfaces: a standard data base for electron inelastic mean free paths in solids*. Surface and Interface Analysis|Surface and Interface Analysis, 1979. **1**(1): p. 2-11.
112. Niemantsverdriet, J.W., *Spectroscopy in Catalysis: An introduction*. 1993: Verlag Chemie, Weinheim.
113. Binnig, G. and H. Rohrer, *Scanning Tunneling Microscopy*. Helvetica Physica Acta, 1982. **55**(6): p. 726-735.
114. Bardeen, J., *Tunnelling from a Many-Particle Point of View*. Physical Review Letters, 1961. **6**(2): p. 57.
115. Tersoff, J. and D.R. Hamann, *Theory of the scanning tunneling microscope*. Physical Review B, 1985. **31**(2): p. 805.
116. Schichting, H. and D. Menzel, *Techniques for wide range, high resolution and precision, thermal desorption measurements: I. Principles of apparatus and operation*. Surface Science, 1993. **285**(3): p. 209.
117. John T. Yates, J., *Experimental Innovations in Surface Science: A Guide to Practical laboratory Methods and Instruments*. 1998, New York: Springer-Verlag.
118. March, R.E. and R.J. Hughes, *Quadropole storage mass spectrometry*. 1989: Wiley.
119. Zaremba, E. and W. Kohn, *Van der Waals interaction between an atom and a solid surface*. Physical Review B, 1976. **13**: p. 2270.
120. Zaremba, E. and W. Kohn, *Theory of helium adsorption on simple and noble-metal surfaces*. Physical Review B, 1977. **15**: p. 1769.
121. Wedler, G., *Chemisorption: An Experimental Approach (translated by Klemperer, F. D.)*. 1976: Butterworths.
122. Bauer, E. and F. Bonczek, *Thermal desorption of metals from tungsten single crystal surfaces* Surface Science, 1975. **53**(1): p. 87-109.

123. Habenschaden, E. and J. Küppers, *Evaluation of flash desorption spectra* Surface Science, 1984. **138**: p. L147.
124. Jong, A.M.d. and J.W. Niemantsverdriet, *Thermal desorption analysis: Comparative test of ten commonly applied procedures* Surface Science, 1990. **233**: p. 355.
125. King, D.A., *Thermal desorption from metal surfaces: A review* Surface Science, 1975. **47**: p. 384.
126. Redhead, P.A., *Thermal desorption of gases*. Vacuum, 1962. **12**: p. 203.
127. Bolina, A.S., A.J. Wolff, and W.A. Brown, *Reflection absorption infrared spectroscopy and temperature-programmed desorption studies of the adsorption and desorption of amorphous and crystalline water on a graphite surface*. Journal of Physical Chemistry B, 2005. **109**: p. 16836.
128. Zhdanov, V.P., J. Pavlíček, and Z. Knor, *Preexponential Factors for Elementary Surface Processes*. Catalysis Reviews: Science and Engineering, 1988. **30**(4): p. 501 - 517.
129. Baugh, P.J., *Gas chromatography A practical approach*. 2002, New York: Oxford University Press.
130. McNair, H. and J. Miller, *Basic gas chromatography*. 2009: Wiley-Interscience.
131. Cornell, R.M. and U. Schwertmann, *The Iron-oxides*. 1996: VCH, Weinheim.
132. Ketteler, G., et al., *Bulk and surface phases of iron oxides in an oxygen and water atmosphere at low pressure*. Physical Chemistry Chemical Physics, 2001. **3**(6): p. 1114-1122.
133. Darken, L.S. and R.W. Gurry, *The system iron-oxygen. I. The Wüstite field and related equilibria*. Journal of the American Chemical Society, 1945. **67**(8): p. 1398-1412.
134. Weiss, W. and M. Ritter, *Metal oxide heteroepitaxy: Stranski-Krastanov growth for iron oxides on Pt(111)*. Physical Review B, 1999. **59**(7): p. 5201-5213.
135. Fadley, C.S., et al., *Photoelectron diffraction: new dimensions in space, time, and spin*. Journal of Electron Spectroscopy and Related Phenomena, 1995. **75**: p. 273-297.
136. Galloway, H.C., P. Sautet, and M. Salmeron, *Structure and contrast in scanning tunneling microscopy of oxides: FeO monolayer on Pt(111)*. Physical Review B, 1996. **54**(16): p. R11145.
137. Geus, J.W., *Preparation and properties of iron oxide and metallic iron catalysts*. Applied Catalysis, 1986. **25**(1-2): p. 313-333.
138. Adib, K., et al., *Chemistry of CCl₄ on Fe₃O₄(111)-(2 x 2) surfaces in the presence of adsorbed D₂O studied by temperature programmed desorption*. Surface Science, 2003. **537**(1-3): p. 191-204.
139. Daschbach, J.L., et al., *Water adsorption, desorption, and clustering on FeO(111)*. Journal of Physical Chemistry B, 2005. **109**(20): p. 10362-10370.
140. Leist, U., W. Ranke, and K. Al-Shamery, *Water adsorption and growth of ice on epitaxial Fe₃O₄(111), FeO(111) and Fe₂O₃(biphase)*. Physical Chemistry Chemical Physics, 2003. **5**(11): p. 2435-2441.
141. Shaikhutdinov, S., et al., *Structure and reactivity of iron oxide surfaces*. Faraday Discussions, 1999. **114**: p. 363-380.
142. Zscherpel, D., W. Weiss, and R. Schlogl, *Adsorption and dehydrogenation of ethylbenzene on ultrathin iron oxide model catalyst films*. Surface Science, 1997. **382**(1-3): p. 326-335.

143. Biberrian, J. and M. Van Hove, *A new model for CO ordering at high coverages on low index metal surfaces: A correlation between LEED, HREELS and IRS II. CO adsorbed on fcc (111) and hep (0001) surfaces.* Surface Science, 1984. **138**(2-3): p. 361-389.
144. Persson, B., M. Tüshaus, and A. Bradshaw, *On the nature of dense CO adlayers.* Journal of Chemical Physics, 1990. **92**: p. 5034.
145. Carrasco, E., et al., *Infrared spectra of high coverage CO adsorption structures on Pt (111).* Surface Science, 2010. **604**(15-16): p. 1320-1325.
146. Steininger, H., S. Lehwald, and H. Ibach, *Adsorption of oxygen on Pt (111).* Surface Science, 1982. **123**(1): p. 1-17.
147. Collins, D.M. and W.E. Spicer, *Adsorption of CO, O₂ and H₂ on Pt.1. Thermal desorption spectroscopy studies.* Surface Science, 1977. **69**(1): p. 85-113.
148. McCabe, R.W. and L.D. Schmidt, *Binding states of CO on single crystal planes of Pt.* Surface Science, 1977. **66**(1): p. 101-124.
149. Winkler, A., et al., *Kinetics and energetics of oxygen adsorption on Pt (111) and Pt (112)-A comparison of flat and stepped surfaces.* Surface Science, 1988. **201**(3): p. 419-443.
150. Lemire, C., et al., *The surface structure of Fe₃O₄(111) films as studied by CO adsorption.* Surface Science, 2004. **572**(1): p. 103-114.
151. Schäfer, L. and H.W. Wassmuth, *Oxidation of graphitic carbon on a Pt(111) surface.* Surface Science, 1989. **208**(1-2): p. 55-70.
152. Libuda, J., et al., *Evidence for Pd_x(CO)_y compound formation on an alumina substrate.* Chemical Physics Letters, 1995. **240**(5-6): p. 429-434.
153. Sato, S. and Y. Ukisu, *Mechanism of the photolysis of iron pentacarbonyl adsorbed on a Pt surface.* Surface Science, 1993. **283**(1-3): p. 137-142.
154. Imbihl, R. and G. Ertl, *Oscillatory kinetics in heterogeneous catalysis.* Chemical Reviews, 1995. **95**(3): p. 697-733.
155. Santra, A.K. and D.W. Goodman, *Catalytic oxidation of CO by platinum group metals: From ultrahigh vacuum to elevated pressures.* Electrochimica Acta, 2002. **47**(22-23): p. 3595-3609.
156. Berlowitz, P.J., C.H.F. Peden, and D.W. Goodman, *Kinetics of CO oxidation on single crystal Pd, Pt and Ir.* Journal of Physical Chemistry, 1988. **92**(18): p. 5213-5221.
157. Bikondoa, O., et al., *Direct visualization of defect-mediated dissociation of water on TiO₂(110).* Nature Materials, 2006. **5**(3): p. 189-192.
158. Schaub, R., *Erratum: Oxygen-mediated diffusion of oxygen vacancies on the TiO₂(110) surface (Science (January 17, 2003) (377)).* Science, 2006. **314**(5801): p. 925.
159. Schaub, R., et al., *Oxygen-mediated diffusion of oxygen vacancies on the TiO₂(110) surface.* Science, 2003. **299**(5605): p. 377-379.
160. Mars, P. and D.W. van Krevelen, *Oxidations carried out by means of vanadium oxide catalysts.* Chemical Engineering Science, 1954. **3**: p. 41.
161. Vannice, M.A., *An analysis of the Mars-van Krevelen rate expression.* Catalysis Today, 2007. **123**(1-4): p. 18-22.
162. Kandalam, A.K., et al., *Oxidation of CO on Fe₂O₃ model surfaces.* Surface Science, 2007. **601**(21): p. 4873-4880.
163. Li, P., et al., *The removal of carbon monoxide by iron oxide nanoparticles.* Applied Catalysis B: Environmental, 2003. **43**(2): p. 151-162.

164. Randall, H., R. Doepper, and A. Renken, *Modeling CO oxidation on silica-supported iron oxide under transient conditions*. Industrial and Engineering Chemistry Research, 1997. **36**(8): p. 2996-3001.
165. Wagloehner, S., et al., *Kinetic modeling of the oxidation of CO on Fe₂O₃ catalyst in excess of O₂*. Journal of Catalysis, 2008. **260**(2): p. 305-314.
166. Giordano, L., et al., *Oxygen-induced transformations of a FeO(111) film on Pt(111): A combined DFT and STM study*. submitted, 2010.
167. Sun, Y.-N., et al., *The interplay between structure and CO oxidation catalysis on metal-supported ultrathin oxide films*. Angewandte Chemie, International Edition, 2010. **49**(26): p. 4418-4421.
168. Aizawa, H., et al., *A density-functional study of the atomic structures and vibrational spectra of NO/Pt(111)*. Surface Science, 2002. **514**(1-3): p. 394-403.
169. Gland, J.L. and B.A. Sexton, *Nitric-oxide adsorption on the Pt(111) surface*. Surface Science, 1980. **94**(2-3): p. 355-368.
170. Matsumoto, M., et al., *Study of the adsorption structure of NO on Pt(111) by scanning tunneling microscopy and high-resolution electron energy-loss spectroscopy*. Surface Science, 2000. **454**: p. 101-105.
171. Matsumoto, M., et al., *Dynamical low-energy electron diffraction analysis of the structure of nitric oxide on Pt(111)*. Surface Science, 2002. **513**(3): p. 485-500.
172. Xu, C. and B.E. Koel, *A LEED, TPD AND HREELS investigation of NO adsorption on Sn/Pt(111) surface alloys*. Surface Science, 1994. **310**(1-3): p. 198-208.
173. Zhu, J.F., et al., *The adsorption of NO on an oxygen pre-covered Pt(111) surface: in situ high-resolution XPS combined with molecular beam studies*. Surface Science, 2003. **547**(3): p. 410-420.
174. Blyholder, G., *Molecular Orbital View of Chemisorbed Carbon Monoxide*. Journal of Physical Chemistry, 1964. **68**(10): p. 2772-2777.
175. Blyholder, G., *CNDO model of carbon monoxide chemisorbed on nickel*. Journal of Physical Chemistry, 1975. **79**(7): p. 756-761.
176. Cosandey, F., L. Zhang, and T.E. Madey, *Effect of substrate temperature on the epitaxial growth of Au on TiO₂(1 1 0)*. Surface Science, 2001. **474**(1-3): p. 1-13.
177. Dulub, O., W. Hebenstreit, and U. Diebold, *Imaging cluster surfaces with atomic resolution: The strong metal-support interaction state of Pt supported on TiO₂(110)*. Physical Review Letters, 2000. **84**(16): p. 3646-3649.
178. Gao, Y., Y. Liang, and S.A. Chambers, *Thermal stability and the role of oxygen vacancy defects in strong metal support interaction - Pt on Nb-doped TiO₂(100)*. Surface Science, 1996. **365**(3): p. 638-648.
179. Jennison, D.R., et al., *Structure of an ultrathin TiO_x film, formed by the strong metal support interaction (SMSI), on Pt nanocrystals on TiO₂(1 1 0)*. Surface Science, 2001. **492**(1-2): p. L677-L687.
180. Mullins, D.R. and K.Z. Zhang, *Metal-support interactions between Pt and thin film cerium oxide*. Surface Science, 2002. **513**(1): p. 163-173.
181. Pesty, F., H.P. Steinrück, and T.E. Madey, *Thermal stability of Pt films on TiO₂(110): evidence for encapsulation*. Surface Science, 1995. **339**(1-2): p. 83-95.
182. Shaikhutdinov, S., et al., *Interaction of oxygen with palladium deposited on a thin alumina film*. Surface Science, 2002. **501**(3): p. 270-281.

183. Qin, Z., et al., *Encapsulation of Pt nanoparticles as a result of strong metal-support interaction with Fe₃O₄ (111)*. Journal of Physical Chemistry C, 2008. **112**(27): p. 10209-10213.
184. Qin, Z., et al., *Morphology and CO adsorption on platinum supported on thin Fe₃O₄(111) films*. Journal of Physics: Condensed Matter, 2009. **21**(13).
185. Altman, E.I. and R.J. Gorte, *The desorption of CO from small Pt particles on Al₂O₃*. Surface Science, 1986. **172**(1): p. 71-80.
186. Altman, E.I. and R.J. Gorte, *A comparison of the desorption of CO from Pt and Rh particles on α -Al₂O₃{0001}*. Surface Science, 1988. **195**(3): p. 392-402.
187. Doering, D.L., H. Poppa, and J.T. Dickinson, *Chemisorption of CO on particulate deposits of platinum*. Journal of Vacuum Science & Technology, 1981. **20**(3): p. 827-830.
188. Højrup Hansen, et al., *Palladium nanocrystals on Al₂O₃: structure and adhesion Energy*. Physical Review Letters, 1999. **83**(20): p. 4120-4123.
189. Bonzel, H.P. and R. Ku, *Adsorbate interactions on a Pt(110) surface. I. Sulfur and carbon monoxide*. Journal of Chemical Physics, 1973. **58**: p. 4617-4624.
190. McCabe, R.W. and L.D. Schmidt, *Adsorption of H₂ and CO on clean and oxidized (110) Pt*. Surface Science, 1976. **60**(1): p. 85-98.
191. Shumbera, R.B., H.H. Kan, and J.F. Weaver, *Temperature-programmed reaction of CO adsorbed on oxygen-covered Pt(100): Reactivity of high-coverage oxygen phases*. Journal of Physical Chemistry C, 2008. **112**(11): p. 4232-4241.
192. Wadayama, T., et al., *Infrared reflection-absorption study of carbon monoxide adsorption on Fe/Pt(111) bimetallic surfaces*. Journal of Physical Chemistry C, 2008. **112**(24): p. 8944-8950.
193. Pint, C., G. Bozzolo, and J.E. Garcés, *Growth and alloy formation of Fe on flat and stepped Pt substrates*. Surface Science, 2008. **602**(2): p. 559-570.
194. Ali, A., et al., *Carbon monoxide adsorption on a Pt₈₀Fe₂₀(111) single-crystal alloy*. Surface Science, 1994. **302**(1-2): p. 121-125.
195. Xu, C. and B.E. Koel, *Probing the modifier precursor state: adsorption of CO on Sn/Pt(111) surface alloys*. Surface Science, 1994. **304**(3).
196. Vermang, B., M. Juel, and S. Raaen, *CO adsorption on Ce-Pt(111) studied with LEED, XPS, and temperature programmed desorption*. Physical Review B, 2006. **73**: p. 033407.
197. Vannice, M.A., *The catalytic synthesis of hydrocarbons from H₂/CO mixtures over the group VIII metals : I. The specific activities and product distributions of supported metals*. Journal of Catalysis, 1975. **37**(3): p. 449.
198. Iwasawa, Y., et al., *The reactions of carbon monoxide at coordinatively unsaturated sites on a platinum surface*. Chemical Physics Letters, 1976. **44**(3): p. 468-470.
199. Lang, B., R.W. Joyner, and G.A. Somorjai, *Low energy electron diffraction studies of chemisorbed gases on stepped surfaces of platinum*. Surface Science, 1972. **30**(2): p. 454-474.
200. Li, X.Q.D. and R. Vanselow, *Dissociation of CO on stepped/kinked surface areas of a rounded Pt crystal: I. Clean surface*. Catalysis Letters, 1989. **2**(2): p. 113-120.
201. Rupprechter, G., et al., *High-pressure carbon monoxide adsorption on Pt(III) revisited: A sum frequency generation study*. Journal of Physical Chemistry B, 2001. **105**(18): p. 3797-3802.

202. McCrea, K., et al., *Surface structure sensitivity of high-pressure CO dissociation on Pt(557), Pt(100) and Pt(111) using sum frequency generation surface vibrational spectroscopy*. *Surface Science*, 2001. **494**(3): p. 238-250.
203. Schauermaun, S., et al., *Adsorption, decomposition and oxidation of methanol on alumina supported palladium particles*. *Physical Chemistry Chemical Physics*, 2002. **4**(15): p. 3909-3918.
204. Senanayake, S.D., et al., *The reaction of carbon monoxide with palladium supported on cerium oxide thin films*. *Surface Science*, 2007. **601**(15): p. 3215-3223.
205. Lemons, R.A., *Fuel cells for transportation*. *Journal of Power Sources*, 1990. **29**(1-2): p. 251-264.
206. Alexeev, O.S., et al., *Effects of reduction temperature and meta-support interactions on the catalytic activity of Pt/ α -Al₂O₃ and Pt/TiO₂ for the oxidation of CO in the presence and absence of H₂*. *Journal of Physical Chemistry B*, 2005. **109**(49): p. 23430-23443.
207. Atalik, B. and D. Uner, *Structure sensitivity of selective CO oxidation over Pt/[γ]-Al₂O₃*. *Journal of Catalysis*, 2006. **241**(2): p. 268-275.
208. Fukuoka, A., et al., *Preferential Oxidation of Carbon Monoxide Catalyzed by Platinum Nanoparticles in Mesoporous Silica*. *Journal of the American Chemical Society*, 2007. **129**(33): p. 10120-10125.
209. Kahlich, M.J., H.A. Gasteiger, and R.J. Behm, *Kinetics of the Selective CO Oxidation in H₂-Rich Gas on Pt/Al₂O₃*. *Journal of Catalysis*, 1997. **171**(1): p. 93-105.
210. Manasilp, A. and E. Gulari, *Selective CO oxidation over Pt/alumina catalysts for fuel cell applications*. *Applied Catalysis B: Environmental*, 2002. **37**(1): p. 17-25.
211. Zhou, S., Z. Yuan, and S. Wang, *Selective CO oxidation with real methanol reformat over monolithic Pt group catalysts: PEMFC applications*. *International Journal of Hydrogen Energy*, 2006. **31**(7): p. 924-933.
212. Kotobuki, M., et al., *Reaction mechanism of preferential oxidation of carbon monoxide on Pt, Fe, and Pt-Fe/mordenite catalysts*. *Journal of Catalysis*, 2005. **236**(2): p. 262-269.
213. Liu, X., O. Korotkikh, and R. Farrauto, *Selective catalytic oxidation of CO in H₂: structural study of Fe oxide-promoted Pt/alumina catalyst*. *Applied Catalysis A: General*, 2002. **226**(1-2): p. 293-303.
214. Shou, M., et al., *New catalyst for selective oxidation of CO in excess H₂ designing of the active catalyst having different optimum temperature*. *Catalysis Today*, 2004. **90**(3-4): p. 255-261.
215. Tanaka, K., et al., *A new catalyst for selective oxidation of CO in H₂: Part I, activation by depositing a large amount of FeO_x on Pt/Al₂O₃ and Pt/CeO₂ catalysts*. *Catalysis Letters*, 2004. **92**: p. 115-121.
216. Sirijaruphan, A. and J. Goodwin, *Effect of Fe promotion on the surface reaction parameters of Pt/ γ -Al₂O₃ for the selective oxidation of CO*. *Journal of Catalysis*, 2004. **224**(2): p. 304-313.
217. Liu, K., et al., *Quasi In Situ ⁵⁷Fe Mossbauer Spectroscopic Study: Quantitative Correlation between Fe²⁺ and H₂ Concentration for PROX over Ir- Fe/SiO₂ Catalyst*. *Journal of Physical Chemistry C*, 2010. **114**(18): p. 8533-8541.

218. Pozdnyakova-Tellinger, O., et al., *Surface water-assisted preferential CO oxidation on Pt/CeO₂ catalyst*. Journal of Physical Chemistry C, 2007. **111**(14): p. 5426-5431.
219. Jacobs, G., et al., *Low-temperature water-gas shift: impact of Pt promoter loading on the partial reduction of ceria and consequences for catalyst design*. Journal of Catalysis, 2005. **229**(2): p. 499-512.
220. Mhadeshwar, A.B. and D.G. Vlachos, *Microkinetic modeling for water-promoted CO oxidation, water-gas shift, and preferential oxidation of CO on Pt*. Journal of Physical Chemistry B, 2004. **108**(39): p. 15246-15258.
221. Shi, X., et al., *The Mechanism for the Selective Oxidation of CO Enhanced by H₂O on a Novel PROC Catalyst*. Catalysis Letters, 2008. **120**(3): p. 210-214.
222. Shou, M. and K.-i. Tanaka, *Isotope effect of H₂/D₂ and H₂O/D₂O for the PROX reaction of CO on the FeO_x/Pt/TiO₂ catalyst*. Catalysis Letters, 2006. **111**(3): p. 115-118.
223. Tanaka, K.-I., et al., *Significant enhancement of the oxidation of CO by H₂ and/or H₂O on a FeO_x/Pt/TiO₂ catalyst*. Catalysis Letters, 2006. **110**(3): p. 185-190.
224. Pozdnyakova, O., et al., *Preferential CO oxidation in hydrogen (PROX) on ceria-supported catalysts, part I: Oxidation state and surface species on Pt/CeO₂ under reaction conditions*. Journal of Catalysis, 2006. **237**(1): p. 1-16.
225. Wadayama, T. and et al., *Infrared reflection absorption study of carbon monoxide adsorption on Fe-deposited Pt(111) surface*. Journal of Physics: Conference Series, 2008. **100**(1): p. 012007.
226. Zhan, C.-G., J.A. Nichols, and D.A. Dixon, *Ionization potential, electron affinity, electronegativity, hardness, and electron excitation energy: molecular properties from density functional theory orbital energies*. Journal of Physical Chemistry A, 2003. **107**(20): p. 4184-4195.
227. Nalley, S.J., et al., *Molecular electron affinities from collisional ionization of cesium. I. NO, NO₂, and N₂O*. Journal of Chemical Physics, 1973. **59**(8): p. 4125-4139.
228. Scaronulka, M., et al., *Electron affinity of the O₂ molecule: CCSD(T) calculations using the optimized virtual orbitals space approach*. International Journal of Quantum Chemistry, 2008. **108**(12): p. 2159-2171.
229. Refaey, K.M.A. and J.L. Franklin, *Endoergic ion--molecule-collision processes of negative ions. I. Collision of I on SO₂*. Journal of Chemical Physics, 1976. **65**(5): p. 1994-2001.
230. Burrow, P.D., J.A. Michejda, and K.D. Jordan, *Electron transmission study of the temporary negative ion states of selected benzenoid and conjugated aromatic hydrocarbons*. The Journal of Chemical Physics, 1987. **86**(1): p. 9-24.
231. Novick, S.E., et al., *Laser photoelectron, photodetachment, and photodestruction spectra of O₃⁻*. Journal of Chemical Physics, 1979. **70**(6): p. 2652-2662.
232. Dispert, H. and K. Lacmann, *Chemiiionization in alkali-halogen reactions: Evidence for ion formation by alkali dimers*. Chemical Physics Letters, 1977. **47**(3): p. 533-536.
233. Smith, G.P., L.C. Lee, and P.C. Cosby, *Photodissociation and photodetachment of molecular negative ions. VIII. Nitrogen oxides and hydrates, 3500--8250 [A-ring]*. Journal of Chemical Physics, 1979. **71**(11): p. 4464-4470.

234. Eastment, R.M. and C.H.B. Mee, *Work function measurements on (100), (110) and (111) surfaces of aluminium*. Journal of Physics F: Metal Physics, 1973. **3**(9): p. 1738.
235. Chelvayohan, M. and C.H.B. Mee, *Work function measurements on (110), (100) and (111) surfaces of silver*. Journal of Physics C: Solid State Physics, 1982. **15**(10): p. 2305.
236. Prada, S., U. Martinez, and G. Pacchioni, *Work function changes induced by deposition of ultrathin dielectric films on metals: A theoretical analysis*. Physical Review B, 2008. **78**(23): p. 235423.
237. Berge, S., P.O. Gartland, and B.J. Slagsvold, *Photoelectric work function of a molybdenum single crystal for the (100), (110), (111), (112), (114), and (332) faces*. Surface Science, 1974. **43**(1): p. 275-292.
238. Hansson, G.V. and S.A. Flodström, *Photoemission study of the bulk and surface electronic structure of single crystals of gold*. Physical Review B, 1978. **18**(4): p. 1572.
239. Hözl, J. and F.K. Schulte, *Solid surface physics*. Vol. 85. 1979: Springer, Heidelberg.
240. Rotermund, H.H., et al., *Investigation of surfaces by scanning photoemission microscopy*. Journal of Electron Spectroscopy and Related Phenomena, 1990. **52**: p. 811-819.
241. Demuth, J.E., *Chemisorption of C₂H₂ on Pd(111) and Pt(111): formation of a thermally activated olefinic surface complex*. Chemical Physics Letters, 1977. **45**(1): p. 12-17.
242. Derry, G.N. and Z. Ji-Zhong, *Work function of Pt(111)*. Physical Review B, 1989. **39**(3): p. 1940.